Development of an ECR Ion Source Using Liquid-Helium-Free Superconducting Solenoid Coils

Tetsuro KURITA

A dissertation submitted to the Doctoral Program
in Physics, the University of Tsukuba
in partial fulfillment of the requirements for the
degree of Doctor of Philosophy (Science)

February, 2001

Abstract

Over the last several years, we have been constructing a facility for experiments to study the dynamic behavior of metal clusters in various processes, such as fission and multi-fragmentation. One of the main capabilities of this facility is the production of multiply ionized metal clusters through soft peripheral collisions with highly charged ions. The collisions occurs when the beam of metal clusters crosses a beam of highly charged ions. To produce the intense beam of highly charged ions for this experiment, we constructed an Electron Cyclotron Resonance Ion Source (ECRIS) using a liquid-He-free superconducting magnet.

The new source uses Gifford-McMahon refrigerators for cooling the solenoid coils instead of liquid He. This feature allows us to avoid the higher costs in consuming liquid He, the complicated operation and bulkiness of ordinary superconducting magnets using liquid He. To implement this magnetic system efficiently, we determined the optimum configuration for the solenoid coils, the axial position of the yoke, in addition to the optimum operational parameters, such as the current in the coils. Also we determined the optimum shape of the hexapole magnet. A maximum axial magnetic field of 3 T and a radial magnetic field of 1 T on the plasma chamber wall are provided with this magnetic system. Microwaves of 14.5 GHz (maximum power of 2 KW) are used for heating the plasma. The new type ECRIS was named SHIVA (**S**uperconducting without liquid **H**e ECR **I**on source for **V**arious **A**tomic cluster experiments).

In addition, experiments to determine the optimum conditions of the source have been preformed. SHIVA excelled in producing intense highly charged ion beams. We obtained a current of 5.7 μA of Xe^{32+}, 3.8 μA of Xe^{33+} and 0.9 μA of Xe^{36+}. These set world records for beam intensities of highly charged Xe ions extracted from an ECRIS using 14.5 GHz microwaves. In comparison with other high performance ECRISs using 14.5 GHz microwaves, we found that the long plasma chamber, the high magnetic field and the aluminium cylinder of SHIVA achieves longer ion

confinement time and more intense beams of highly charged ions. The long plasma chamber, the high magnetic field and the aluminum cylinder on the wall of the plasma chamber are essentials in producing intense beams of highly charged ions.

Contents

Chapter 1

Introduction

1.1 Cluster Fission Project

The fission and fragmentation processes of multiply charged clusters have been subject to many experimental and theoretical investigations since they were observed by Sattler et al. [1]. Lord Rayleigh predicted that a Z-fold charged droplet would become unstable with respect to the quadrupole deformations at the critical size N_Z^{crit} at which its Coulomb energy $E_c(N, Z)$ equals twice its surface energy $E_s(N)$, more precisely,

$$E_c\left(N_Z^{crit}, Z\right) = 2E_S\left(N_Z^{crit}\right) \rightarrow N_Z^{crit} = \frac{e^2 Z^2}{16\pi r_s^2 \sigma} \tag{1.1}$$

Here σ is the bulk surface tension of the respective element and the radius r_s is determined from the equation $\frac{4\pi}{3} r_s^3 = \frac{m}{\rho}$, where m is the atomic mass and ρ is the mass density of the associated bulk material.

Recently, Chandezon et al. produced multiply charged metal clusters which have a charge state higher than the critical value [2], which displayed interesting new behavior [3]. One of the main features of their experimental method is the production of multiply ionized clusters through soft peripheral collisions of highly charged ions with atomic clusters. This method allows multiple ionization of atomic clusters without strong additional excitations [2]. As described in Ref. [3], the use of higher-charge-state heavy ions allows the production of higher charge state metal clusters. Consequently, we can observe the fission phenomena of heavier metal clusters because the critical size of the metal cluster is proportional to Z^2 as described in Eq. 1.1. Furthermore, if we can analyze metal clusters of a

selected mass before they intersect an ion beam, which has been never done before, we can clearly observe the fundamental processes of fission without complication.

To study the dynamic behavior of larger metal clusters in various processes, like fission, multi-fragmentation, we are constructing a new facility shown in Fig. 1.1. A pulsed cluster beam is generated by a magnetron sputter-type cluster ion source. It can produce clusters larger than a few thousand atoms [4]. The m/q of a cluster is selected by an energy analyzer and an analyzing magnet. Before the mass-selected clusters intersect a highly charged ion beam, the cluster beam will be deaccelerated, and then multiply ionized cluster will be generated through soft peripheral collisions with the highly charged heavy ions. The mass of fragments produced through the fission process will be measured by a T. O. F. system.

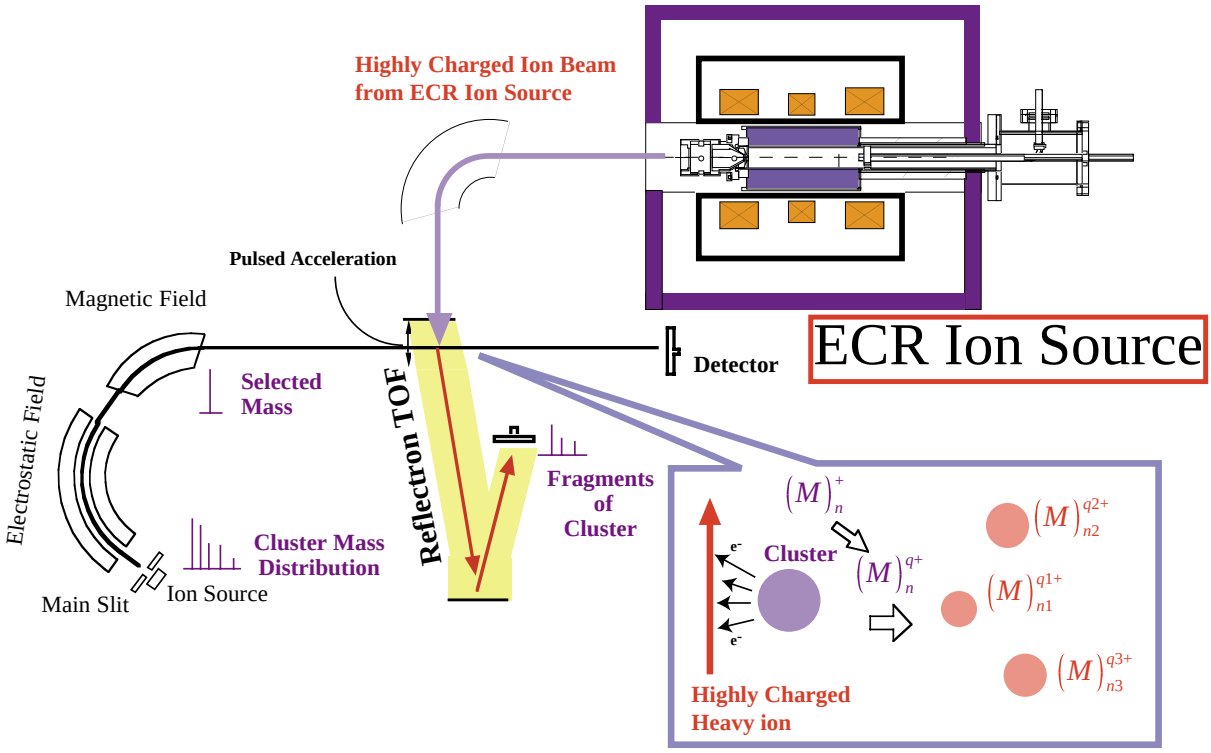

Figure 1.1: A schematic of the experimental setup for multi-charged cluster fission.

One of the planed experiments in the cluster fission project is to observe fission phenomena in both the liquid phase and the solid phase, and to see the difference of fission mechanisms in both phases for the first time in the

world. In the case of sodium clusters, a phase transition from the liquid phase to the solid phase is observed experimentally. Fig. 1.2 shows mass spectra of photoionized $(Na)_n$ clusters from a gas-aggregation-type cluster source [5]. The closed shells are associated with valleys of intensity in the spectra. The closed shells appear with equally spaced intervals on the $n^{1/3}$ for lager clusters (Na_n, $n > 1400$). These closed shells for large cluster do not correspond to electric shells, but shells of atoms. The spectra in Fig .1.2 indicate the existence of a "liquid" to "solid" transition of going from small to large clusters around a cluster size 1400.

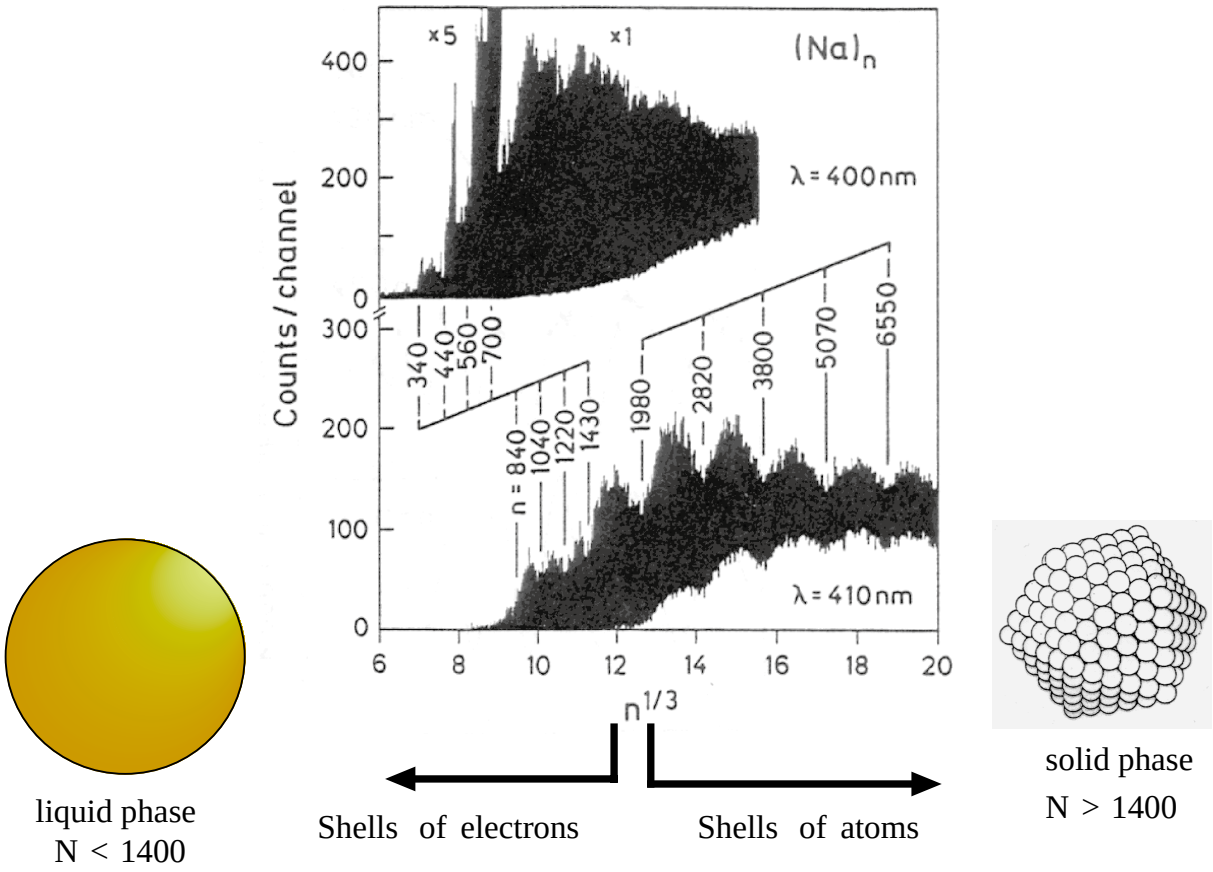

Figure 1.2: Mass spectra of $(Na)_n$ clusters photoionized with 400 and 410 nm light [5].

Fig. 1.3 shows the critical size N_Z^{crit} (Eq. 1.1) as a function of the charge state of clusters for various materials. To obtain critical sizes over 1000 where the phase transition can be expected for various materials, charges over 30+ must be given to clusters.

We assume that a cluster of charge Z+ is generated by collision of the

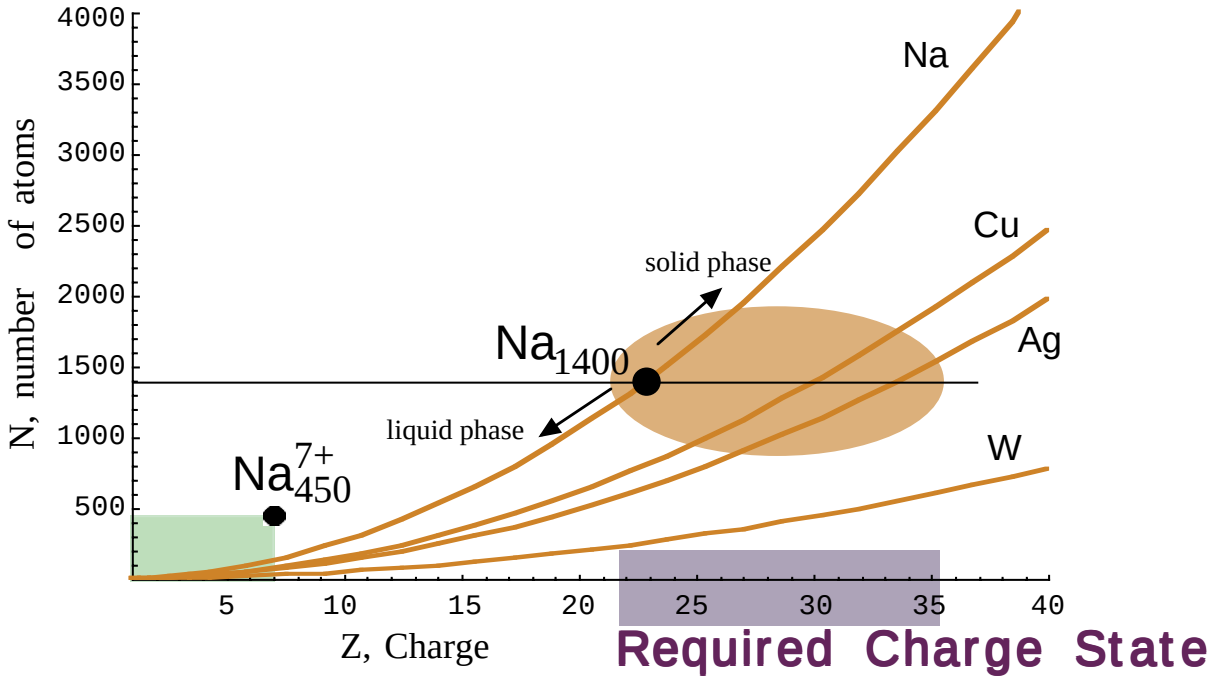

Figure 1.3: The critical size N_Z^{crit} (Eq. 1.1) as a function of the charge state of clusters for various materials. The values of surface tension are from in Ref. [6].

cluster with an ion beam of charge Z+. And considering the production rate and size of the metal clusters from the cluster ion source, we concluded that the ability to produce a current of 10 eμA of Xe^{30+} is required for the new ion source of this facility.

The new ECR ion source will make advanced experiments possible, compared with those with Na_{450}^{7+} which currently has the maximum charge state and the cluster size for the observed fission phenomena [7]. And we will be able to observe fission phenomena in both the liquid phase and the solid phase, and study the differences in the phenomena between the two phases.

1.2 Toward Development of a New ECR Ion Source

At the present stage, only an electron cyclotron resonance ion source (ECRIS) produce intense, stable and continuous beams of highly charged heavy ions such as a beam Xe^{30+} at 10 eμA. The ECRIS was first proposed by R. Geller and his coworkers in 1965 using their experience in mirror machines for fusion plasma studies. ECRISs are now used in heavy

ion accelerators and atomic physics research worldwide. The advantage of the ECRIS is not only in producing high-charge-state ion beams but also high intensity ion beams, which are required to produce multiply ionized cluster effectively.

The production of highly charged ions in the ECRIS depends on the many parameters e.g., the plasma density n_e, the ion confinement time τ_i, and the electron temperature T_e.

In the batch model [8], the relationship between the average charge state and the parameters of the ECRIS is written as

$$q \propto \log n\tau_i w \tag{1.2}$$

where w is the velocity of the electron corresponding to the electron temperature T_e. The ion confinement time τ_i is written as [9]

$$\tau_i \propto B_{max} \tag{1.3}$$

where B_{max} is the maximum magnetic field strength for plasma confinement. Combining the above two equations, we can obtain a scaling law which was proposed by R. Geller,

$$q \propto \log B_{max} \tag{1.4}$$

On the other hand, in order to confine a high-density hot electron plasma in a magnetic trap, the following condition must be satisfied.

$$p_{particle} \ll p_{magnetic} \tag{1.5}$$

where $p_{magnetic}$ and $p_{particle}$ are the pressures of the magnetic field and the charged particles in the plasma, defined as

$$p_{magnetic} = \frac{B^2}{2\mu_0} \tag{1.6}$$

$$p_{particle} = n_e k_B T_e + n_i k_B T_i \tag{1.7}$$

where μ_0, k_B and T_i are the permeability of free space, Boltzmann's constant and the ion temperature, respectively.

In an ECR plasma, the electron temperature is much higher than the ion temperature i.e. , $T_e \gg T_i$, then the second term on the right side of Eq. 1.7 is negligible. Therefore, Equation 1.5 may be rewritten:

$$n_e k_B T_e \ll \frac{B^2}{2\mu_0} \tag{1.8}$$

This equation suggests that the magnetic field increase is acting on both the electron density and the electron temperature. Consequently, a higher electron density achieved by a higher magnetic field allows one to have high ion densities through the plasma charge neutrality condition.

Therefore, a high magnetic field is essential to produce highly charged ions from an ECRIS. Very recently, Catania's group reported that the beam intensity of highly charged heavy ions increases with the magnetic field strength in a superconducting ECRIS (SERSE). The beam intensity was saturated at a magnetic field strength of 3 to 4 times the B_{ECR}, where the B_{ECR} is the magnetic field strength when the Larmor frequency of the electrons is equal to the frequency of the microwaves. To achieve a magnetic field strength around 4 B_{ECR} with reasonable power consumption, we have to use a superconducting magnet. However, at the present stage, it still has a big disadvantages. We have to use liquid He, requiring a supply system and complicating operations. From the viewpoints of operation times, reliability and cost performance, a superconducting magnet requiring liquid He is not suitable for use in the solenoid coils and the hexapole magnet of an ECR ion source, especially, in a small laboratory.

Now we are proposing to use liquid-He-free superconducting solenoid coils for the new ECR ion source of this facility. The purpose of this study is constructing a new ECR ion source not only to meet the requirements of the cluster fission project but also to mark departure from anything that had been done before. Also we search for the optimum parameters to produce a intense beam of highly charged heavy ions, such as a beam Xe^{30+} at 10 eμA.

This thesis is organized as follows:
The basic principles and the functioning of an ECRIS is described in following chapter. In chapter 3, the experimental results of the biased electrode

method used to amplify a beam intensity are presented. A description of our new superconducting ECRIS is presented in chapter 4. In chapter 5, the experimental results are presented. Finally, our conclusion is summarized in chapter 6.

Chapter 2

Principle of Electron Cyclotron Resonance Ion Source

2.1 General Description

Figure 2.1 shows a schematic of an ECRIS.

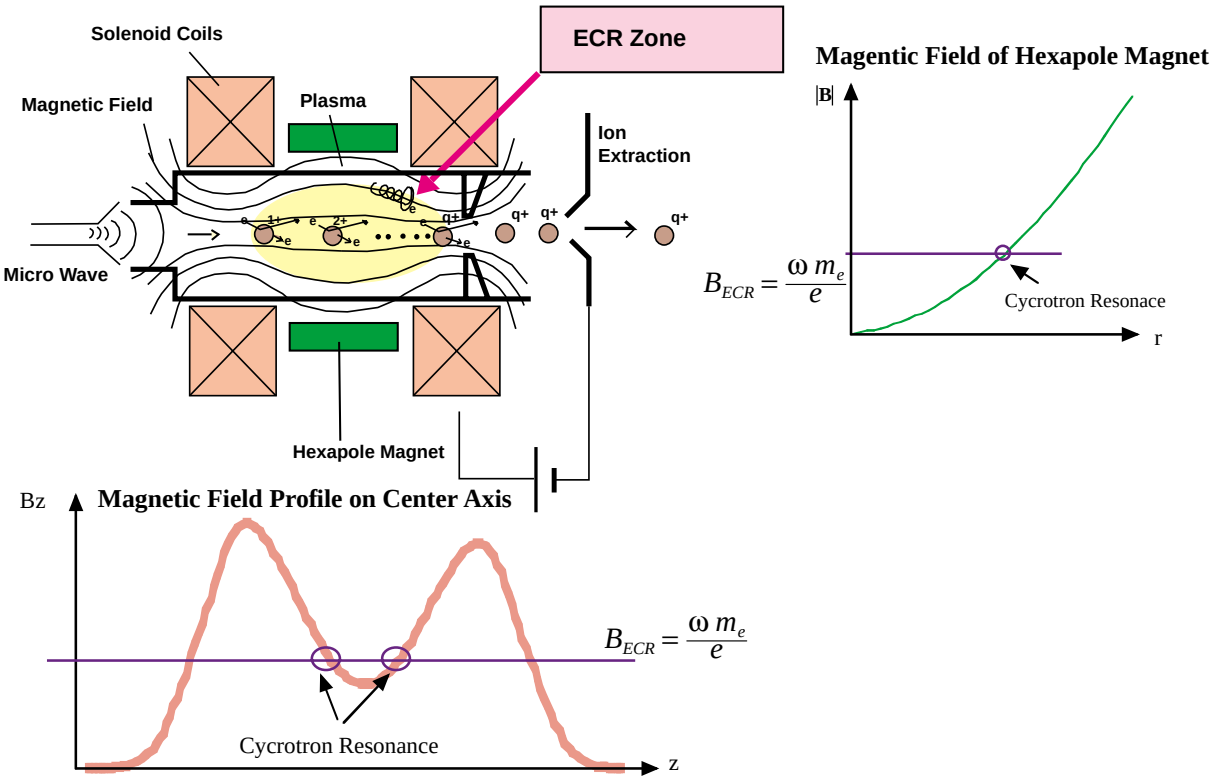

Figure 2.1: A Schematic of an ECRIS

An ECRIS consists of a vacuum chamber, which serves also as a microwave cavity, a set of solenoid coils, which provides a magnetic mirror field for the axial plasma confinement, a hexapole magnet for the radial

plasma confinement and an axial ion extraction system. Microwaves can be coupled into the ion source axially or radially through a wave guide.

Injected microwaves into the chamber interacts resonantly with the electrons of the plasma. The Larmor frequency of the electrons is equal to the frequency of the microwaves so that electrons are accelerated by the wave electric field towards very high energies, which enables the injected atoms and ions to be stripped up to very high charge states. The details of the principle of the electron heating are described in section 2.3.

The ions should be ionized during its confinement (see section 2.5) by the step-by-step ionization process which is the dominant process (see section 2.4). And the energy of the electrons should be higher than the ionization potential of the desired charge state. Consequently, the electron temperature and the electron density are significantly important for producing highly charged ions. For higher values of the electron temperature and the electron density, a better plasma confinement (see section 2.2) is an essential point.

The ions produced in the ECR plasma are extracted and accelerated with a high-voltage potential between the plasma chamber and an ion-extraction electrode.

The details of the physical processes in an ECRIS are described below.

2.2 Plasma Confinement and Magnetic Structure

The plasma confinement on an ECRIS is archived by radial magnetic and axial magnetic mirror fields. The confinement of electrons is essential for ECRIS to produce intense beams of highly charged heavy ions. A higher electron temperature and density given by a better plasma confinement leads to the higher efficiencies of the ionization and the production of highly charged ions.

The reasons why a hexapole magnet is used in addition to a set of solenoid coils are as follows.

In a simple mirror magnetic field (see subsection 2.2.1), the curvature of magnetic field lines are convexity at any region. In such magnetic struc-

ture, the centrifugal force of the plasma due to the particle motion along the curved lines of force causes an interchange instability [10]. It is well known in the field of the fusion plasma that adding a magnetic multipole to a mirror field prevent the interchange instability and reduce radially escaping particles [11] (Fig. 2.2). For this reason, radial magnetic mirrors in additions to an axial mirror are great helpful for confining a plasma. Such magnetic confinement structure is called as "minimum-B" structure (i.e., the magnetic field strength increases in every direction from the center).

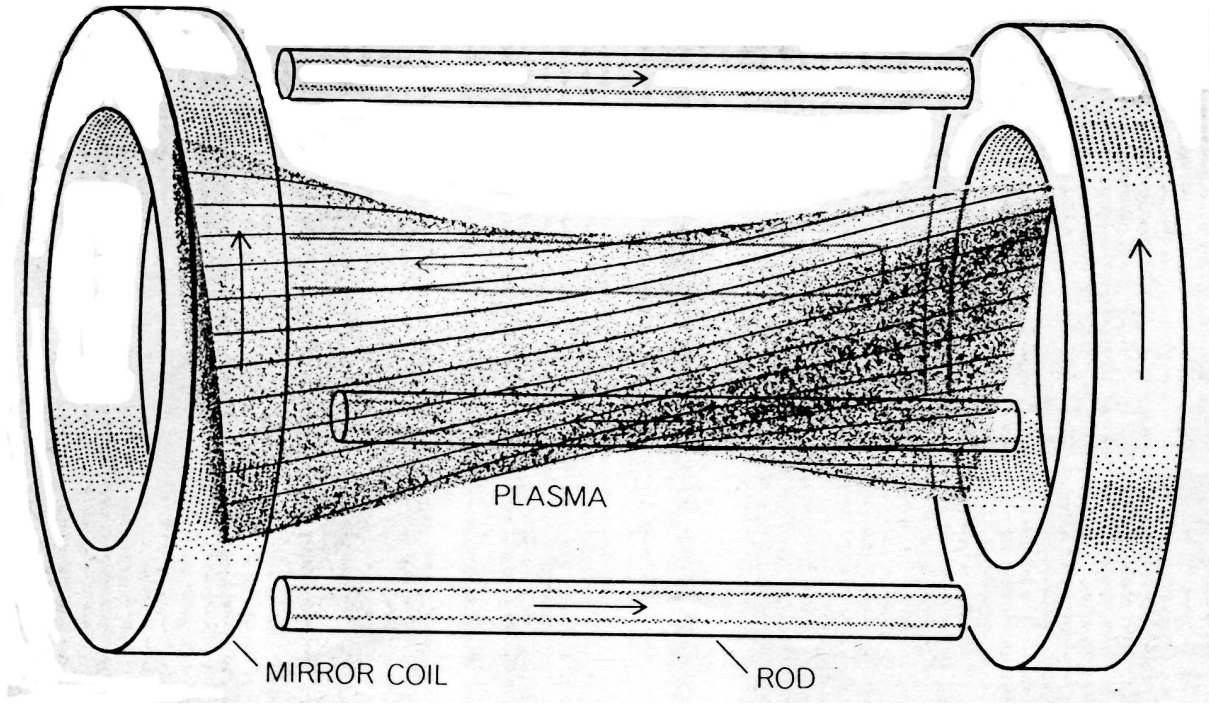

Figure 2.2: "minimum-B" structure can be created by surrounding a mirror-type magnetic field by four rods carrying current [11].

It is considered that the hexapole magnetic is preferred for the radial confinement in an ECRIS. There are two reasons for this consideration. The first is shapes of loss areas which are determined by polarity of the superimposed mirror field, with respect to the ion extraction. As shown in Fig. 2.3, a higher order multipole has larger loss areas at both ends, which are usable for the ion extraction. The loss area of a quadrupole is just a line at the ends, which can not be expected the effective ion extraction. The second is cross-sectional shapes of magnetic field strength, with respect

to the plasma confinement. As shown in Fig. 2.3, the region of a higher magnetic field of an octopole magnet is closer to a chamber wall rather than that of a hexapole magnet. We can expect better plasma confinement to a hexapole magnet rather than an octopole magnet. Therefore, a hexapole magnet is usually used in ECRISs.

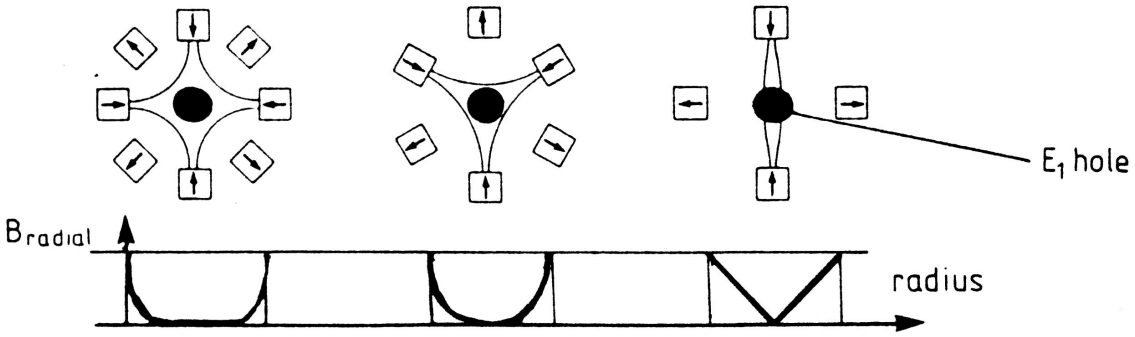

Figure 2.3: Loss areas for octoples, hexapoles, and quadrupoes and corresponding cross-sectional shapes of magnetic field strength [8]

The plasma confinement by a magnetic mirror field which composes minimum-B structure is demonstrated by two keywords, the loss corn and the plasma pressure. The loss corns are holes of a magnetic mirror field, from which charged particles of plasma escape. The size of loss corn is determined by mirror ratio R_m, which is written as

$$\frac{1}{R_m} = \sin^2 \theta_m = \frac{B_{min}}{B_{max}} \tag{2.1}$$

where B_{min} and B_{max} are magnetic field strength at the midplane and the peak of the mirror field, respectively.

On the other, the stable confinement of high density - high temperature plasmas requires not only a high mirror ratio but also an actually high magnetic field. The plasma as magnetic fluid in a magnetic field is approximately governed by relationship of the form:

$$P_{plasma} + \frac{B^2}{2\mu_0} = \text{constant} \tag{2.2}$$

where P_{plasma} is the plasma kinetic pressure written as

$$P_{plasma} = n_e k_B T_e \tag{2.3}$$

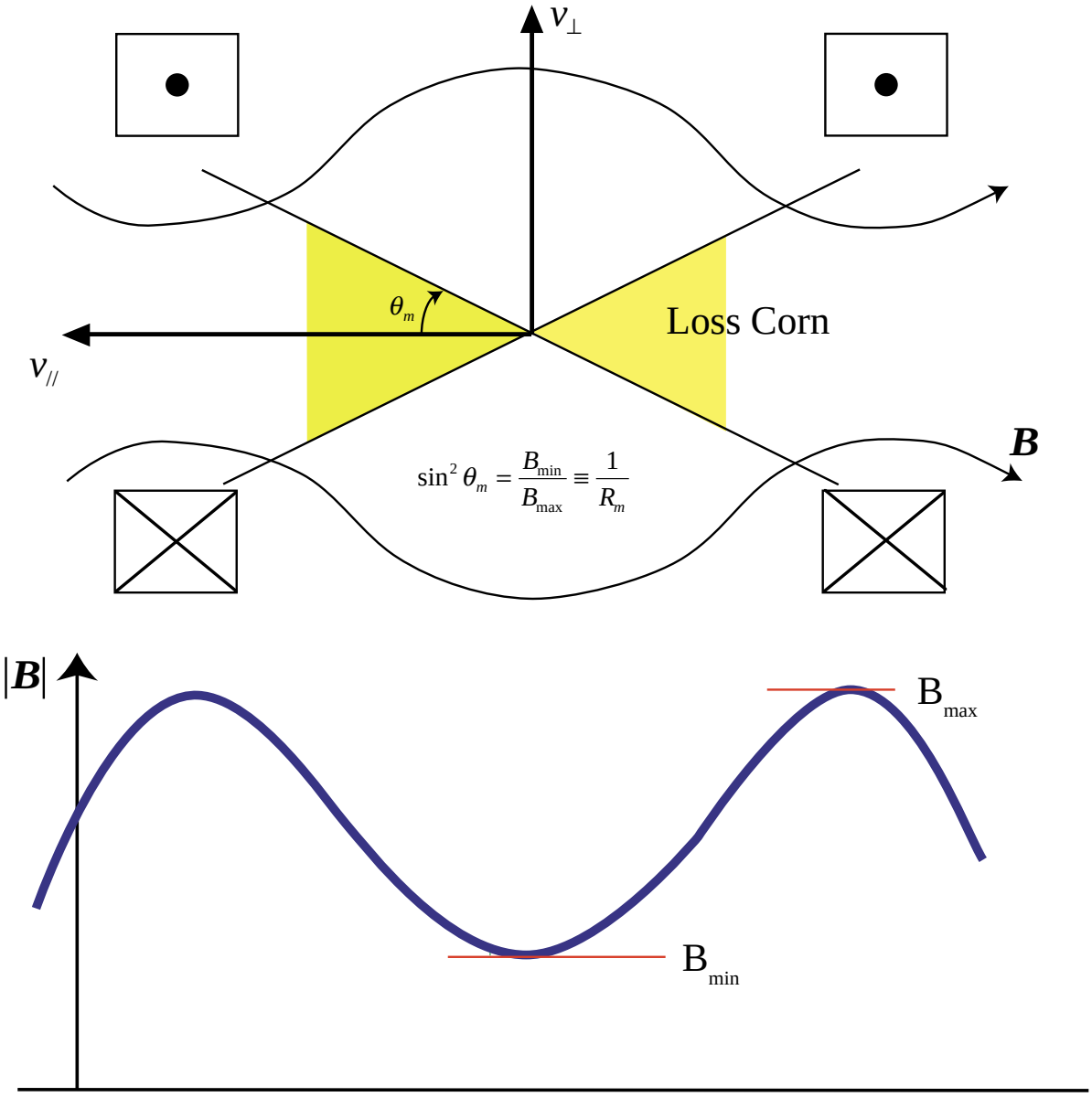

Figure 2.4: The Loss corn of which size is determined by the mirror ratio

The details about the loss corn and the plasma pressure are described in following subsections.

2.2.1 Loss Corn

In this subsection, I describe the derivation of 'loss corn' of mirror magnetic field for the plasma confinement, which is determined by 'mirror ratio'.

We consider a magnetic field which is pointed primarily in the z direction and whose magnitude varies in the z direction. The field is axisymmetric,

with $B_\theta = 0$ and $\frac{\partial B}{\partial \theta} = 0$. Since the lines of force converge and diverge, there is necessarily a component B_r as show in Fig. 2.5.

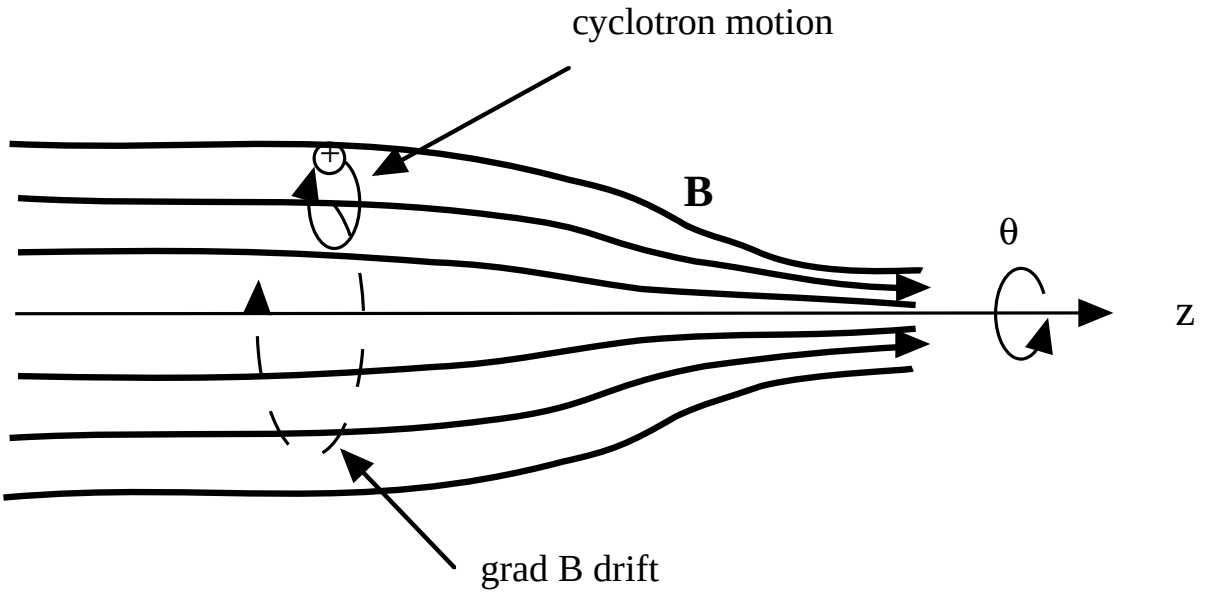

Figure 2.5: Magnetic mirror field and drifts of a particles in the field.

We can obtain B_r from $\boldsymbol{\nabla} \cdot \boldsymbol{B} = 0$:

$$\frac{1}{r}\frac{\partial}{\partial r}(rB_r) + \frac{\partial B_z}{\partial z} = 0 \tag{2.4}$$

From this equation, we lead approximate B_r. If $\frac{\partial B_z}{\partial z}$ is given at $r = 0$ and does not vary much with r, we have B_r of 0 th order approximation as follows.

$$\begin{aligned} \frac{1}{r}\frac{\partial}{\partial r}(rB_r) + \frac{\partial B_z}{\partial z} &= 0 \\ \Leftrightarrow rB_r = -\int_0^r r\frac{\partial B_z}{\partial z}dr &\approx -\frac{1}{2}r^2\frac{\partial B_z}{\partial z} \\ \therefore B_r &= -\frac{1}{2}r\frac{\partial B_z}{\partial z} \end{aligned} \tag{2.5}$$

The components of the Lorentz force are

$$F_r = q(v_\theta B_z - v_z B_\theta) = qv_\theta B_z \tag{2.6}$$

$$F_\theta = q(-v_r B_z + v_z B_r) \tag{2.7}$$

$$F_z = q(v_r B_\theta - v_\theta B_r) = -qv_\theta B_r \tag{2.8}$$

Two terms vanish due to $B_\theta = 0$. F_r and first term of F_θ give rise to the usual Larmor gyration. Second term of F_θ causes a drift in the radial direction at off-axis. F_z is the one we are interested in. Using Eq. 2.5, we obtain

$$F_z = \frac{1}{2} q v_\theta r \frac{\partial B_z}{\partial z} \tag{2.9}$$

We must now average over one gyration. For simplicity, consider a particle whose guiding center lies on the axis. Then $r = r_L$, where r_L is Larmor radius. We assume that v_θ is a constant during a gyration and v_θ is $v_\perp$. When $B > 0$

$$\begin{aligned} q > 0 \ &\rightarrow \ v_\perp < 0 \\ q > 0 \ &\rightarrow \ v_\perp < 0 \end{aligned}$$

therefore

$$q v_\perp = - \left| q v_\perp \right| \tag{2.10}$$

$$r_L = \left| \frac{v_\perp}{q} \right| \frac{m}{B} \tag{2.11}$$

Using Eq. 2.10 and 2.11, the average force is

$$\bar{F}_z = \frac{1}{2} q v_\perp r_\theta \frac{\partial B_z}{\partial z} = -\frac{1}{2} \left| q v_\perp \right| \left| \frac{v_\perp}{q} \right| \frac{m}{B} \frac{\partial B_z}{\partial z} = -\frac{1}{2} \frac{v_\perp^2 m}{B} \frac{\partial B_z}{\partial z} \tag{2.12}$$

We define the magnetic moment of the gyrating particle to be

$$\mu \equiv \frac{\frac{1}{2} m v_\perp^2}{B} \tag{2.13}$$

Using Eq. 2.13, the average force $\bar{F}_z$ can be written as

$$\bar{F}_z = -\mu \left(\frac{\partial B_z}{\partial z} \right) \tag{2.14}$$

In general

$$\boldsymbol{F}_\parallel = -\mu \left(\frac{\partial B}{\partial \boldsymbol{s}} \right) = -\mu \boldsymbol{\nabla}_\parallel B \tag{2.15}$$

where $d\boldsymbol{s}$ is a line element along $\boldsymbol{B}$. The above equation means that the force affect the charged particle from stronger $\boldsymbol{B}$ to weaker $\boldsymbol{B}$.

There is an important law of μ that μ remains invariant when the particle move to any different $\boldsymbol{B}$ location. To probe this, consider the component of the equation of the motion along $\boldsymbol{B}$:

$$\begin{aligned} F_{\parallel} = m\frac{dv_{\parallel}}{dt} &= -\mu\frac{\partial B}{\partial s} \\ \Leftrightarrow mv_{\parallel}\frac{dv_{\parallel}}{dt} &= -\mu\frac{\partial B}{\partial s}\frac{ds}{dt} \\ \Leftrightarrow \frac{d}{dt}\left(\frac{1}{2}mv_{\parallel}^2\right) &= -\mu\frac{\partial B}{\partial t} \end{aligned} \tag{2.16}$$

Here $d\boldsymbol{B}/dt$ is the variation of $\boldsymbol{B}$ as seen by the particle. The equation $v_{\parallel} = \frac{ds}{dt}$ is used. From particle's energy conservation law with Eq. 2.13 and Eq. 2.16, we have

$$\begin{aligned} &\frac{d}{dt}\left(\frac{1}{2}mv_{\parallel}^2 + \frac{1}{2}mv_{\perp}^2\right) = 0 \\ &\Leftrightarrow -\mu\frac{\partial B}{\partial t} + \frac{d}{dt}\left(\mu B\right) = 0 \\ &\Leftrightarrow -\mu\frac{\partial B}{\partial t} + B\frac{d\mu}{dt} + \mu\frac{dB}{dt} = 0 \\ &\Leftrightarrow \frac{d\mu}{dt} = 0 \end{aligned} \tag{2.17}$$

As a particle moves from a weak-field region to a strong field-region in the course of its thermal motion, it sees an increasing B. Therefore its $v_{\perp}$ must increase in order to keep μ constant. On the other hand, to keep total energy in constant, $v_{\parallel}$ must necessarily decrease. $v_{\parallel}$ becomes zero at the location where B is enough high, and the force $\boldsymbol{F}_{\parallel}$ reflects the particle back to the weak-field region. As a result, a plasma can be trapped in nonuniform field which is formed by a simple pair of coils as shown in Fig. 2.6.

The trapping is not perfect. For instance, a particle with $v_{\perp} = 0$ will have not magnetic moment and will not feel any force along $\boldsymbol{B}$. A particle with small $v_{\perp}/v_{\parallel}$ at the midplane ($B = B_{min}$) will escape if the maximum field B_{max} is not large enough. This fact is derived as follows.

A particle with $v_{\perp} = v_{\perp 0}$ and $v_{\parallel} = v_{\parallel 0}$ at the midplane will have $v_{\perp} = v'_{\perp}$ and $v_{\parallel}$ at its turning point. The magnetic field at the turning point is B'.

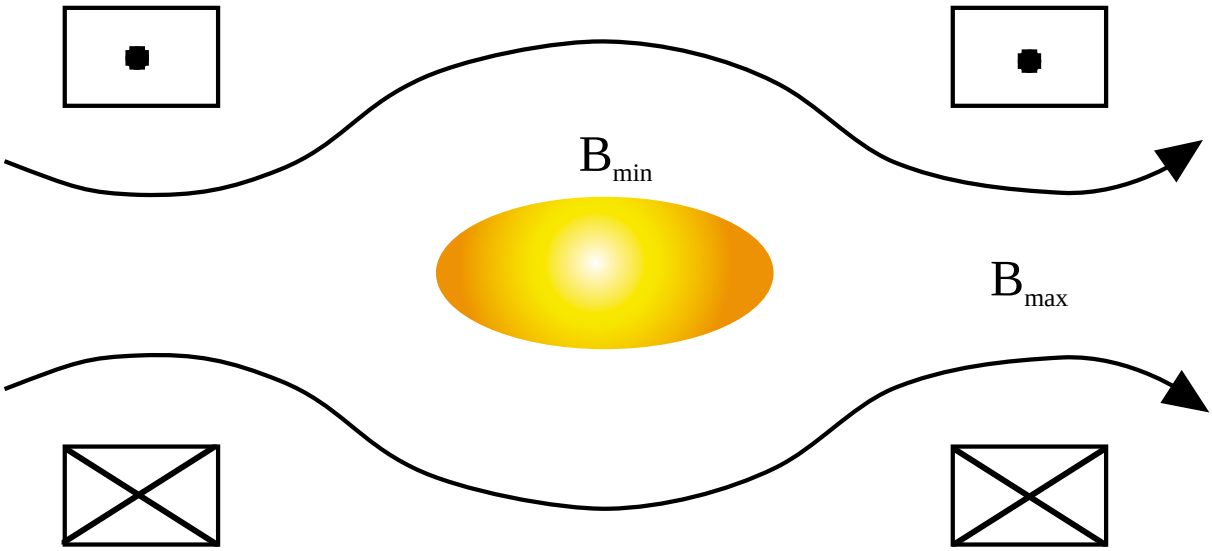

Figure 2.6: A plasma trapped between magnetic mirrors

The the invariance of μ yields

$$\frac{\frac{1}{2}mv_{\perp 0}^2}{B_{\min}} = \frac{\frac{1}{2}mv'^2_{\perp}}{B'} \tag{2.18}$$

The energy conservation law requires

$$\begin{aligned} &\frac{1}{2}mv_{\perp 0}^2 + \frac{1}{2}mv_{\parallel 0}^2 = \frac{1}{2}mv'^2_{\perp} \\ &\Leftrightarrow v_{\perp 0}^2 + v_{\parallel 0}^2 = v'^2_{\perp} = v_0^2 \end{aligned} \tag{2.19}$$

Combining Eqs. 2.18 and 2.19, we find

$$\frac{B_{\min}}{B'} = \frac{v_{\perp 0}^2}{v'^2_{\perp}} = \frac{v_{\perp 0}^2}{v_0^2} \equiv \sin^2\theta \tag{2.20}$$

where θ is the pitch angle of the orbit in the midplane. The above equation means that particles with smaller θ will mirror in regions of higher B , and in the case where B' exceed B_{max} due to too small θ, the particle does not mirror at all.

Replacing B' by B_{max} is Eq. 2.20, we obtain the smallest θ of a confined particle, which is given by

$$\sin^2\theta_m = \frac{B_{\min}}{B_{\max}} \equiv \frac{1}{R_m} \tag{2.21}$$

where R_m is called the 'mirror ratio'. Equation 2.21 defines the boundary of a region in velocity space in the shape of a cone, which is called a 'loss

corn' (Fig. 2.4). Particles lying within the loss cone are not confined. Note that the loss cone is independent of q and m.

Without collision, particles outside loss corn well confined. When collisions occur, particles are lost when they are scatted into the loss corn. For better plasma confinement, we need to reduce the probability that particles come into loss corn, i.e., higher mirror ration is desirable.

2.2.2 Plasma Pressure

In previous subsection, I describe the principle of plasma confinement. In this subsection, I derive that confinement of high pressure plasma, i.e., high density and high temperature plasma requires not only mirror ratio but also high magnetic field.

We can consider a plasma as a single fluid which have mass density ρ an electrical conductivity $1/\eta$, instead of composition of two interpenetrating fluid. The plasma as a single fluid is described by the equation of magnetohydrodynamics(MHD).

$$\rho\frac{\partial \boldsymbol{v}}{\partial t} = \boldsymbol{j} \times \boldsymbol{B} - \boldsymbol{\nabla} p \tag{2.22}$$

where $\boldsymbol{v}$, $\boldsymbol{j}$ and p are mass velocity , current density and pressure of plasma, respectively. For a steady state with $\frac{\partial v}{\partial t} = 0$, the plasma must satisfy

$$\boldsymbol{\nabla} p = \boldsymbol{j} \times \boldsymbol{B} \tag{2.23}$$

Equation 2.23 states that there is a balance of forces between the pressure-gradient force and Lorentz force. To clear how this comes about, consider a cylindrical plasma with ∇p directed toward the axis as show in Fig. 2.7.

To counteract the outward force of expansion, there must be an azimuthal current in the direction shown in Fig. 2.7. The derivation of the required magnitude of the current is as follows.

The cross product of Eq. 2.23 with $\boldsymbol{B}$

$$\boldsymbol{B} \times \boldsymbol{\nabla} p = \boldsymbol{B} \times (\boldsymbol{j} \times \boldsymbol{B}) = \boldsymbol{j} B^2 - \boldsymbol{B}\,(\boldsymbol{B} \cdot \boldsymbol{j}) \tag{2.24}$$

If $\boldsymbol{j} = \boldsymbol{j}_\perp$ is perpendicular to $\boldsymbol{B}$, we obtain

$$\boldsymbol{j}_\perp = \frac{\boldsymbol{B} \times \boldsymbol{\nabla} p}{B^2} = (k_B T_i + k_B T_e)\,\frac{\boldsymbol{B} \times \boldsymbol{\nabla} n}{B^2} \tag{2.25}$$

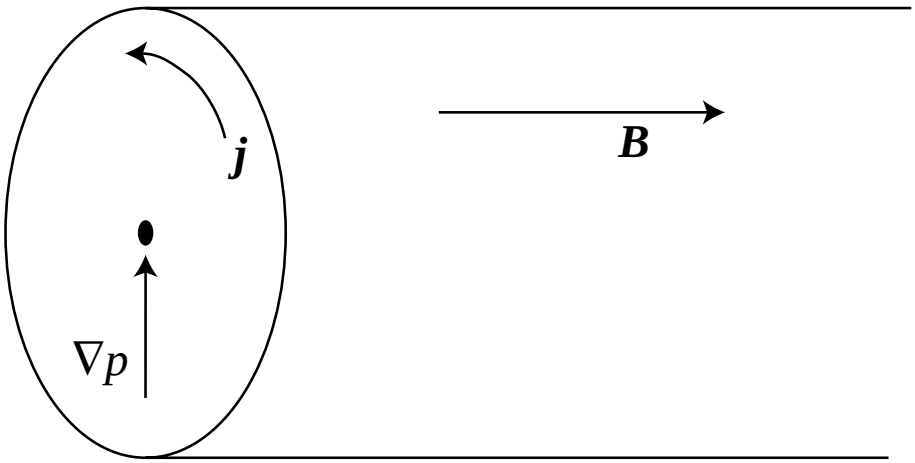

Figure 2.7: The $\boldsymbol{j} \times \boldsymbol{B}$ force of the diamagnetic current balances the pressure-gradient force in steady state

This current is called 'the diamagnetic current'. The diamagnetic current flow in the direction to decrease the magnetic field in plasma. The relation between magnetic field strength and plasma pressure can be derived as follows.

From Maxwell's equations

$$\boldsymbol{\nabla} \times \boldsymbol{B} = \mu_0 \boldsymbol{j} \tag{2.26}$$

We substitute Eq. 2.26 into Eq. 2.23 to obtain

$$\begin{aligned} \boldsymbol{\nabla} p &= \frac{1}{\mu_0} (\boldsymbol{\nabla} \times \boldsymbol{B}) \times \boldsymbol{B} = \frac{1}{\mu_0} \left[(\boldsymbol{B} \cdot \boldsymbol{\nabla}) \boldsymbol{B} - \frac{1}{2} \boldsymbol{\nabla} B^2 \right] \\ \Leftrightarrow \boldsymbol{\nabla} &\left(p + \frac{B^2}{2\mu_0} \right) = \frac{1}{\mu_0} \left[(\boldsymbol{B} \cdot \boldsymbol{\nabla}) \boldsymbol{B} \right] \end{aligned} \tag{2.27}$$

In many interesting cases, such as a straight cylinder with axial field, the right-hand side vanishes or is small. Then in almost cases, Eq 2.27 says that

$$p + \frac{B^2}{2\mu_0} = \text{constant} \tag{2.28}$$

where $\frac{B^2}{2\mu_0}$ is the magnetic field pressure known as 'Maxwell stresses'. Equation 2.28 says that the sum of the particle pressure and magnetic field pressure is a constant. In plasma with a density gradient (Fig. 2.8), the magnetic field must be low where the density is high, and vice versa. The

decrease of the magnetic field inside the plasma is caused by diamagnetic current as mentioned above.

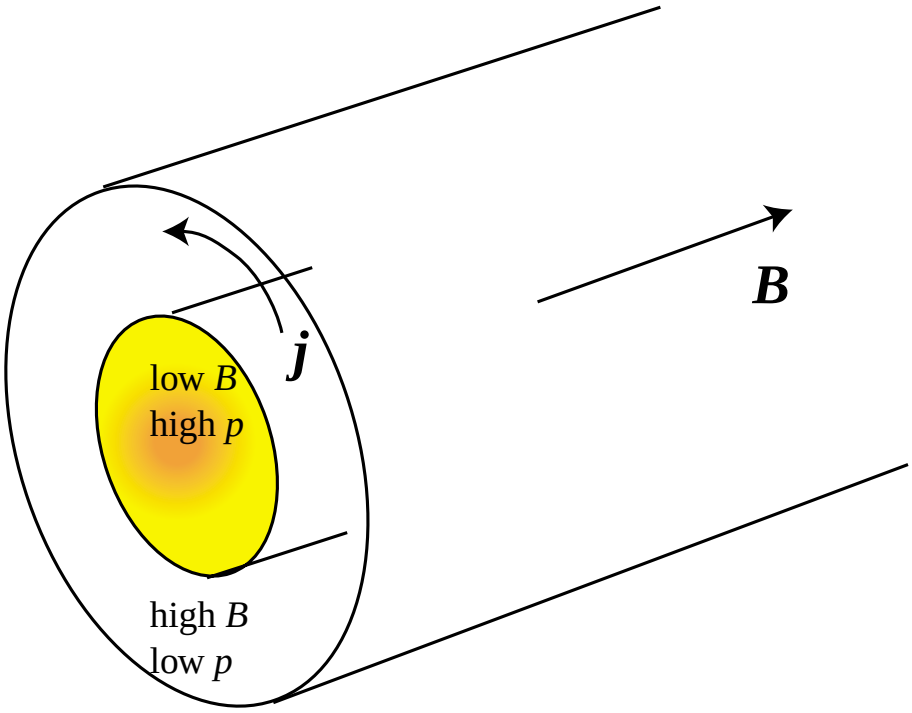

Figure 2.8: In a finite-β plasma, the diamagnetic current decreases the magnetic field. keeping the sum of the magnetic and particle pressures a constant.

The size of the diamagnetic effect is indicated by the ration of the two terms in Eq. 2.28. This ratio is usually denoted by β:

$$\beta = \frac{\sum nk_BT}{B^2/2\mu_0} = \frac{\text{Particle pressure}}{\text{Magneitc field pressure}} \tag{2.29}$$

If β is high, the local value of B can be greatly reduced by the plasma. When $\beta = 1$,there are two regions: a region of plasma with out field, and a region of field without plasma. This equilibrium would likely be unstable.

As a result, it is necessary for stable plasma confinement to keep β low. For low β of high pressure plasma, i.e., high density and high temperature plasma, absolute magnetic field strength is required.

2.3 Electron Heating

The electrons resonantly absorb energy from an electromagnetic wave whose frequency ω is equal to the gyrofrequency ω_c of the electrons at a particular

surface which is called the resonance surface; the equation of the surface is given by;

$$\omega_c = \frac{eB}{m_e} \tag{2.30}$$

with e, m_e the electron charge and mass, respectively. This resonant absorption mechanism is called 'Electron Cyclotron Resonance (ECR)'.

Each time an electron passes through a cyclotron resonant zone, it gains perpendicular energy from the resonant microwave field, its magnetic moment increase and its tuning point is shifted toward the midplane as described below. Their acceleration is strongly dependent on the phase difference between the electron cyclotron motion and the right-hand circularly polarized component of the electromagnetic field [10]. If the phase difference is zero, the electron will be accelerated, but if the phase difference is 180°, the electron will be decelerated.

In order to obtain the temporal evolution of the hot-electron component, one has to calculate the motion of an individual electron for a given time including occasionally many successive resonance-zone crossings, and to average over the motion of many electrons, i.e., to average over many individual phase differences.

The gain of perpendicular velocity by one transit through the resonant zone can be written as, [12, 13]

$$\Delta v_{\perp r} = \frac{e}{m} E_{\perp}^{0} T e^{i(\phi_0 - \theta_0)} \tag{2.31}$$

where ϕ_0 and θ_0 are initial phases of electric field and gyromotion of electron respectively. $E_{\perp}^{0}$ is perpendicular amplitude of electric field to background magnetic field. $|T|$ is effective resonance time, which is written as,

$$T = \int_{-\infty}^{\infty} \exp\left[-i\left(\omega_\mu t + \int_0^t \Omega\left(t\right) dt\right)\right] dt \tag{2.32}$$

Over a time of many transits through the resonant zones, the particles perform an random walk in energy which results in time averaged heating. The models of this type are referred as 'stochastic heating', because an element fo randomness is necessary in order to prevent the wave phase and particle gyrophase from becoming correlated on successive passes through

the resonant zone. This wave-plasma interaction can be modeled as a diffusive process in velocity space. The diffusion paths at resonant zone show in Fig. 2.9. $v_{\perp r}$ and $v_{\parallel r}$ indicate perpendicular component and parallel component of electron's velocity at resonant zone, respectively.

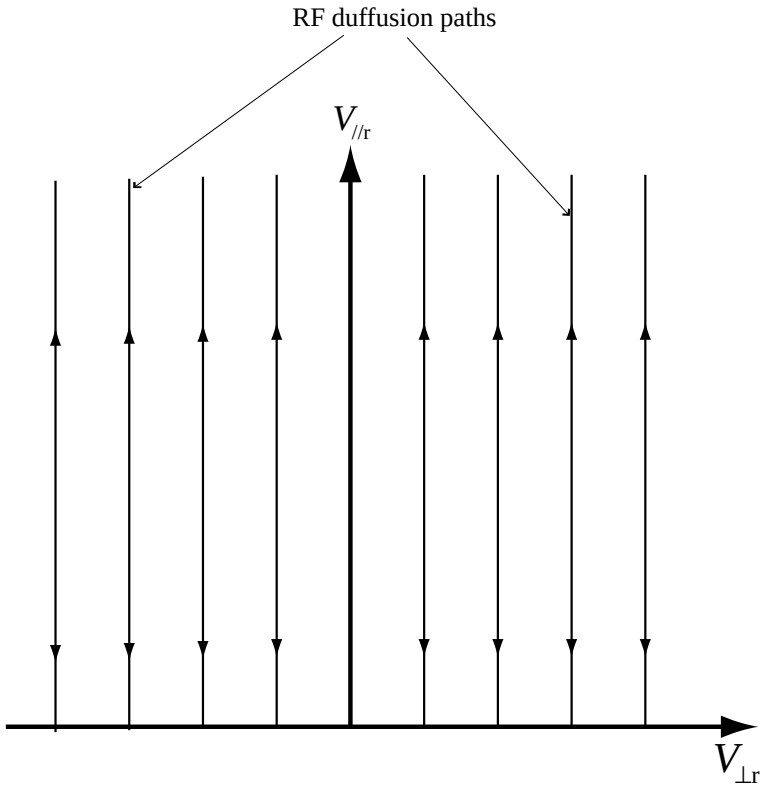

Figure 2.9: The diffusion paths of electrons at resonant zone.

The accelerated electrons move along a magnetic field line to the location which have a different magnetic field strength. The motion of electrons in magnetic field governed by energy conservation low and magnetic moment conservation which are written as follows.

$$\epsilon = \frac{m}{2}\left(v_{\perp r}^2 + v_{\parallel r}^2\right) = \frac{m}{2}\left(v_{\perp}^2 + v_{\parallel}^2\right) \tag{2.33}$$

$$\mu = \frac{m}{2}\frac{v_{\perp r}^2}{B_r} = \frac{m}{2}\frac{v_{\perp}^2}{B} \tag{2.34}$$

From these equation, the diffusion paths at the location with magnetic field strength B is written as follows.

$$v_{\parallel}^2 = v_{\parallel r}^2 + \left(\frac{B_r}{B}\right) v_{\perp}^2 \tag{2.35}$$

The diffusion paths seen from the midplane are shown in Fig. 2.10. In Fig. 2.10, We find that some heated electrons are kicked off from loss corn, i.e., confinement of hot electrons are improved.

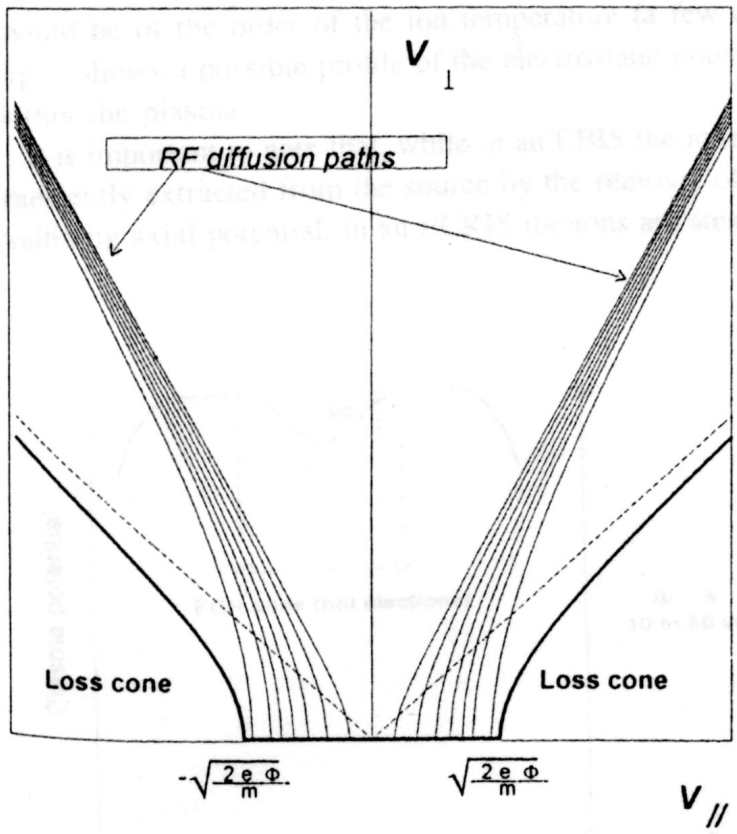

Figure 2.10: The diffusion paths of electrons seen from midplane [14].

In general, the time development of distribution function $f(\boldsymbol{A})$ formed through random walk of vector $\boldsymbol{A}$ can be described by Fokker-Plank equation.

$$\frac{\partial f}{\partial t} = -\frac{\partial}{\partial \boldsymbol{A}}\left\{\left\langle\frac{\Delta \boldsymbol{A}}{\Delta t}\right\rangle f(\boldsymbol{A})\right\} + \frac{1}{2}\frac{\partial}{\partial \boldsymbol{A}} : \left\{\left\langle\frac{\Delta \boldsymbol{A} : \Delta \boldsymbol{A}}{\Delta t}\right\rangle f(\boldsymbol{A})\right\} \quad (2.36)$$

Using equation 2.31, the Fokker-Plank equation on velocity space can be written as,

$$\frac{\partial f}{\partial t} = \frac{1}{4}\frac{1}{v_{\perp r}}\frac{\partial}{\partial v_{\perp r}}\left\{v_{\perp r}\frac{\partial}{\partial v_{\perp r}}\left(\frac{\left\langle|\Delta v_{\perp r}|^2\right\rangle}{\tau}\right) f(v_{\perp r})\right\} \quad (2.37)$$

where τ is a cycle of velocity gain $\Delta v_{\perp r}$.

To estimate τ, the mirror magnetic field is approximated by a parabolic curve as follows.

$$B(z) = B_{\min}\left(1 + z^2/L^2\right)$$

where B_{min} and L are a magnetic field strength at midplane and a distance resonant zone, respectively. In this mirror field, the electron motion can be treat as a simple harmonic motion. As a result, the cycle of transit of resonant zone is written as,

$$\tau = \frac{\pi L\sqrt{R_r}}{v_{\perp r}} \tag{2.38}$$

where R_r is mirror ratio between the midplane and the resonant zone.

$$R_r = \frac{B_r}{B_{\min}} \tag{2.39}$$

Under Eq. 2.37 and 2.38, we can obtain the velocity distribution after time t.

$$f\left(v_{\parallel r}, v_{\perp r}, t\right) = \frac{1}{atv_{\perp r}} e^{-\frac{v_{\perp r}}{at}} \int_0^\infty du f^{(0)}\left(v_{\parallel r}, u\right) u e^{-\frac{u}{at}} I_0\left(2\frac{\sqrt{uv_\perp}}{at}\right) \tag{2.40}$$

$$a = \frac{\left(eE_\perp^0/m\right)^2}{2\Omega_e^L\sqrt{R_r}}\frac{1}{v_{\parallel r}}$$

$$\Omega_e = \frac{e}{m}\frac{dB}{dz}$$

where I_0 and $f^{(0)}$ are the modified Bessel function and the initial velocity distribution of electrons, respectively.

Figure 2.11 shows the time development of velocity distribution calculated from Eq. 2.40. The initial distribution is assumed as Maxwell distribution.

The velocity distribution of electrons heated by ECR have a higher tail at high energy region than Maxwell distribution. This is caused by Eq. 2.38 where the frequency of transit through resonant zone increase with $v_{\perp r}$. As a result, hot electron component of ECR plasma is created effectively in mirror magnetic field.

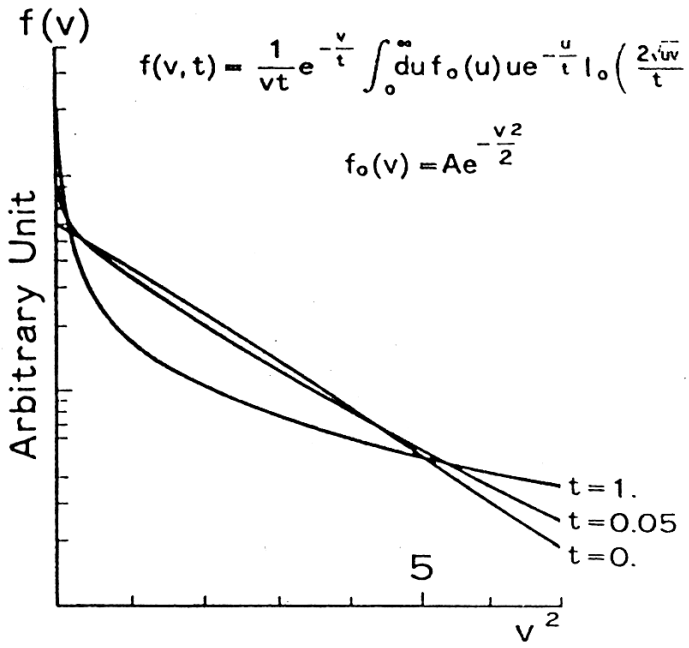

Figure 2.11: The velocity distribution of electrons heated by ECR and its time development [12]

2.4 Ionization Mechanism of Highly Charged Ions

The probability of producing high charged ions by a single electron impact falls of rapidly with increasing charge state of ions. Therefore the only efficient way to obtain a reasonable yield of highly charged ions is by successive ionization [15, 14]. If the single collision, multiple-ionization process contribute negligibly to total ion production, the ionization process can be describe following rate equation [16]. The Ionization process in ECR plasma have been considered as follows.

$$\frac{dn_i}{dt} = n_e\langle\sigma\nu\rangle_{i-1\to i} n_{i-1} + n_n\langle\sigma\nu\rangle_{i+1\to i} n_{i+1} - n_e\langle\sigma\nu\rangle_{i\to i-1} n_i - n_n\langle\sigma\nu\rangle_{i\to i+1} n_i - \frac{n_i}{\tau_i} \quad (2.41)$$

where the right hand side terms stand respectively for the creation term of charge i through ionization of charge $(i-1)$ and through charge exchange of charge $(i+1)$ with neutrals, and the loss term thorough ionization towards charge $(i+1)$ and charge exchange with neutrals of charge i, and the losses due to diffusion out side the plasma. The system was solved under various

assumptions (constant electron temperature T_e, constant electron density n_e, constant pressure n_0). Remarkable agreement between experiments and theory could be found as seen from Fig. 2.12 [16].

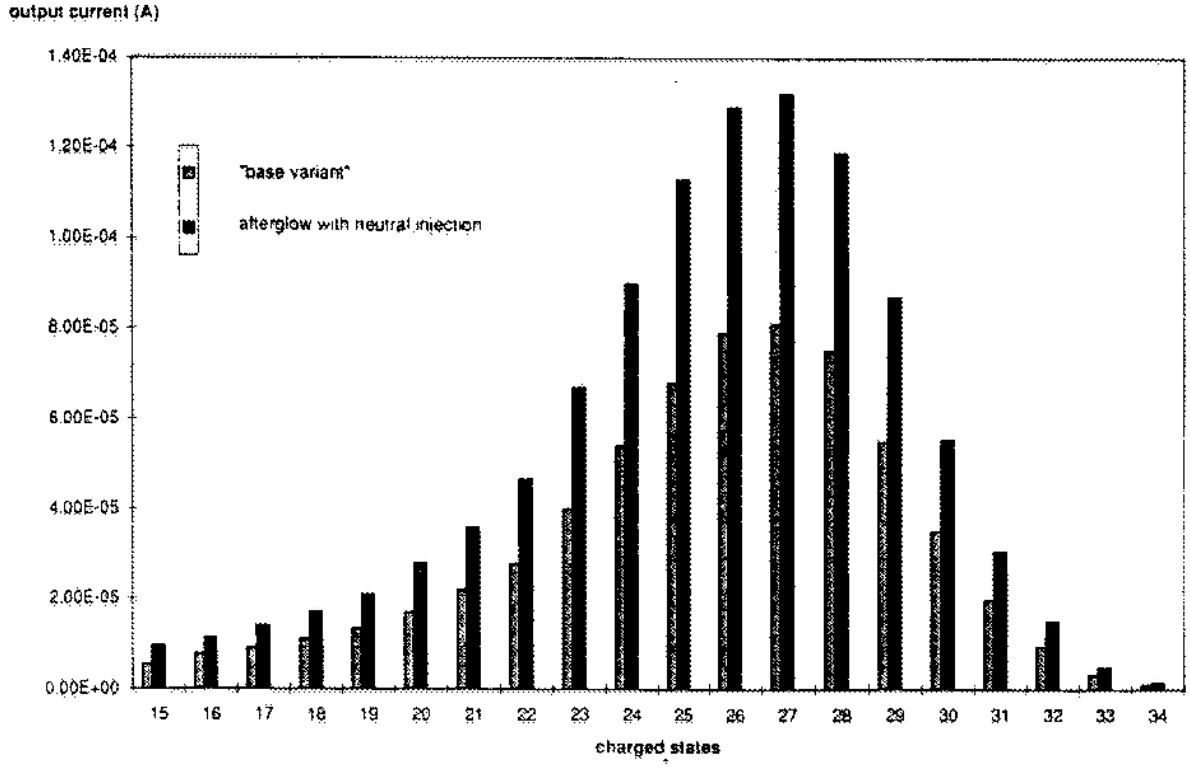

Figure 2.12: Calculated and measured Charge State Distribution of in Lead ions the afterglow mode [16]

2.5 Ion Confinement and Afterglow

The electron confinement time becomes longer with increasing the perpendicular energy of electrons, which is given by the ECR heating as described in section 2.3. Then the electrons will be mainly confined by magnetic fields. On the other hand, the mechanism to improve magnetic confinement of ions does not exists. The ions are confined in the electronic cloud by a self electrostatic well.

More precisely, in any device containing a hot plasma, the central plasma is isolated from the metallic wall by an electron cloud making sheath. This sheath is due to the high mobility of electrons compared to the ions. The

electrons leave the central plasma more rapidly than the ions, so the central plasma is naturally biased with a positive potential ϕ_0 with respect to the wall (see Fig. 2.13) [10]. The positive potential ϕ_0 is called "plasma potential". In an ECR ion source, we can consider that the central plasma shows a depressed negative potential $\Delta\phi$ as shown in Fig. 2.13[17]. The potential dip $\Delta\phi$ is induced by a relatively high density of hot electrons created by ECR heating and trapped in minimum B magnetic field. The ions which overcome the potential dip can be extracted from plasma.

The negative potential dip $\Delta\phi$ created by the hot electrons can be evidenced by a sharp current peak observed at the RF power turn off. At this time the hot electron cloud partially collapses and being no longer sustained by the RF field. As a consequence, the ion losses temporary increase as shown in Fig. 2.14. This kind of current is called the afterglow current. The current in steady-state operation is called the steady-state current against to the afterglow current.

To describe the relation between the afterglow current and the steady-state current, we assume following items.

1. The ion temperature T_i of the different ion species in the source is uniform, since ion-ion collision time τ_{ii} is such that $\tau_{ii} \ll \tau_i$, where τ_i is ion confinement time.

2. The ion temperature will never reach a value greater than several tens of eV, since $\tau_i \ll \tau_e$ (equipartition time between electrons and ions).

3. The velocity distribution of ions follows a Maxwellian distribution.

From the third assumption, the ion density n_{i0} at the central plasma can be written as,

$$n_{i0} = A \int_{-\infty}^{\infty} \exp\left(\frac{-\frac{1}{2}mv^2}{k_B T_i}\right) dv \tag{2.42}$$

Generally, the Maxwellian distribution of Z_i charge state particles at potential $\Delta\phi$ can be written as,

$$A\exp\left(\frac{-\left(\frac{1}{2}mv^2 + Z_i\Delta\phi\right)}{k_B T_i}\right) \tag{2.43}$$

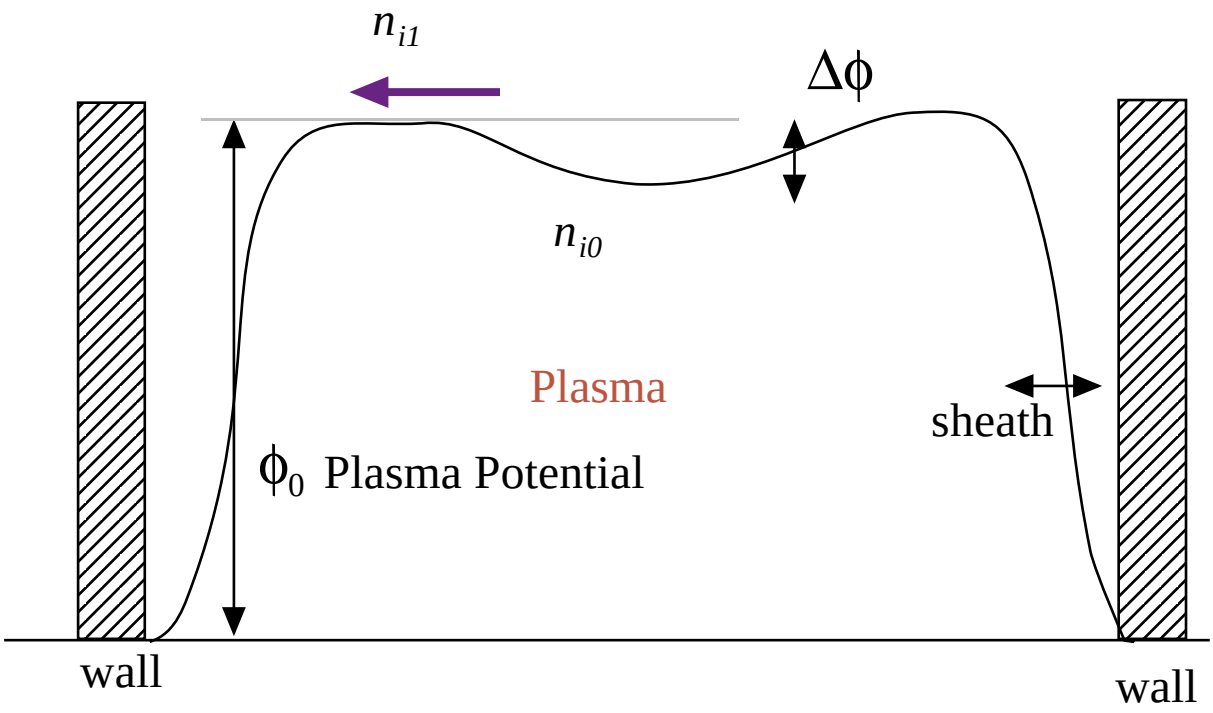

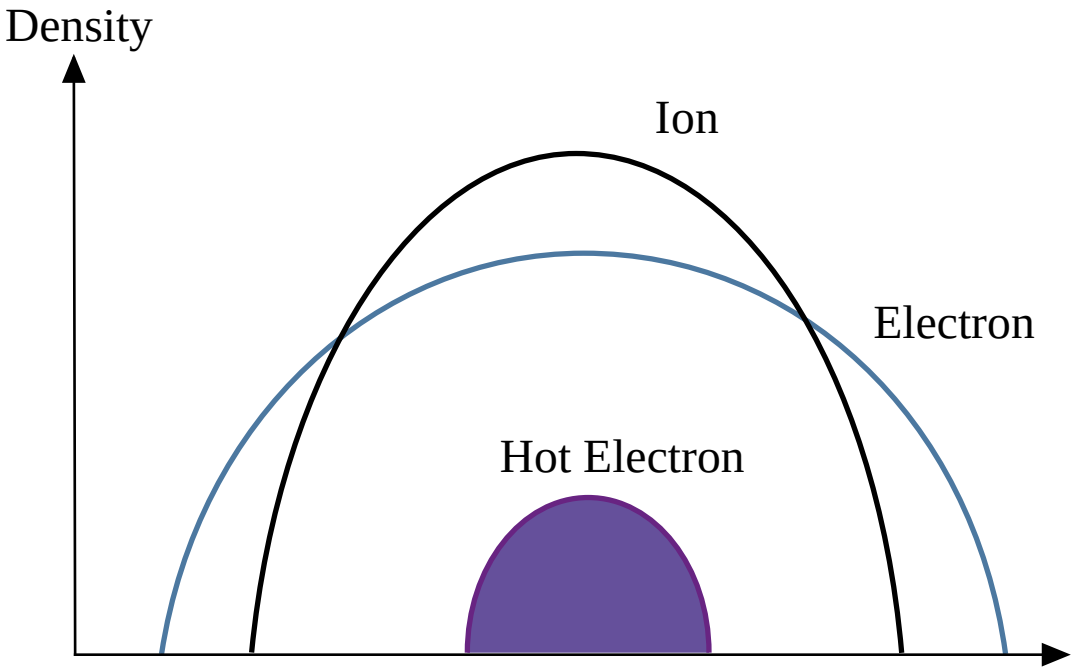

Figure 2.13: Electrostatic potential, Ions and electrons distribution in ECR plasma.

Then the ion density n_{i1} at the edge of potential dip can be written as,

$$n_{i1} = A\int_{-\infty}^{\infty} \exp\left(\frac{-\left(\frac{1}{2}mv^2 + Z_i\Delta\phi\right)}{k_B T_i}\right) dv = n_{i0}\exp\left(\frac{-Z_i\Delta\phi}{k_B T_i}\right) \quad (2.44)$$

If the steady-state current I_{steady} and afterglow current $I_{afterglow}$ are

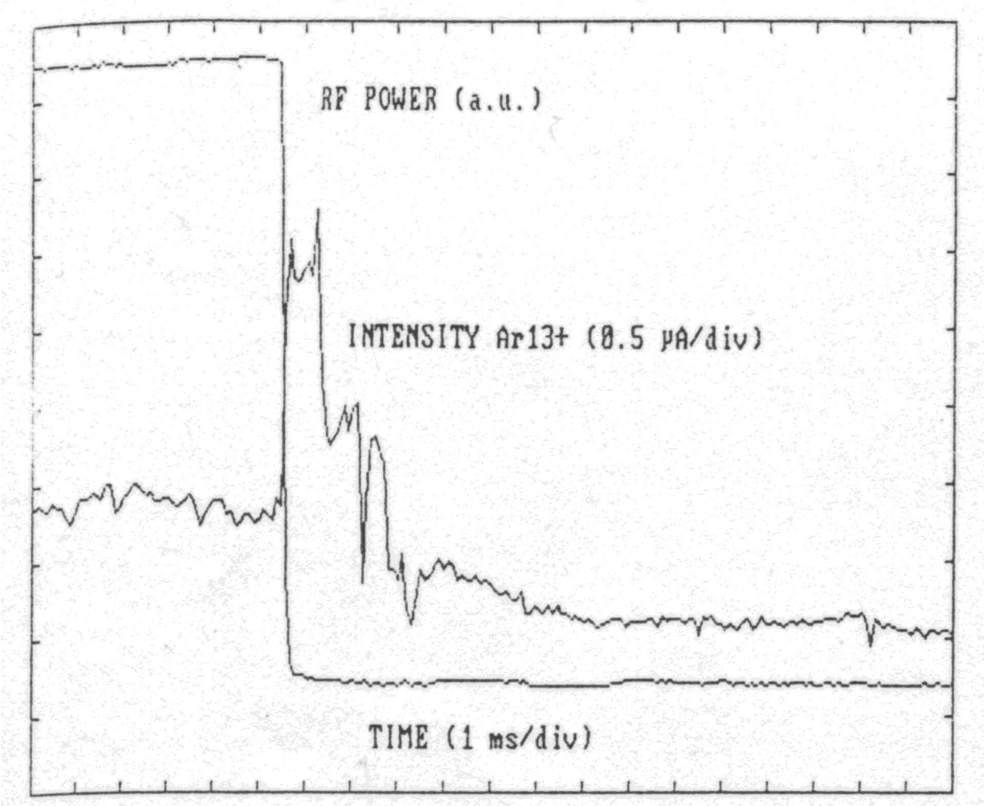

Figure 2.14: RF signal and extracted Ar^{13+} intensity vs time [18]

proportional to n_{i0} and n_{i1} respectively, we can verify that

$$\frac{I_{afterglow}}{I_{steady}} \propto \exp\left(\frac{Z_i \Delta\phi}{k_B T_i}\right) \tag{2.45}$$

If we have an homogeneous density and temperature for any ionic species, this ratio must be proportional to $exp\,(Z_i)$. The experimental results are show in Fig. 2.15 and 2.16 . The expected tendency can be shown.

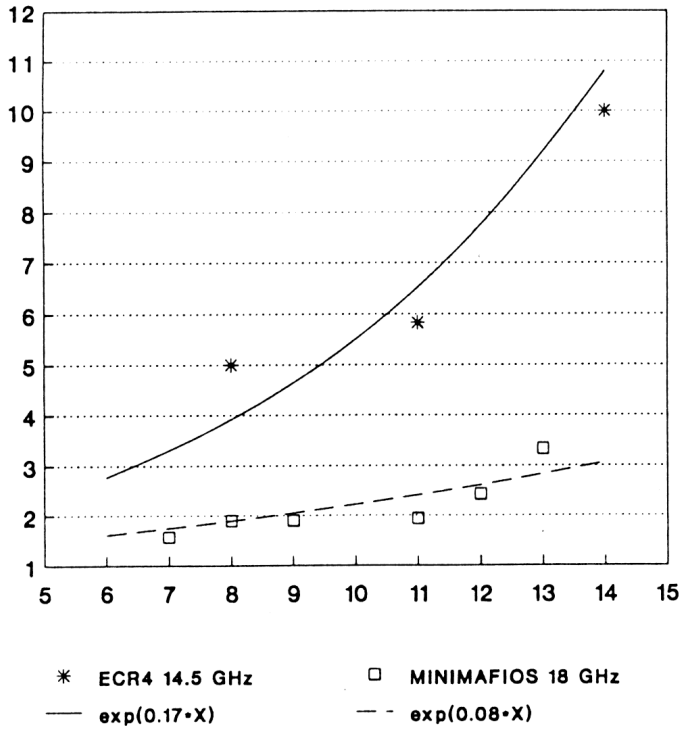

Figure 2.15: Ratio of the afterglow current to the steady-state current of the argon ions [17].

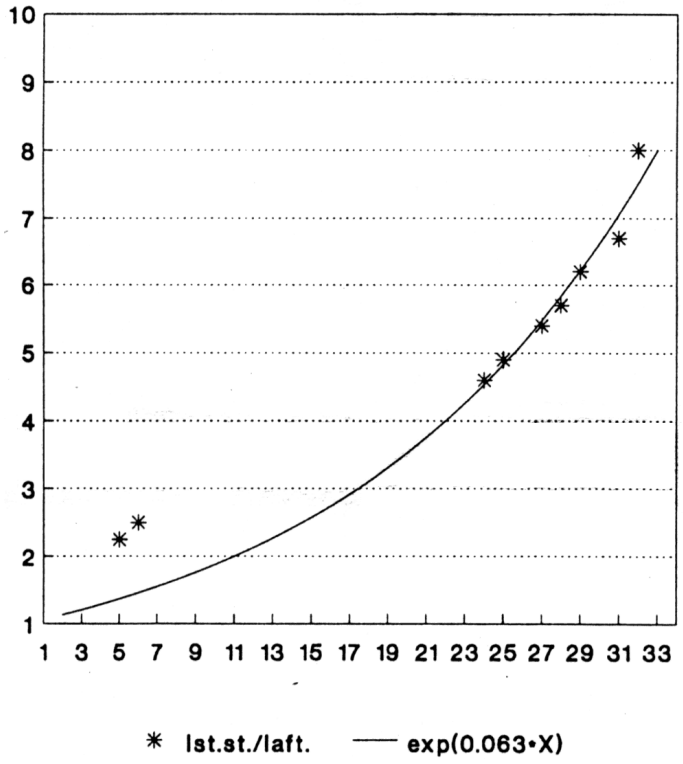

Figure 2.16: Ratio of the afterglow current to steady-state current for lead ions (charges 5 and 6 correspond to oxygen ions when the source is tuned for lead) [17]

Chapter 3

Experiments to Research Biased Electrode Effects

3.1 Prologue

As described before (see section 2.4), highly charged ions are effectively yielded mainly through the successive ionization process. Therefore, to obtain highly charged heavy ions, it is crucial to prolong the exposure time of the ions in the electron cloud and to increase the density of ionizing electrons. To fulfill these requirements, many laboratories have made efforts by using various methods [19, 8]. One of these methods is to install a biased or floating electrode into the plasma chamber of the ion source [8]. The details of the biased electrode method are described in following section (see section 3.2).

On the other hand, for increasing the beam intensity, sometimes we need to shorten the ion confinement time (keeping its value, of course, higher than the ionization time). As a result, there exists an optimal confinement time for every ion species. As described in section 2.5, ion confinement time is strongly governed by the depth of the plasma potential dip. The measurement of afterglow- and steady-state currents under the pulsed mode operation of the microwaves provides information of potential dip in ECR Plasma [8]. Using this method , we can obtain the information of ion confinement time.

Toward design of new superconducting ECRIS, we research the effects of biased electrode to ion confinement time. The superconducting ECRIS have a strong magnetic field which may cause longer ion confinement than

optimal confinement time. In this chapter, I described the experiments and its results to examine the effect of an electrode on the plasma potential dip using the pulsed mode operation.

The experiments are performed highly charged Kr ions produced from the RIKEN 18 GHz ECRIS. The contents of this chapter were published as ref.[20].

3.2 A Biased Electrode in ECRISs

The effect of a biased electrode to ECRIS was initially demonstrated by the Grenoble ECRIS group [21]. A negatively biased electrode has been successfully used in many laboratories to increase the beam intensity of highly charged heavy ions [21, 22, 23].

Increase of ion currents under insertion of the biased electrode is often explained in terms of boosting electron density in ECR plasma due to injection of cold secondary electrons from the electrode to discharge, which, in turn, results in increased density of highly charged ions in plasma. However, the experiments results[24, 23, 25] with floating potential electrode without bias voltage indicate that more careful analysis of the phenomenon is required.

3.3 Description of RIKEN 18 GHz ECRIS with a Biased Electrode

The design and performance of the RIKEN 18 GHz ECRIS without using an electrode are described in ref.[26]. Main parameters of this ECRIS are listed as follows.

- Maximum magnetic field strength of mirror field : $\sim$ 1.4 T
- Minimum magnetic field strength of mirror field : $\sim$ 0.47 T
- Mirror ratio : 2.8
- Hexapole magnet on inner surface of plasma chamber: 1.25 T

- Microwave frequency : 18 GHz
- Maximum microwave power: 1.5 kW
- Inner diameter of plasma chamber : 74 mm

Figure 3.1 shows the schematic drawing of the RIKEN 18 GHz ECRIS with a stainless steel electrode. The diameter and thickness of the electrode are 13 and 1 mm, respectively. It is possible to apply a negative bias voltage between the electrode and plasma chamber as show in Fig. 3.1. It is also possible to use the electrode at the floating potential by disconnecting it from the electric power supply.

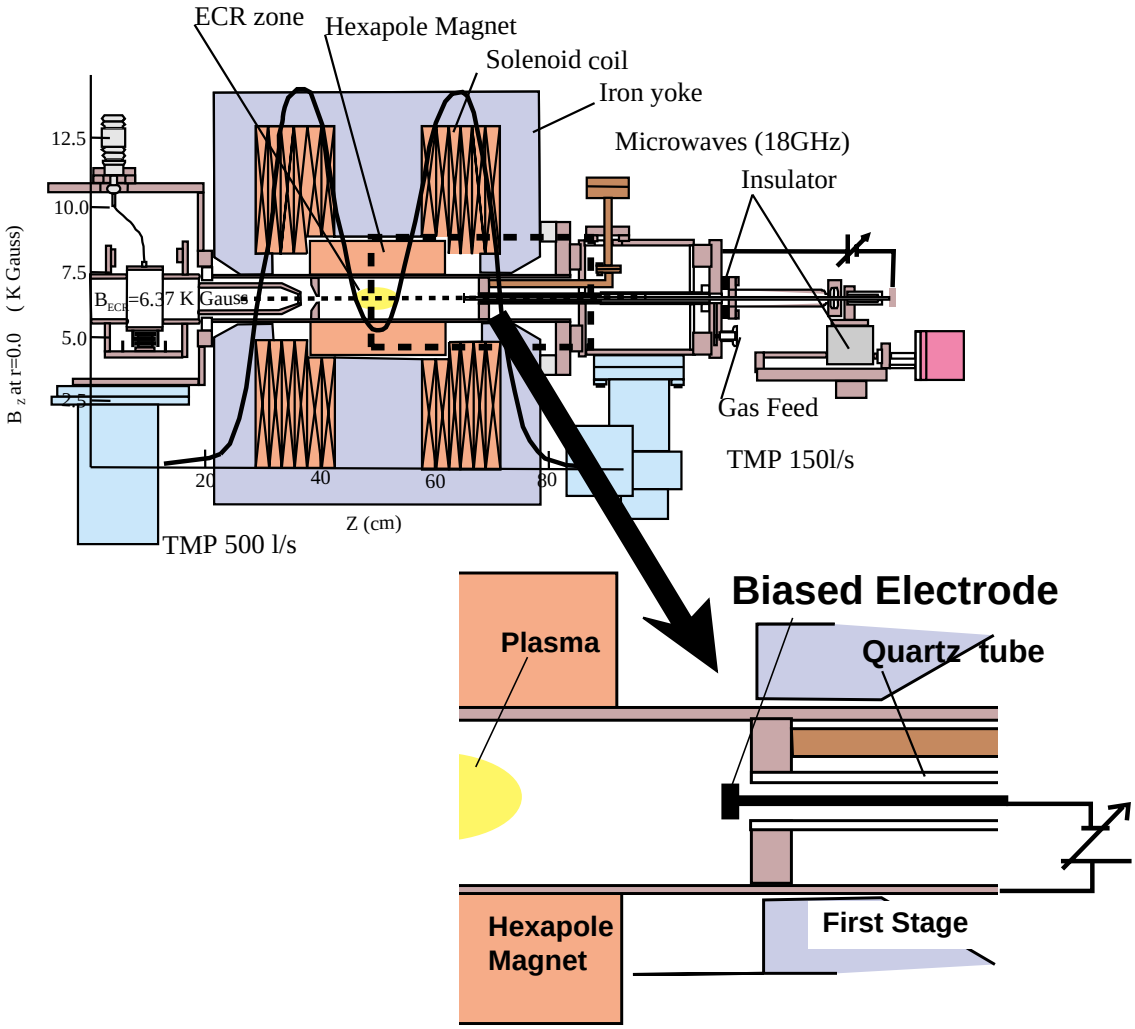

Figure 3.1: a cross-sectional view of the RIKEN18 GHz

In this experiment, we used the electrode at the floating potential. The electrode was placed at the point of maximum magnetic field strength in the axial direction, the most suitable position for increasing the beam intensity. Krypton gas was used as the ionized gas. We used oxygen as the mixing gas to produce the mixing gas to produce the Krypton ions. The extraction voltage was 13 kV.

3.4 Beam Intensity of Kr Ions with and without The Use of The Electrode

Under the CW mode operation of the injected microwaves, we measured the charge state distributions of Kr ions and beam intensities of $Kr^{18,20+}$ as a function of the microwave power. The most suitable conditions for tuning the ion source to produce Kr^{18+} ions are listed in Table 3.1 for both cases, i.e., without and with electrode (condition I and II). In condition III, we kept the same parameters of condition II, but no electrode was used. In this condition, the electrode was removed from the plasma chamber without changing any other parameters. It should be noted that as listed in Table 3.1, when using the electrode (condition II), the maximum mirror magnetic field strength is higher than that when not using it (condition I) as the optimum condition.

Table 3.1: Parameters for production of Kr^{18+} under condition I,II, and III

	gas pressure (Torr)	maximum mirror magnetic field strength (B_{max})	electrode position
condition I	7×10^{-7}	1.25	no electrode
condition II	8.1^{-8}	1.4	at B_{max}
condition III	8.1^{-8}	1.4	no electrode

Figure 3.2 shows the beam intensities of $Kr^{18,20+}$ ions increase with increasing microwave power. At a microwave power of $\sim$ 700 W, we obtained 50 eμA of Kr^{20+} and 95 eμA of Kr^{18+}, which almost twice as high as those obtained without using the electrode (condition I).

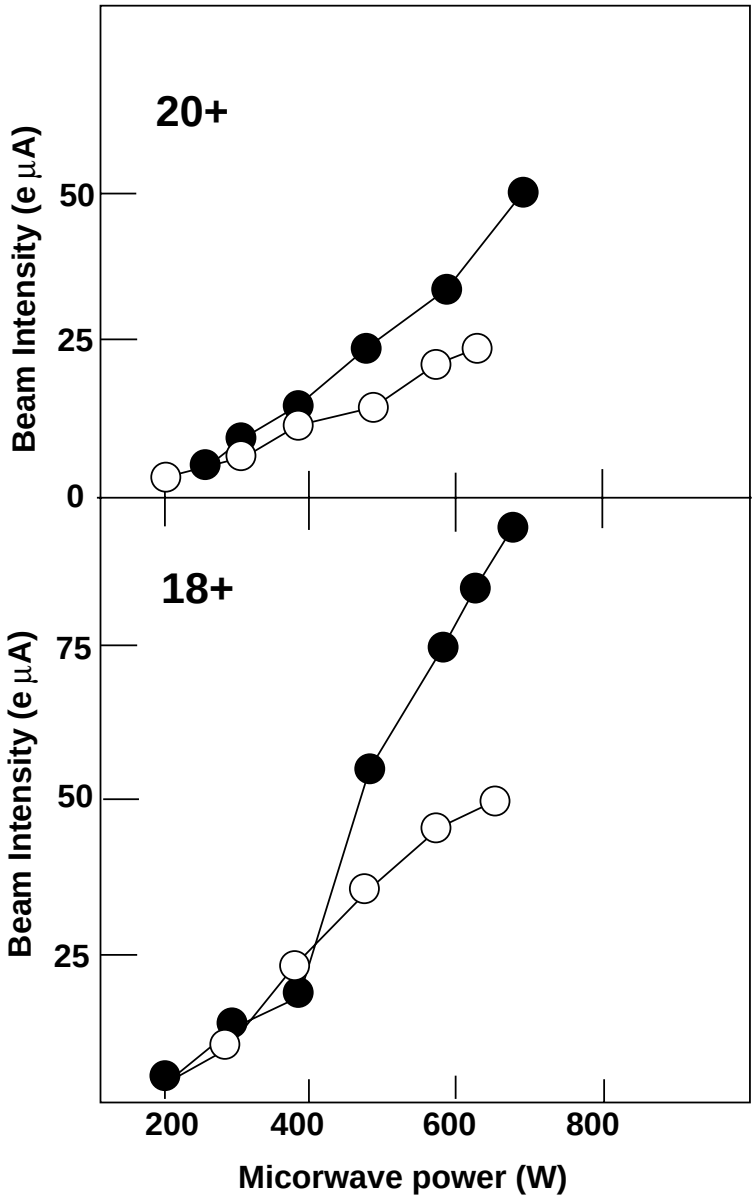

Figure 3.2: Beam intensities of $Kr^{18+,20+}$ ions as a function of the microwave power. Open and closed circles are the results obtained without the use of the electrode (condition I) and with the use of the electrode (condition II)

Figure 3.3 shows the charge distributions of Kr ions when we tuned the ion source to produce Kr^{18+} ions. Closed circles and squares are the results for conditions I and II, respectively. Open squares are the results for condition III.

Figure 3.4 shows the beam intensity of the highly charged Kr ions. Closed and open circles are the results obtained with and without the use of the electrode.

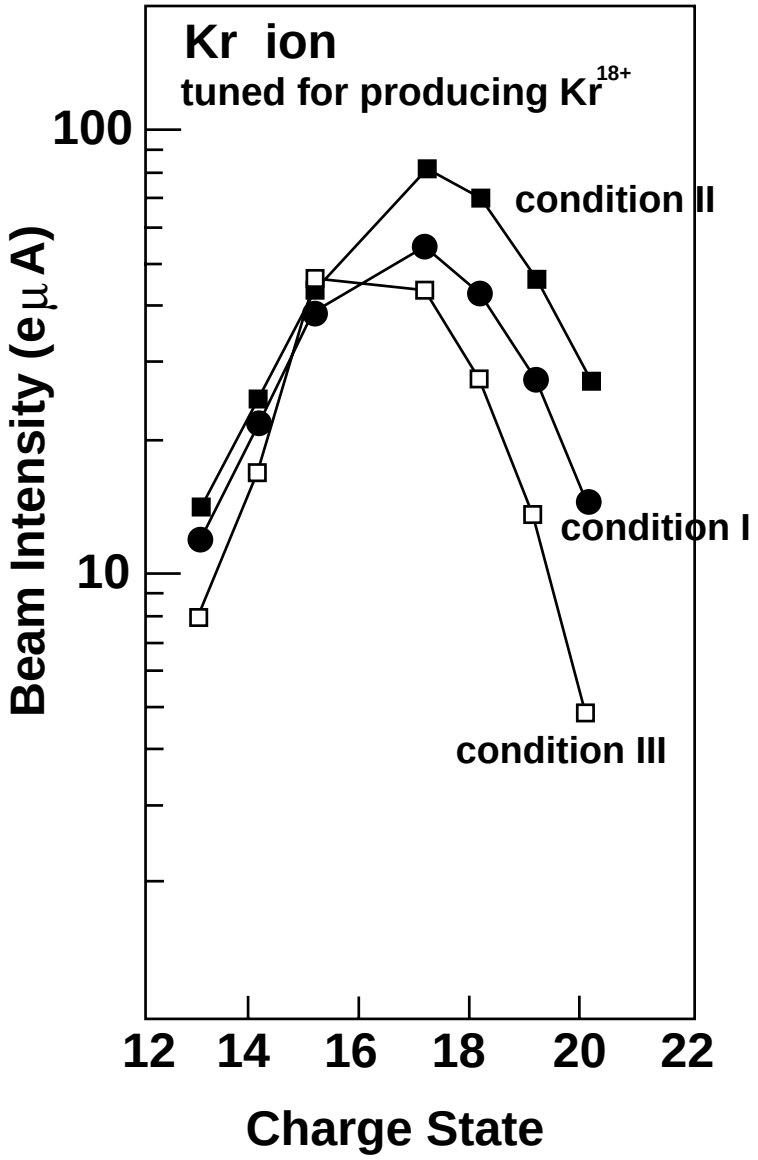

Figure 3.3: Charge distributions of Kr ions; the ion source was tuned to produce Kr^{18+}. Closed circles, squares and open squares are the results under condition I,II and III, respectively.

The above figures shows that the beam intensities obtained with the use of the electrode are always higher than those obtained without it.

3.5 Experimental Results and Discussions for Pulsed Mode Operation

As mentioned in section 2.5, if the central plasma shows a potential dip, the ratio between $I_{afterglow}$ and I_{steady} in pulsed mode operation can be

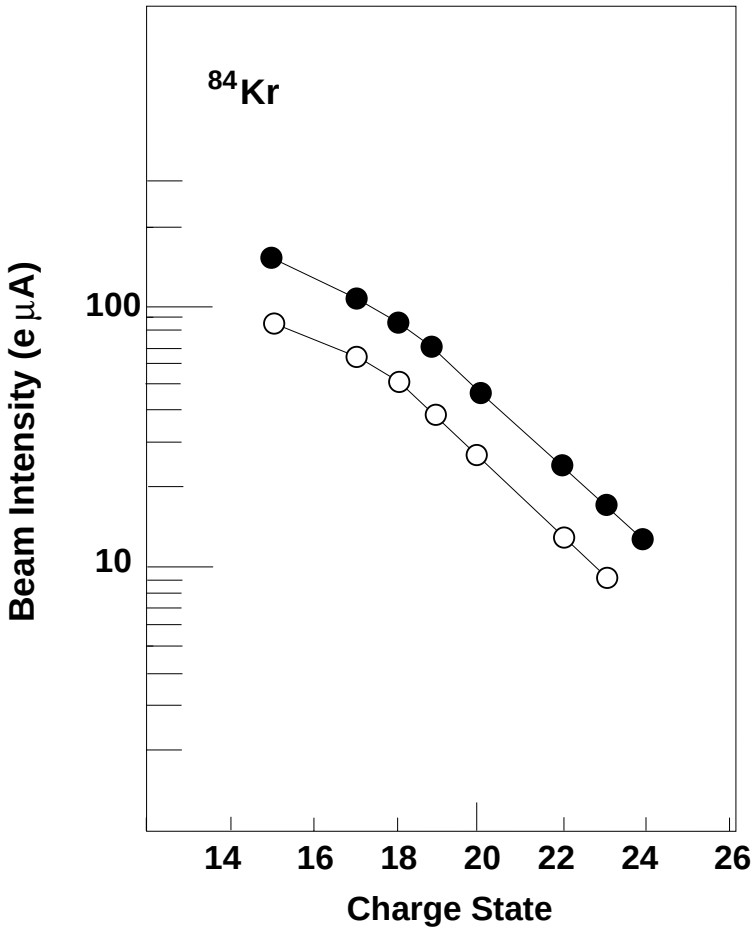

Figure 3.4: Beam intensities of highly charged Kr ions as a function of the charge state. Open and closed circles are the best results obtained with and without the use of the electrode, respectively.

written as,

$$\frac{I_{afterglow}}{I_{steady}} = \exp\left(\frac{q\Delta\phi}{k_B T_i}\right) \tag{3.1}$$

where q, $\Delta\phi$ and T_i are the charge state of ions, depth of potential dip and ion temperature, respectively. Using Eq. 3.1, we examine the value of $\Delta\phi/k_B T_i$. We measured the ratio of the $I_{afterglow}$ to I_{steady} for the charge states from 12+ to 20+ for three conditions (I, II and III) under the duration of 50 ms. Figure 3.5 shows the ratio of $I_{afterglow}$ and I_{steady} as a function of the charge state. Open squares, closed squares and closed circles are the results for under condition I, II and III, respectively. From Eq. 3.1, $\Delta\phi/k_B T_i$ under condition II is smallest. The largest one is obtained under condition III.

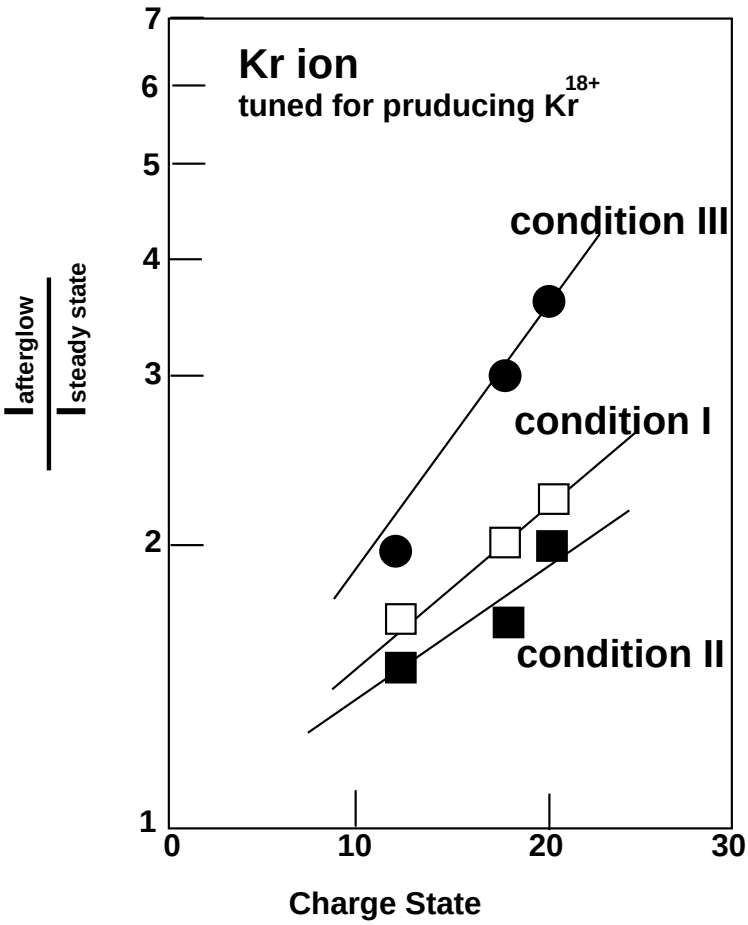

Figure 3.5: Ratio of afterglow current to steady-state current as a function of the charge state. Open squares and closed circles are the results obtained under conditions 1 and 2 and 3 respectively.

Figure 3.6 shows $I_{afterglow}$ and I_{steady} for Kr^{18+} for the three conditions. The afterglow-current obtained under condition II is almost the same as that obtained under condition III. On the other hand, the steady-state current obtained under condition II is much higher than that obtained under conditions III.

As mentioned in section 2.5, the ion confinement of highly charged ions in written by

$$\tau_q \propto \exp\left(\frac{q\Delta\phi}{k_B T_i}\right) \tag{3.2}$$

The extracted ion current(I_q) from ECRIS can be written as,

$$I_q \propto n_q q r^2 L/\tau_q \tag{3.3}$$

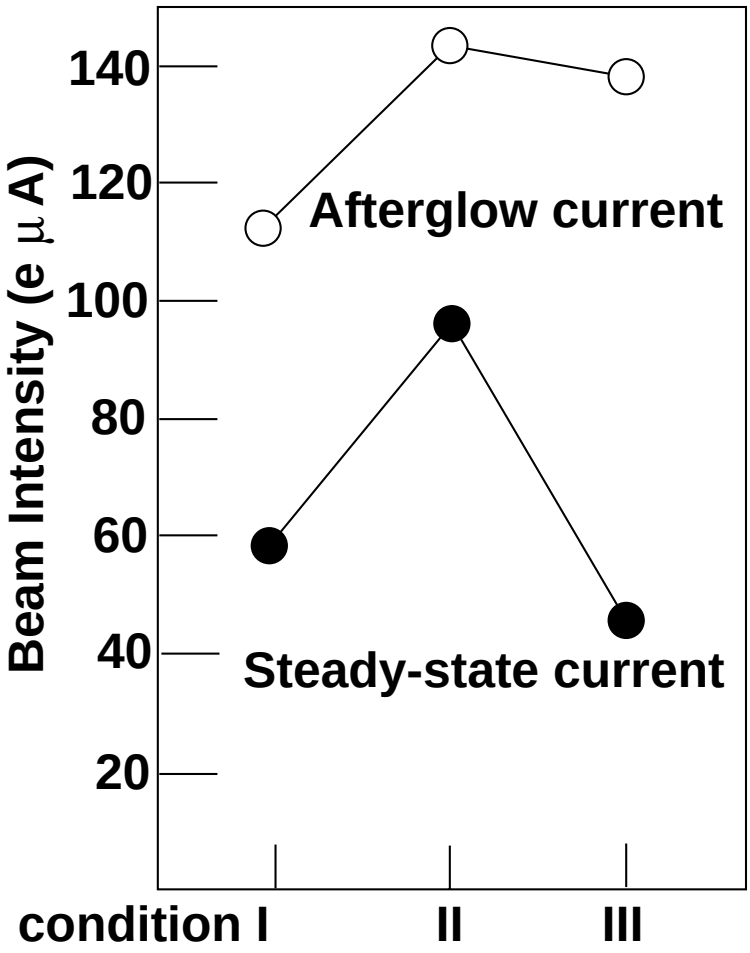

Figure 3.6: Afterglow current (open circles) and steady-state current (closed circles) of Kr^{+18} for conditions I, II and III.

where n_q, r, L and τ_q are the density of ions, average radius of plasma, length of plasma and ion confinement time, respectively. From these equations, it is concluded that the difference between the I_{steady} under condition II and II is due to the difference in ion confinement time. In order to obtain a higher current of ions, the ion confinement time should be shorter for a fixed n_q, r and L. On the other hand, the ion confinement time should be longer than the ionization time(τ_i). When we reduce the ion confinement time but keep it longer than the ionization time for a fixed n_q, r and L, the ion current increases.

In the case of condition I, the ion confinement time is almost the same as that under condition II, but $I_{afterglow}$ is smaller. Meaning that the density of Kr^{18+} ions under condition I is smaller than that under condition II.

We had to use a weaker mirror magnetic field strength to obtain the best results without using an electrode. It seems that the weaker magnetic field results in a shorter ion confinement time and lower ion density of highly charged ions.

In condition II, we can additionally control the plasma conditions by using the electrode, that is, it possible to obtain a higher electron density by increasing the magnetic field strength and to adjust the ion confinement time by inserting the electrode into the plasma. As a result, we obtain an intense beam of highly charged heavy ions.

3.6 Summary

We successfully produced an intense beam of highly charged Kr ions using an electrode. Under the pulsed mode operation, we observed that the density of highly charged Kr ions and ion confinement time increase with increasing mirror magnetic field strength. We also observed that the plasma potential dip changes with insertion of an electrode. Consequently, when we increase the mirror magnetic field strength and insert the electrode into plasma, the beam intensities of highly charged ions increase. From these experimental results, we conclude that the biased electrode will help effective ion extraction and it is surely needed to extract intense beam of highly charged heavy ions from the superconducting ECRIS which has a stronger magnetic field strength than the RIKEN 18 GHz ECRIS.

Chapter 4

Design of Superconducting ECR Ion Source

4.1 Using Liquid-He-Free Superconducting Magnet

As mentioned in section 2.1, a high magnetic field can be expected to provide intense highly charged ion beam. For making a strong magnetic field, superconducting magnet is an effective choice. Superconducting magnets can provide strong magnetic field which can not be achieved by room temperature magnets. Normally liquid Helium is required for cooling the superconducting magnets. It complicates the design of magnets and the operation of sources and requires external facilities for managing it. To avoid their difficulties, we adopt liquid Helium free superconducting magnet using compact refrigerators for our ECR ion source. We have chosen the Gifford-McMahon(G-M) type refrigerator[27] to cool the magnets, which is more reliable and longer-lived than the other of refrigerators. Figure 4.1 shows the cross-sectional view and working process of the G-M type refrigerator.

Superconducting magnets using compact refrigerators give us great advantage comparing to room temperature magnets. It can supply higher magnetic field with low electric power and cooling water consumption. As as example, The comparison between room temperature magnets and superconducting magnets using liquid Helium free cryostat are listed in Table 4.1.

Due to the limit of cooling power at 4.2 K (about 1 W), we have to adopt a hybrid magnetic configuration which consist of superconducting

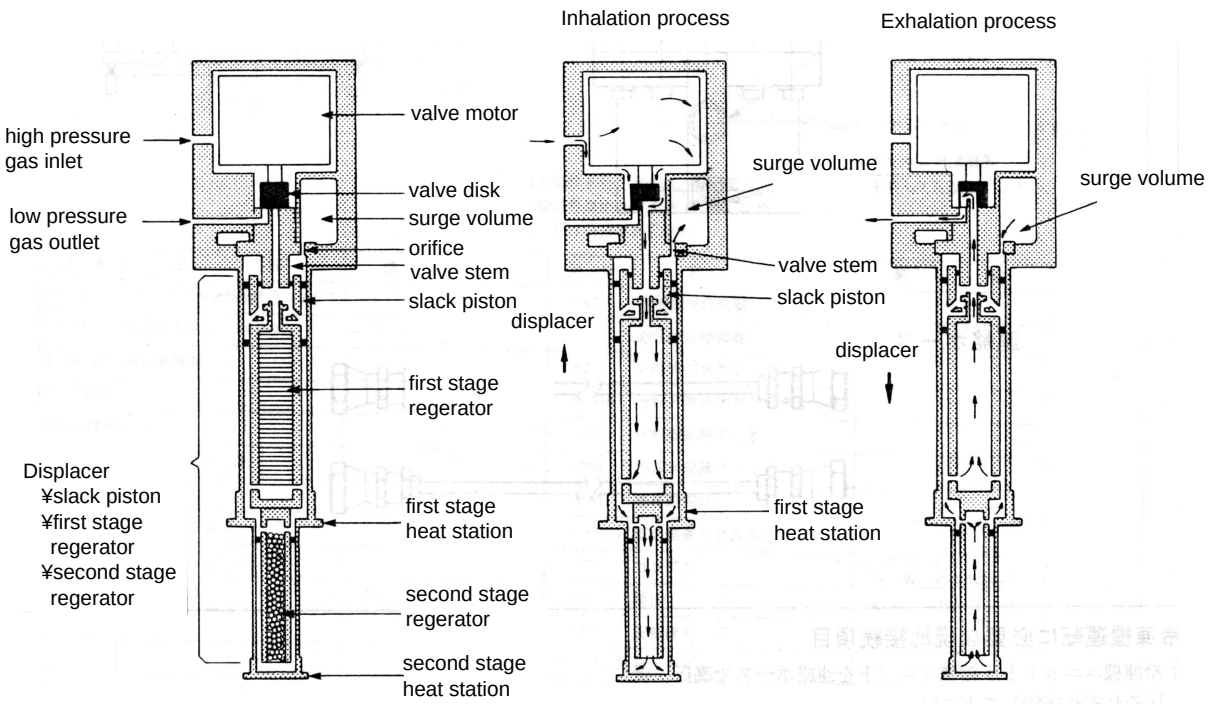

Figure 4.1: The cross-sectional view of GM refrigerator and working processes of it. [28]

Table 4.1: comparison between room temperature magnets and superconducting magnets using compact refrigerators

	power consumption	cooling water consumption
temperature solenoid coils (1.4 T mirror field)	140 kW	80 L/min
superconducting solenoid coils using compact refrigerators (3 T mirror field)	10 kW (used for refrigerators)	15 L/min used for refrigerators

solenoid coils and a permanent hexapole magnet. Furthermore, less thermal insulating supports are desirable to decrease heat invention. Such a limitation leads us to minimize the unbalanced electromagnetic force between coils and iron yokes in design of superconducting magnet system when using G-M type refrigerators (details are described in section 4.3 and 4.5) .

4.2 Design Features of the Source

A sketch of our ECR ion source is shown in Fig. 4.2.

The axial field is given by a set of four solenoid coils which are divided in three groups. The microwave injection side coils consist of two solenoid coils. The center one works in a reverse current to increase the mirror ratio. This superconducting coil system constructed at MITSUBISHI Electric Co., has the following characteristics:

- Internal diameter: 290 mm
- External diameter except center coil: 445 mm
- External diameter of center coil: 380 mm
- Width except inner coil of injection side: 80 mm
- Width of inner coil of injection side: 80 mm
- Conductor: NbTi/Cu
- Maximum current density: 100 A/mm^2
- Axial mirror to mirror distance: 400 m

The highest axial magnetic field profile is shown in Fig. 4.2. The microwave injection side coils generate a maximum field of 3 T, the beam extraction side coil generates a maximum field of 2 T.

Figure 4.3 shows the superconducting coil system and the cryostat. Two G-M refrigerators, a low power 20 K/80 K refrigerator and a high power 4.2 K/50 K refrigerator are placed in the vacuum chamber to refrigerate solenoid coils as shown in Fig. 4.3.

Each refrigerator have two heat station stages. The first stage of the 4.2K/50K refrigerator is used for thermal shield. The second stage of 4.2K/50K refrigerator cools solenoid coils via a heat conductor below 4.2 K. The 20K/80K refrigerator cools current leads and prevents a heat invasion to solenoid coils through current leads. The temperatures and cooling powers on each stage of two refrigerators are listed in Table 4.2.

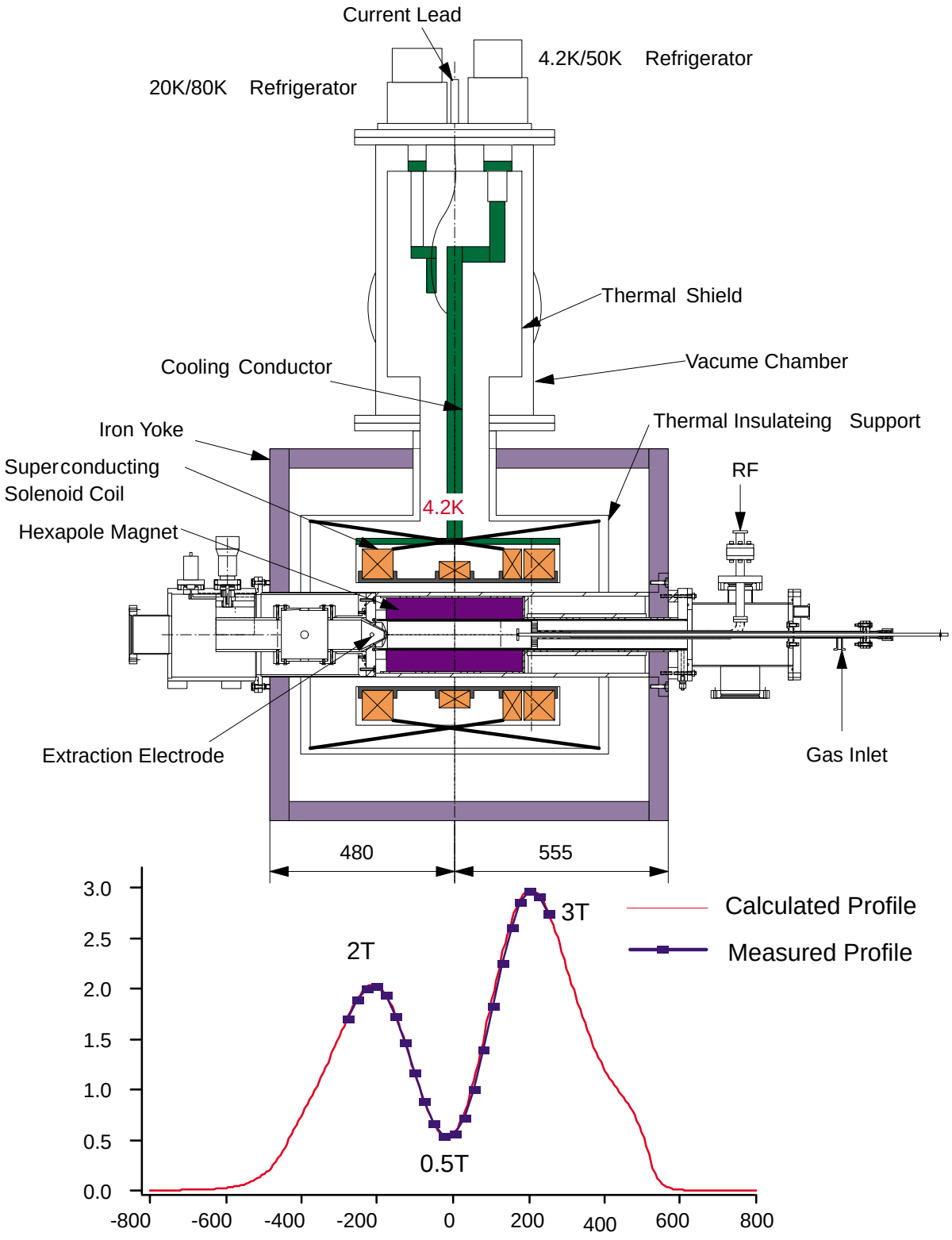

Figure 4.2: A schematic drawing of the ECR ion source using liquid-He-free superconducting solenoid coils and a mirror field profile generated by superconducting solenoid coils.

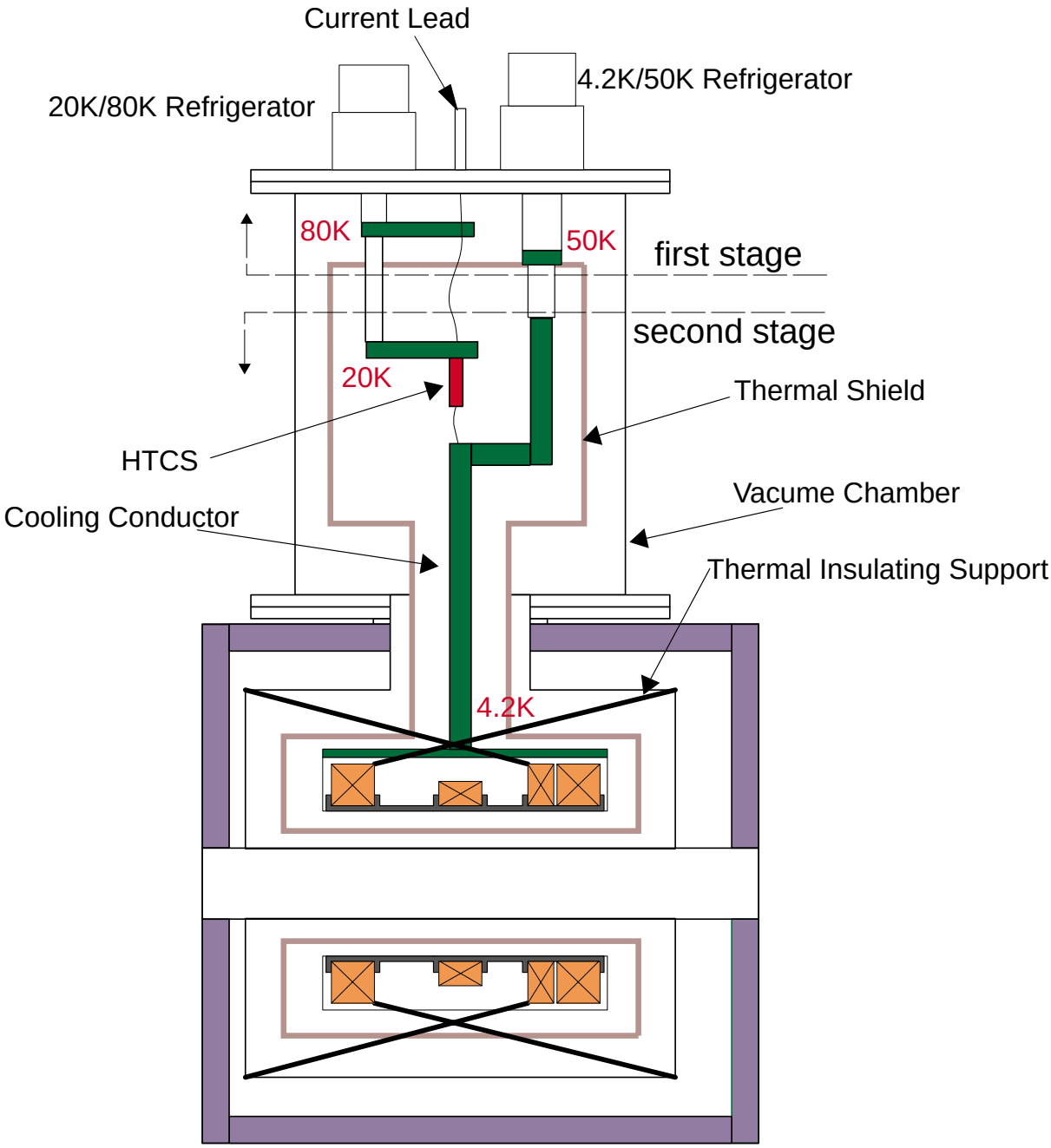

Figure 4.3: A schematic drawing of the superconducting coil system and the cryostat.

The hexapole magnet consists of 24 pieces of Nd-Fe-B permanent magnet, which is mounted in the cryostat bore whose diameter is 220 mm, at room temperature. The inside wall of the cryostat is electrically insulated form the plasma chamber and the hexapole magnet. The outer diameter and the inner diameter are 174 mm and 80 mm, respectively. This hexapole magnet gives a magnetic field of 1 T at the inside wall of the

Table 4.2: Temperatures and cooling power on each heat station

refrigerator	stage	temperature on the stage	cooling power
4.2K/50K refrigerator	first stage	50 K	35 W
	second stage	4.2 K	0.7 W
20K/80K refrigerator	first stage	80 K	40 W
	second stage	20 K	4 W

plasma chamber. The details about the design of hexapole magnet are described in section 4.4.

The inner diameter of the plasma chamber is 72.1 mm. The inner wall of plasma chamber is covered up with a thin aluminium cylinder of which thickness is 1 mm. The aluminium surface emits several secondary electrons per primary electron impact, which helps to increase the plasma density [29].

To protect the hexapole magnet from demagnetization by high temperature, the plasma chamber takes double wall structure to flow cooling water.

To evacuate the plasma chamber an the chamber of beam extraction system, two turbo molecular pumps are used. The turbo molecular pumps of 500 L/s are placed at beam extraction side and microwave injection side, respectively. A vacuum of $10^{-7} \sim 10^{-8}$ Torr can be expected with this vacuum system.

All feedthroughs for gas and RF are done along the axis, avoiding any radial opening. A single 14.5 GHz, 2 kW klystron supplies RF power to the source. The puller and the einzel lens are movable by external manipulation.

4.3 Unbalanced Electromagnetic Force between the Iron Yoke and the Solenoid Coils

When using small-power-refrigerators, it is necessary to minimize unbalanced electromagnetic force , due to the small cooling power (about 1 W at 4.2 K). Our conclusion in the design was that the unbalanced axial force should be less than 15 kN. To minimize the force, we searched the optimum arrangement of coils, the axial position of the yoke and operational conditions using code-OPERA [30].

For an example, usual magnetic configuration[31] with our iron yoke is shown in Fig. 4.4. In this configuration, the unbalanced electromagnetic force between coils and a iron yoke becomes larger than 30 kN when some coils quench. This configuration is not suited to our requirement.

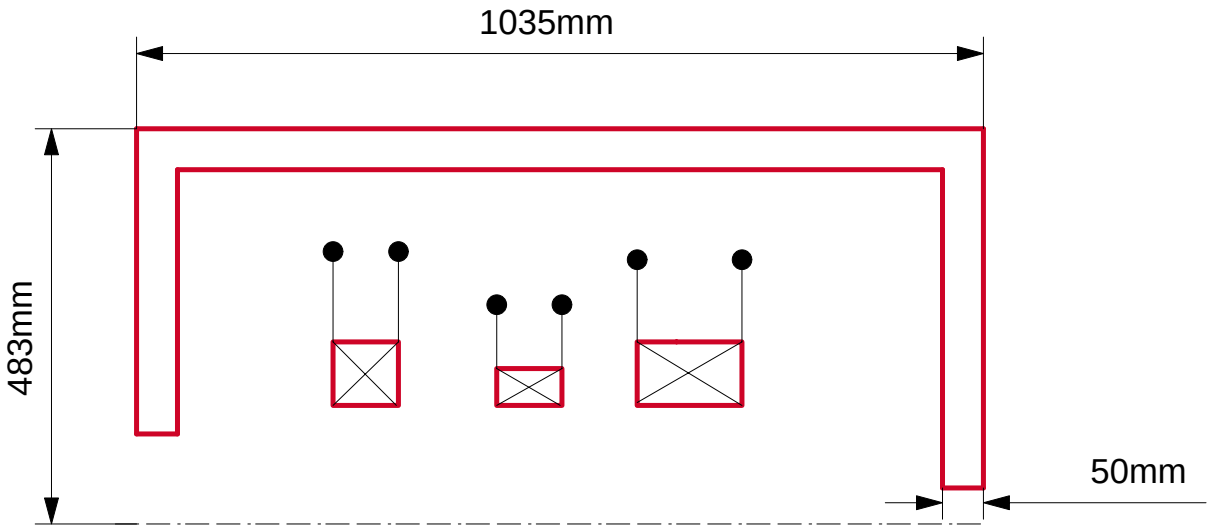

Figure 4.4: The magnetic configuration which is used for usual superconducting ECR ion source

To minimize the electromagnetic force, we have chosen the configuration of solenoid coils as show in Fig. 4.5. To reduce the electromagnetic force without expanding the iron yoke, the injection side coils consist of two solenoid coils (Coil III and Coil IV), and the outer coil of injection side (Coil IV) and the extraction side coil (Coil III) are connected in series.

The most hard conditions of the magnetic configuration when the electromagnetic force becomes maximum are as follows.

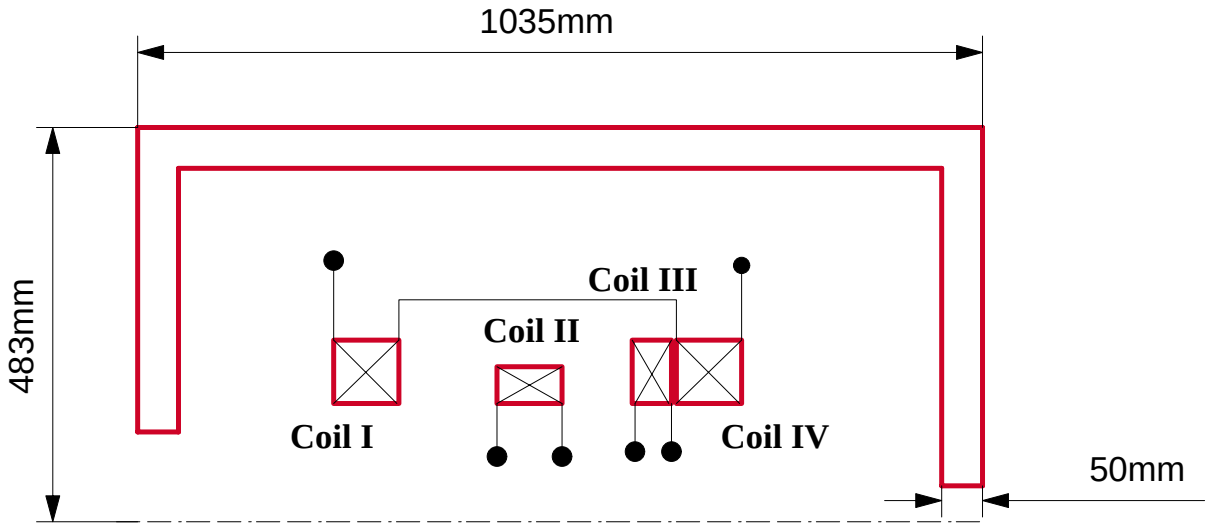

Figure 4.5: Our devised magnetic configuration. The injection side coils consist of two solenoid coils, and the outer one of the injection side coils and the extraction side coil are connected in series.

- case 1: When all coils except Coil III are quenched, the magnetic field of 3 T generated by induced current in Coil 3 will remain on injection side. The magnetic field profile of this case is shown as a solid line in Fig. 4.6. In this case, the electromagnetic force affecting coil toward injection side will become maximum. Since the position of the peak field will shift to inside, the electromagnetic force will reduce compared with a usual arrangement [31].

- case 2: When only Coil I and Coil II are not excited, the electromagnetic force affecting coil toward injection side will become maximum. The magnetic field profile of this case is shown as a dashed line in Fig. 4.6. Thanks to Coil III and Coil IV which are connected in series, there are peaks of a magnetic field at both sides always. This property contributes to reduce the electromagnetic force between the solenoid coils and the iron yoke.

As the optimized and calculated result, the electromagnetic stress become less than $\sim$ 15 KN , as shown in Fig. 4.6. The measured unbalanced force in case 2 is $\sim$13 kN. It is consistent with the calculated value. To summarize, it has been found that we can reduce the electromagnetic force between the iron yoke and the solenoid coils, and we have succeeded in

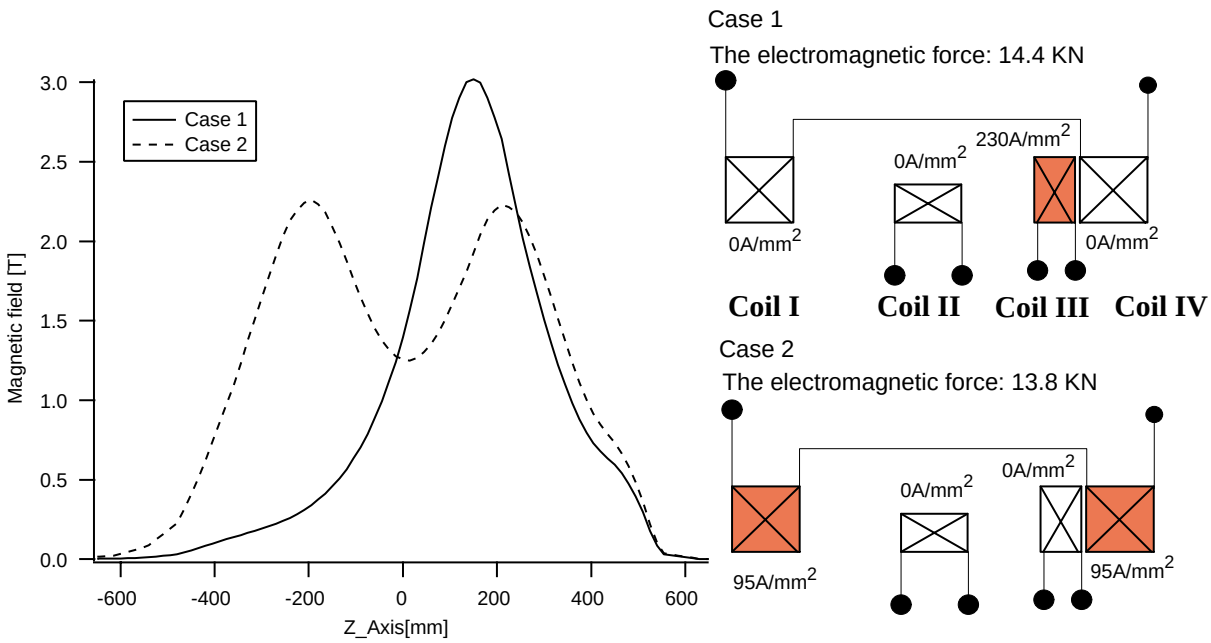

Figure 4.6: The magnetic field profile and the electromagnetic stress when the electromagnetic stress is maximum in this magnetic configuration

designing a compact magnetic system for an ECRIS.

4.4 Optimization of a Hexapole Magnet

For the ECRIS liquid Helium-free superconducting solenoid coils, we investigated optimization of the hexapole magnet with respect to the dependence of the magnetic field strength on the size of permanent magnet as well as the strength of permanent magnet and the number of magnet pieces in order to obtain best design of hexapole magnet. The code-Pandira [32] is used for computations of magnetic field.

Figure 4.7 shows the cross-sectional view of a typical hexapole magnet which consists of 24 pieces of permanent magnets and its magnetic field. As a typical demagnetization curve B(H) of a permanent magnet for the calculation of the magnet field, we adopted a straight line from the point (H=-130000 [Oe], B= 0 [Gauss]) to the other one (H= 0 [Oe], B= 130000 [Gauss]) as shown in Fig. 4.8.

The dependence of the magnetic flux density on the size of permanent magnet is shown in Fig. 4.9. The horizontal axis is a ratio of the external radius to internal one. The vertical axis is a magnetic flux density at the half point of the internal radius. Each line is the case when number of pieces is 24. The dashed line and the solid line indicate the cases when external radius is 4 cm and 2 cm respectively. As show in Fig. 4.9, when magnetic field made by magnets of various size is plotted as a function of the size normalized with internal radius, the magnetic field does not depend on the internal radius of the hexapole magnet. This indicates that magnetic field strength does not depend on absolute magnet size, but rather does on relative magnet size. The magnetic field strength increases with normalized radius up to $\sim$3.5 and then saturates almost. This behavior does not depend on the remanent magnetic flux density of permanent magnets, as shown in Fig. 4.10.

Figure 4.11 shows the magnetic flux density as a function of the number of pieces. In this calculation, we used the one with internal radius of 4 cm and external radius of 9 cm. The magnetic flux densities at the half point of internal radius are plotted. The magnetic flux density increases with the number of pieces as shown in Fig. 4.11. The saturation appears from 24 or

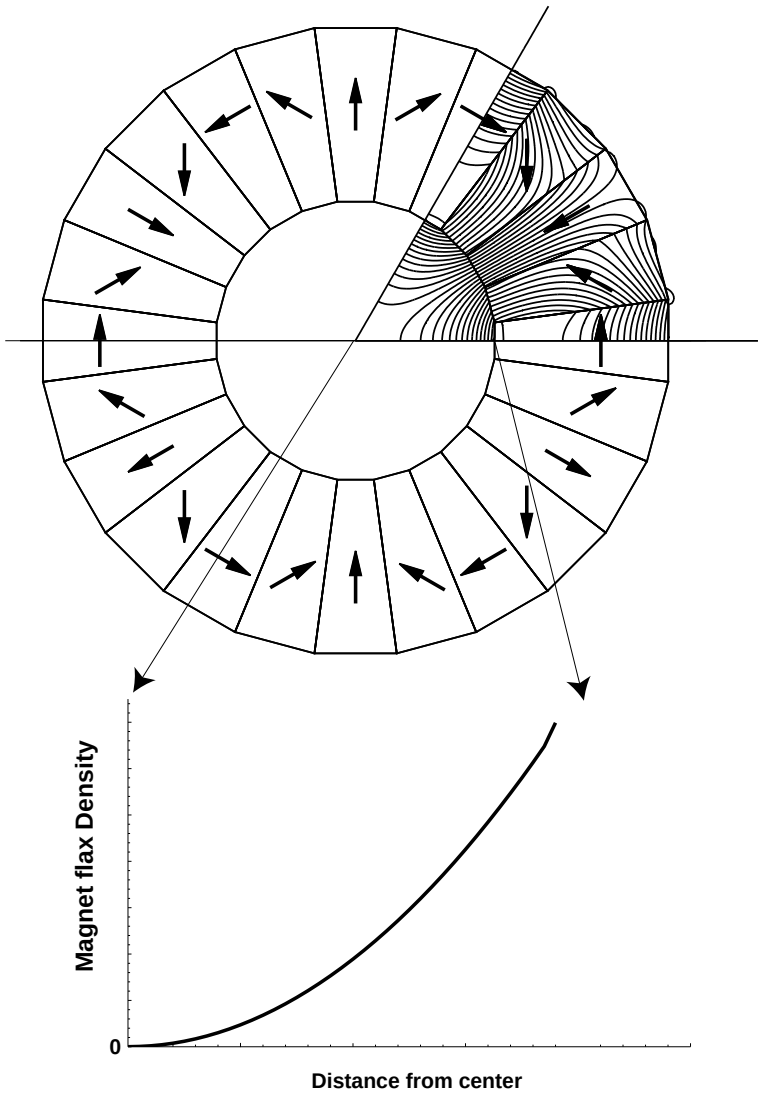

Figure 4.7: A typical Hexapole Magnet consists of 24 pieces and the Pandira computation of it. Arrows in permanent magnets indicate the directions of the magnetization.

30 pieces. From these calculations, we have chosen the hexapole magnet which consists of 24 pieces permanent magnet.

Figure 4.12 shows the demagnetic field in permanent magnet along direction of magnetization. The demagnetization curve for this computation is shown in Fig. 4.8. The demagnetic field in permanent magnet is over -14000 [Gauss] which is stronger than coercive forces of usual magnets. This result suggests that to obtain expected magnet field we must give higher priority to the permanent magnet which has a stronger coercive force rather than larger remanent magnetic flux density.

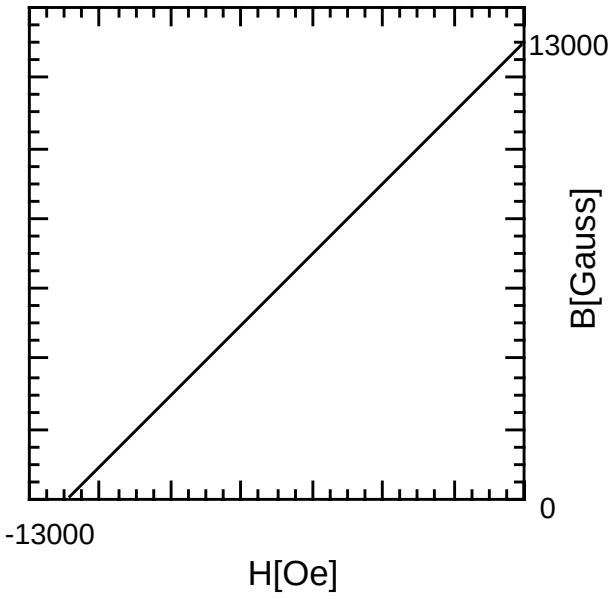

Figure 4.8: Demagnetization curve B(H) of a typical permanent magnet.

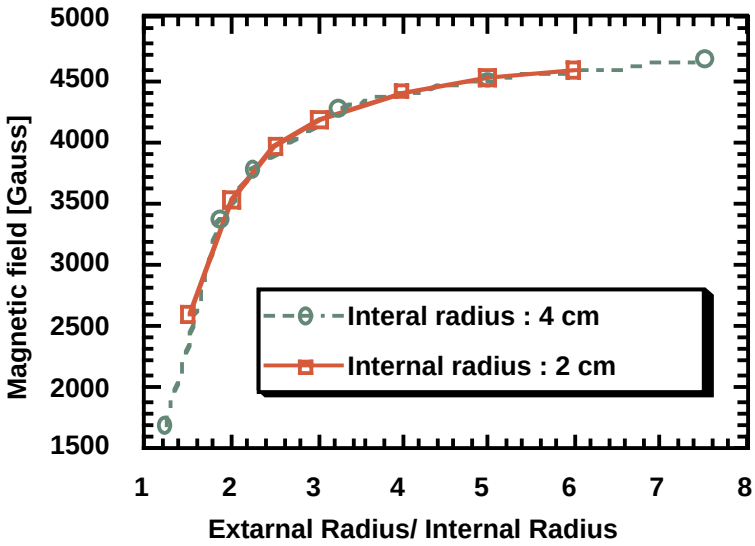

Figure 4.9: Dependence of the magnetic flux density on the size of hexapole magnet.

From the calculated results, the inner diameter and the outer diameter of the our designed hexapole are 80 mm and 174 mm, respectively. The ratio of external radius to internal radius is 2.18. The number of pieces is 24 as shown in Fig. 4.13. To obtain the expected magnetic field from the calculated results, we adopt the N38H Nd-Fe-B permanent magnet of company ShinEtsu, which have strong coerchive force as a commercial product. The characteristics of the hexapole magnet are as follows.

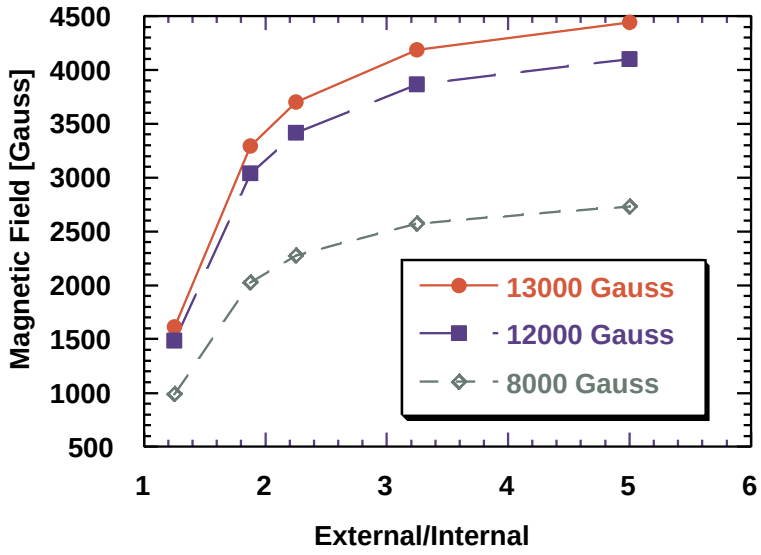

Figure 4.10: Dependence of the magnetic flux density on the size of hexapole about various remanent magnetic flux density of permanent magnets. The magnetic flux density at the half point of internal radius is plotted.

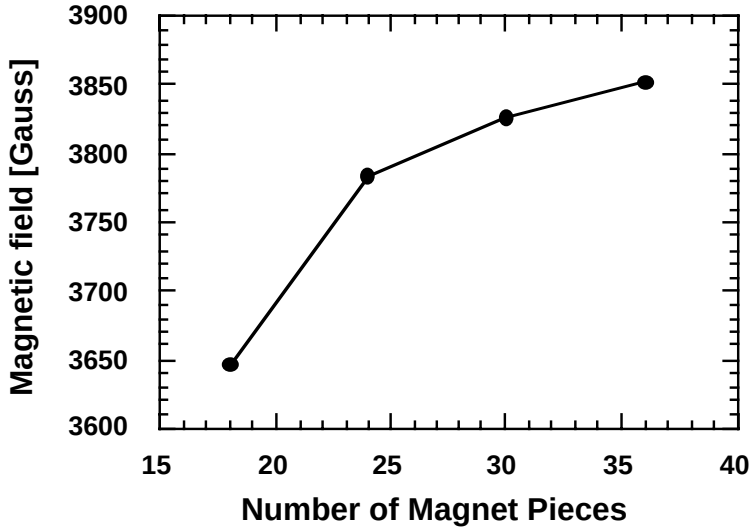

Figure 4.11: The magnetic filed strength as a function of the number of magnet pieces.

- remanent magnetic flux density Br: 12400 $\sim$ 13000 G
- coerchive force iHc: 17000 $\sim$ Oe
- coerchive force iHb: 11400 $\sim$ 124000 Oe

The calculated results of magnetic field on inner wall of plasma chamber was 1.1 T as shown in Fig. 4.13. Figure 4.14 shows the comparison between

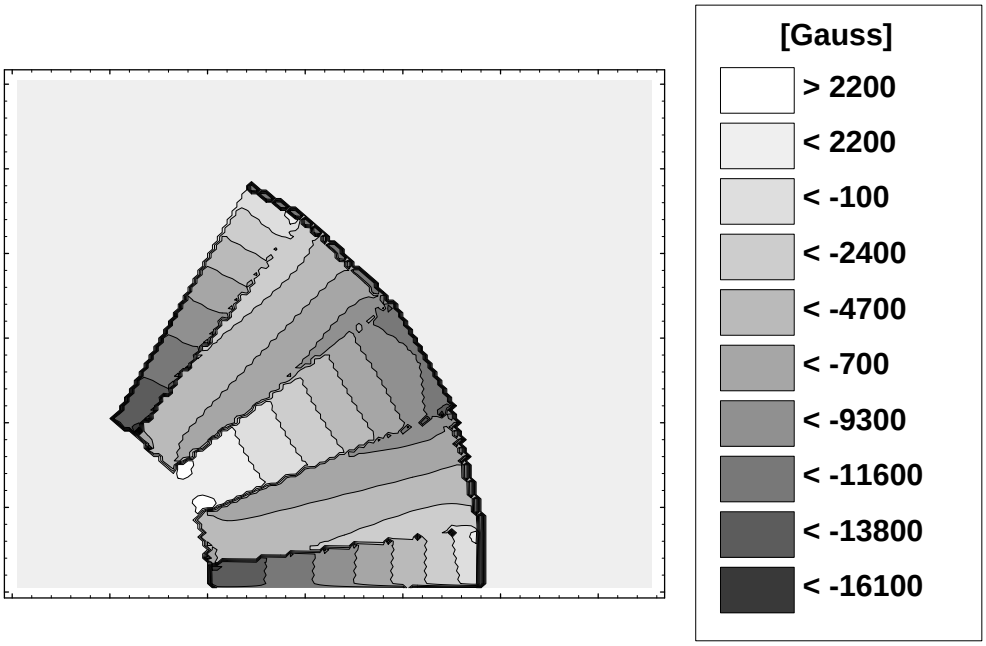

Figure 4.12: Demagnetic flux density in permanent magnets along direction of magnetization.

the measured magnetic field and the calculated magnetic field by code-Pandira on ϕ 70.7. The fluctuation of peak magnetic fields is less than 5 %. The measured magnetic field strength is about 10 % smaller than the calculated field. Then the strength of magnetic field on inner wall of plasma chamber is 1 T. It may cause the overestimation of calculated result that code-Pandira can not evaluate the curvature of a demagnetization curve.

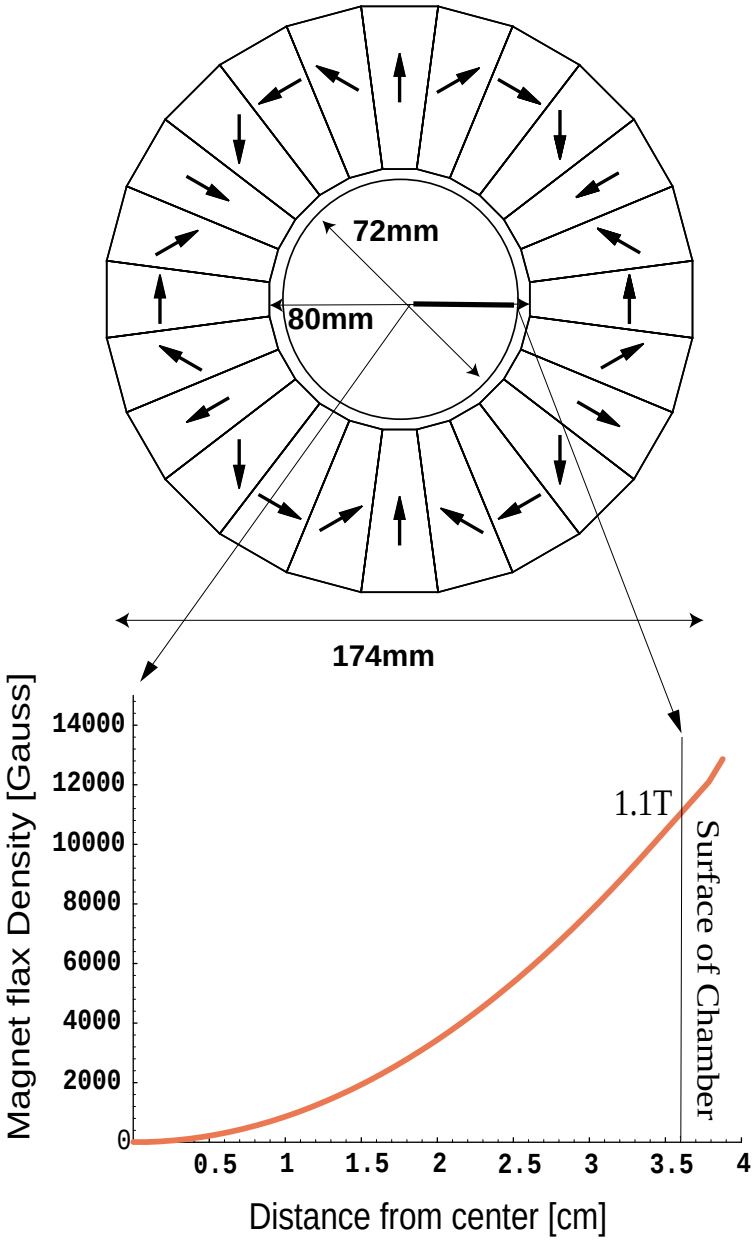

Figure 4.13: The optimized hexapole magnet configuration and it's calculated results of magnetic field.

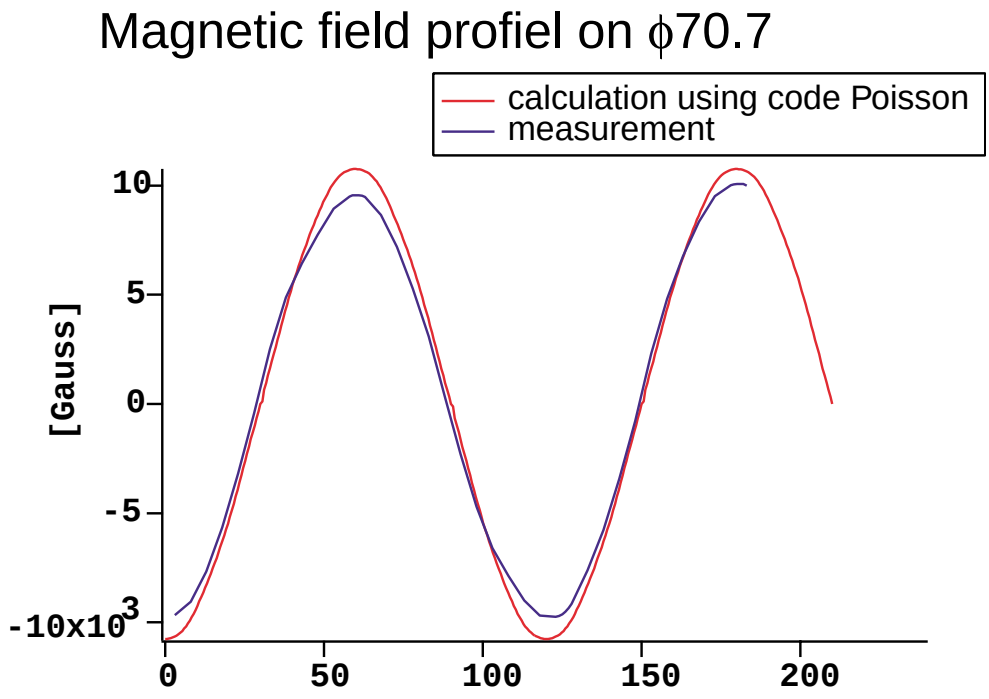

Figure 4.14: Comparison between calculated magnetic field and measured magnetic field.

4.5 The Electromagnetic Stress between the Solenoid Coils and the Hexapole Magnet

In principle, if the position of center axis of a hexapole magnet is completely same as the center axis of solenoid coils, the electromagnetic force between solenoid coil and hexapole magnet will not be generated. But actually the both center axis will not be on same position due to errors of manufacture. In this case, strong force between a hexapole magnet and solenoid coils may be generated. For estimating this effect, we calculate a magnetic field and force between a hexapole magnet and solenoid coils, using the computation program Opera-3D [30].

For easy calculation, a permanent hexapole magnet is replaced with a hexapole coil. Figure 4.15 shows the magnetic profile of the permanent hexapole magnet and the hexapole coil. The inner magnetic field profile of the permanent hexapole magnet can be represented by the hexapole coil. But the outer magnetic profile of the hexapole coil is stronger than one of the permanent hexapole magnet. It means that the electromagnetic force between the hexapole magnet and the solenoid coils will be overestimated. In a sense of safety, it is allowed that the permanent hexapole magnet is replaced with the hexapole coil.

Figure 4.16 show the calculation model for the analysis of the stress between the hexapole magnet and the solenoid coils. The electromagnetic stress was calculated in the cases when the center of the hexapole coil and the solenoid coils were shifted 2 cm to X direction and Y direction with the maximum axial magnetic field. As a result, the stress is less than 100 N in any case. It can be concluded that force between the solenoid coils and the hexapole magnet is negligible small compared to other forces.

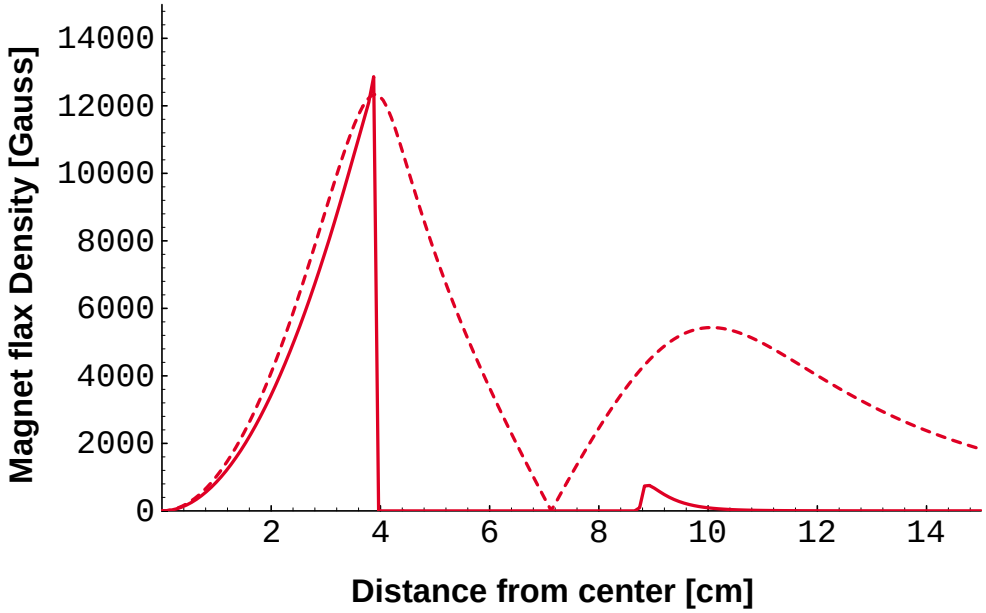

Figure 4.15: The magnetic field profile of the permanent hexapole magnet(solid line) and the hexapole coil(dashed line).

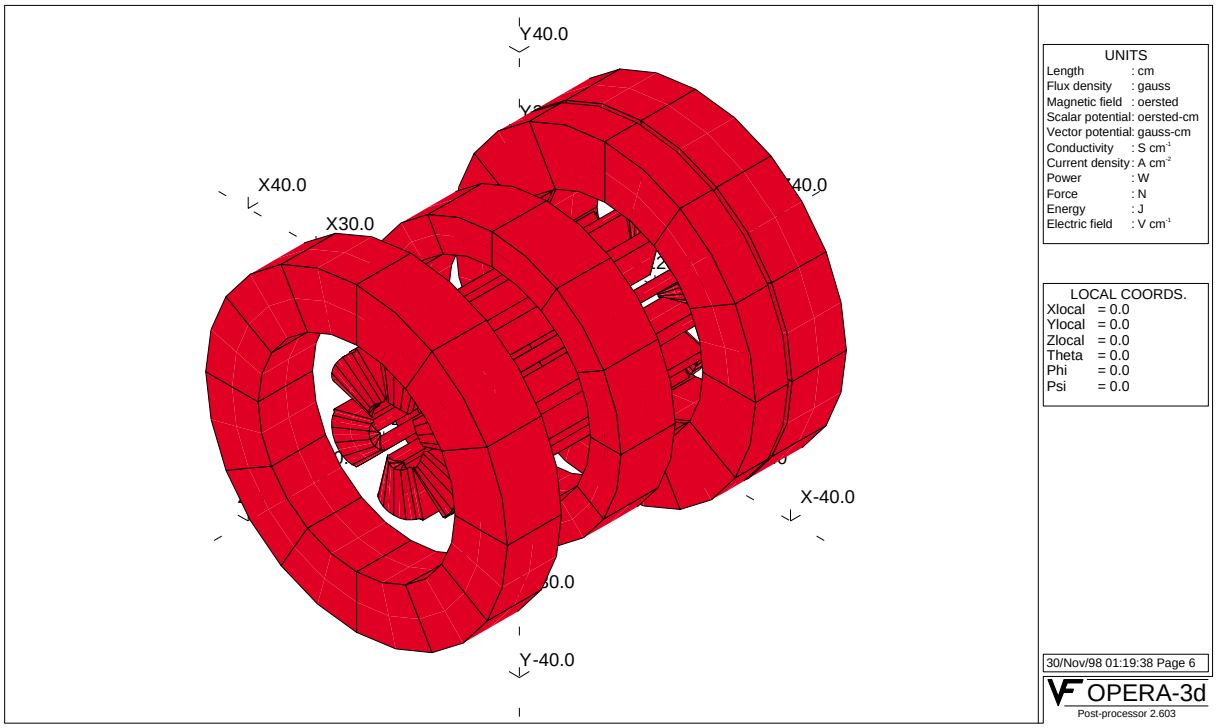

Figure 4.16: A 3D view of calculation model for the stress analysis.

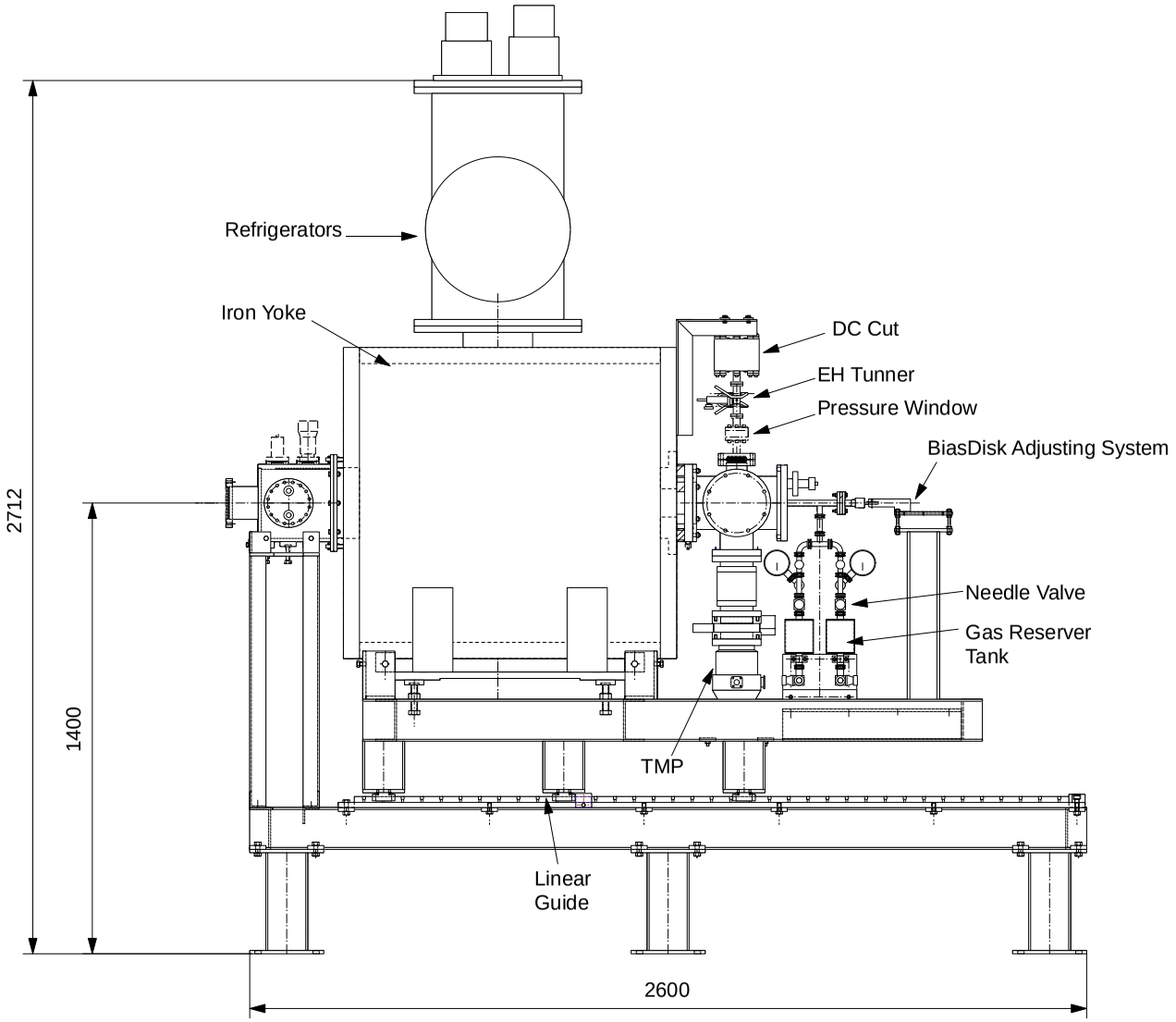

Figure 4.17: A side exterior of the liquid-He-free superconducting ECR ion source

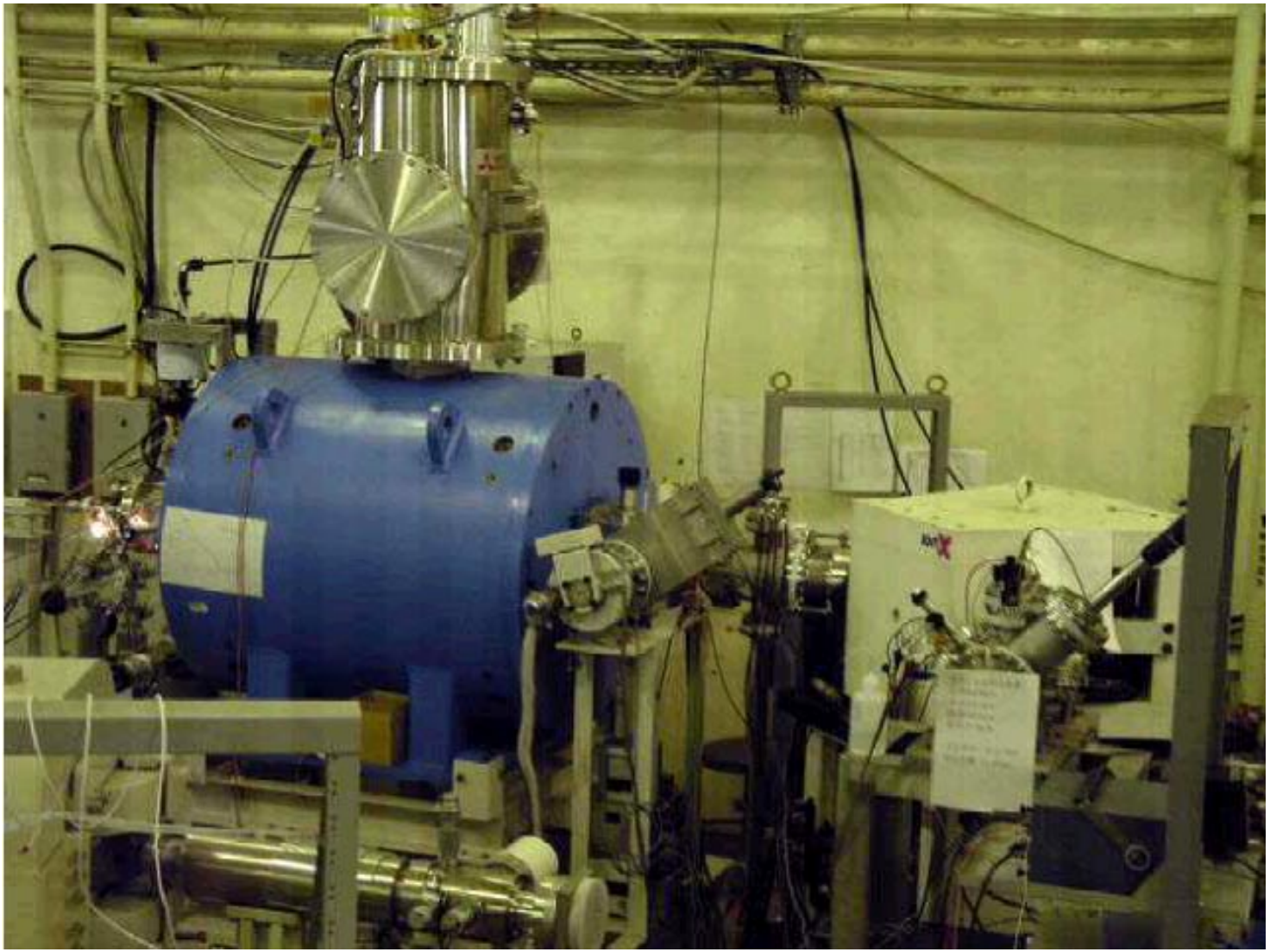

Figure 4.18: A photograph of the liquid-He-free superconducting ECR ion source and the beam line

Chapter 5

Experiments

5.1 Experimental Setup and Conditions

The developed new ECRIS is named SHIVA (**S**uperconducting without liquid **H**e ECR **I**on source for **V**arious **A**tomic cluster experiments). To measure the beam intensities extracted from SHIVA, we constructed a simple experimental system which consist of a bending magnet, electrostatic steerers, two einzel lenses and a Faraday cup (Fig. 5.1).

The ions from SHIVA were accelerated by potential difference $\sim$ 20 kV (15 kV typically used) between the plasma electrode and the extraction electrode. The distance between the plasma electrode and the extraction electrode could be changed between 15 mm $\sim$ 70 mm. The extraction hole was 10mm. The extracted ion beam were injected into the entrance of bending magnet through an electrostatic steerer and two einzel lenses, which were placed between the ion extraction region and the bending magnet as shown in Fig. 5.1. And the ion beams were analyzed by the 90 degrees bending magnet. Main parameters of the bending magnet are listed in Table 5.1. One more electrostatic steerer was placed just behind the bending magnet.

The beam intensities were measured by the Faraday cup placed near the focusing point of the bending magnet. For suppressing the secondary electrons emitted from the Faraday cup, a negatively biased electrode ring was placed in the front of it. At the focusing point of the bending magnet, a set of movable slits are placed, of which opening could be changed from 0 mm to 25 mm.

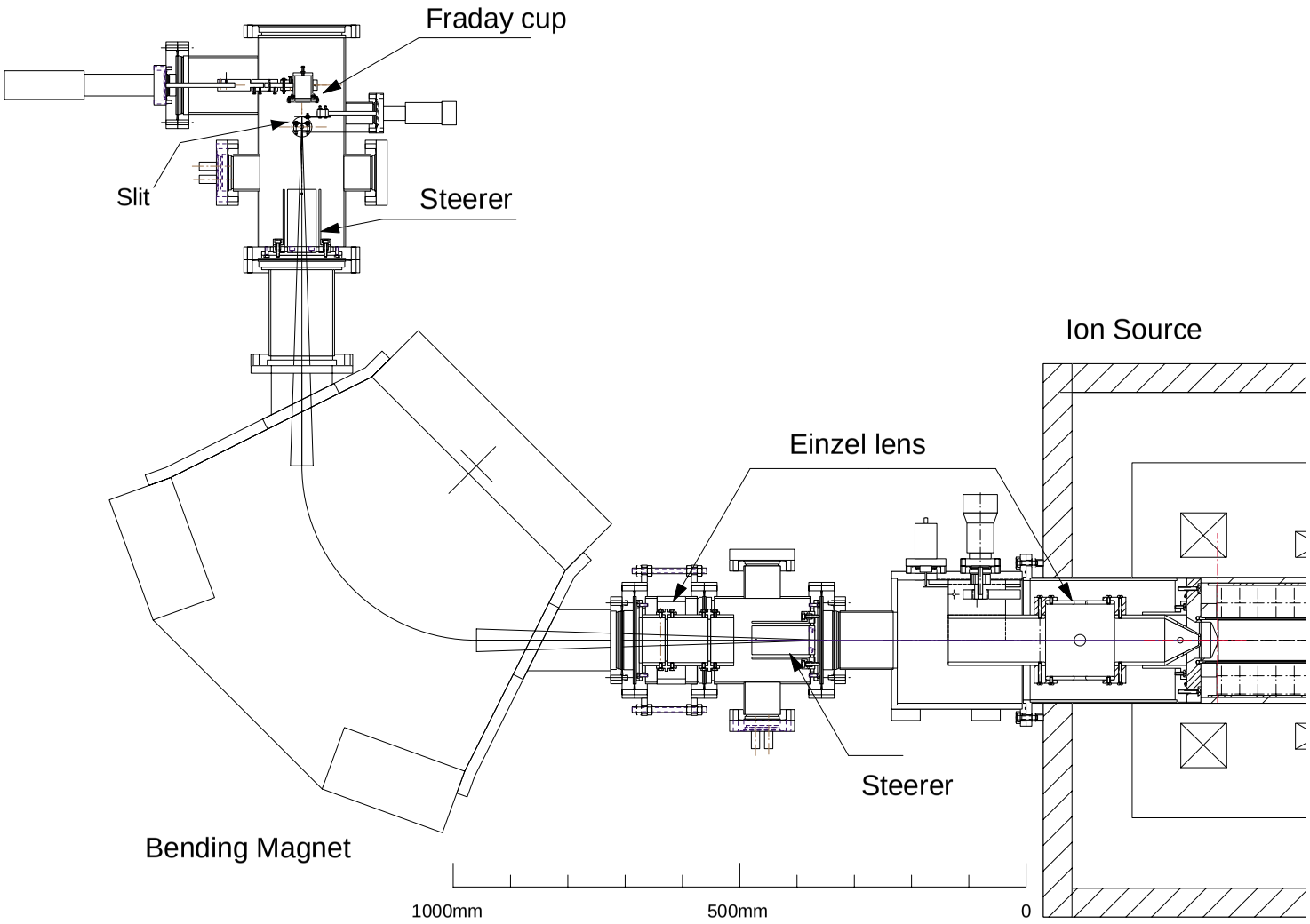

Figure 5.1: The Experimental Setup

Table 5.1: Characteristics of the bending magnet

Angle	90 degrees
Radius	12 inch
Air gap	1.558 inch
Maximum field strength	11700 Gauss
Focal length	24 inch

The gases were fed into the plasma chamber from microwave injection side and its flows were controlled by needle valves. For production of Xe ions, we used an enriched ^{136}Xe gas (enrichment of 85%). For all elements heavier than carbon, usually gas mixing method[19] is used to obtain the highly charged heavy ions. We used oxygen gas as a mixing gas to produce highly charged xenon ions.

The base pressure of the plasma chamber without gas feeding was about 1×10^{-7} Torr.

As show in Fig. 5.2, a thin aluminium cylinder covered inner wall of plasma chamber. The aluminium cylinder can helps to increase the plasma density with secondary electrons emitted from its surface [29]. A movable biased electrode made of stainless steel was inserted from microwave injection side as shown in Fig. 5.2. Variable range of the biased electrode is 130 mm from the end of the plasma chamber where is at B_{max} (maximum magnetic field strength of microwave injection side). The diameter and the thickness of the electrode were 30 and 5 mm, respectively.

A typical magnetic mirror field configuration used in these experiments is shown in Fig. 5.3. These experiments were not performed at the full capability of the coil system in order to keep a safety margin with respect to quench occurrence, and to allow scans of the axial magnetic field. The magnetic field strength of the injection side (B_{inj}) and the one of center (B_{min}) were fixed as $\sim$1.85 T and $\sim$0.4 T, respectively. The magnetic field strength of the extraction side (B_{ext}) was varied to study its influence on beam currents.

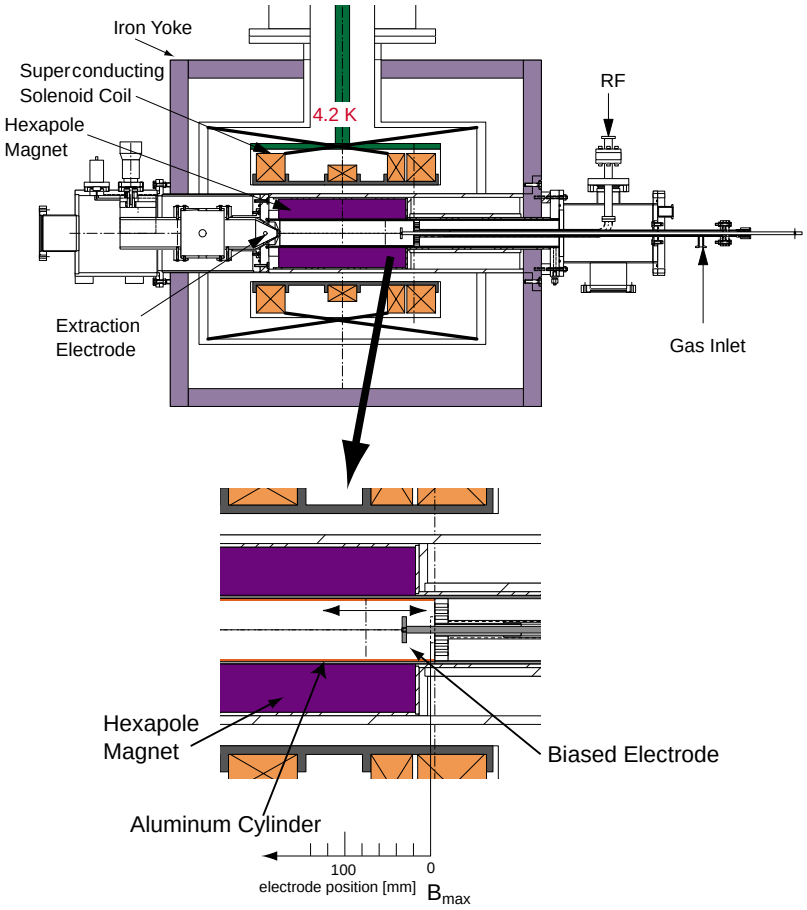

Figure 5.2: A cross-sectional view of plasma chamber with the aluminum cylinder and the biased electrode

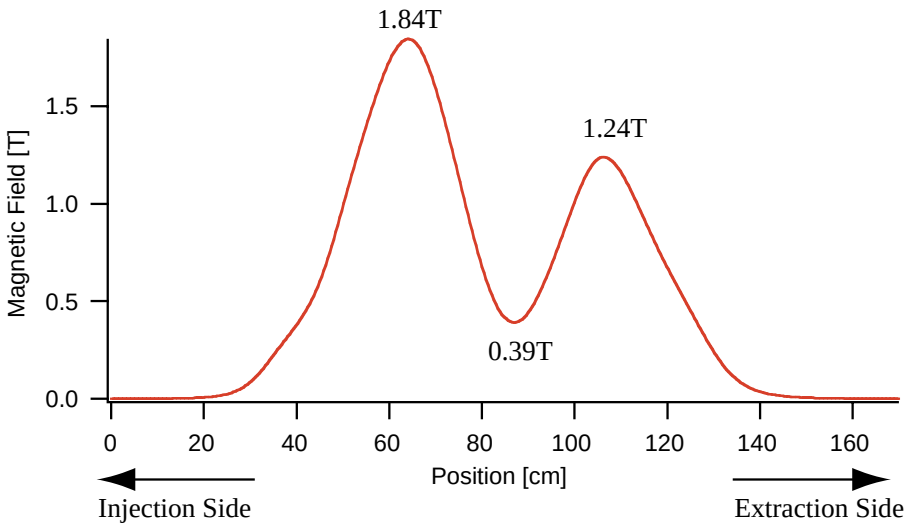

Figure 5.3: A typical mirror magnetic field used in this experiments.

5.2 Experimental Results and Discussion

5.2.1 Performance and Spectra

Figure 5.4 shows a typical charge state distribution of highly charged Xe ions for SHIVA, when the ion source was tuned for producing Xe^{32+} ions. The main parameters for producing Xe^{32+} are also listed in Fig. 5.4. Under these conditions, we obtained 9.6 μA of Xe^{30+}, 5.7 μA of Xe^{32+} and 0.9 μA of Xe^{36+} with 760 W of RF power.

The best results for so far are listed in Table 5.2. The main parameters for producing these ions are listed in the table. All ions were extracted at 15 kV.

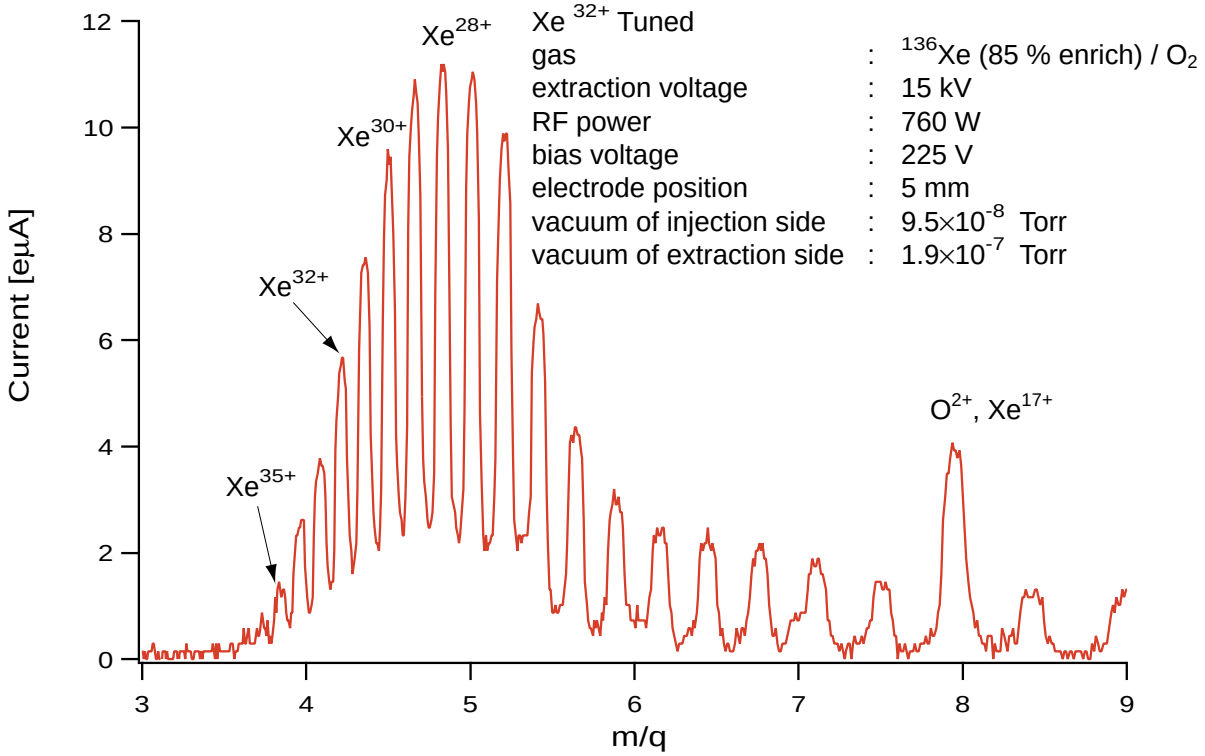

Figure 5.4: The charge stage distribution for Xe, optimized for Xe^{32+}

Table 5.2: Maximum currents of Xe ions extracted from SHIVA. B_{inj} and B_{min} were 1.85 T and 0.4 T, respectively.

charge state	current [eμA]	RF Power [W]	vacuum of extraction side [Torr]	vacuum of injection side [Torr]	B_{ext} [T]	bias voltage [-V]	electrode position [mm]
20	56.5	522	4.4×10^{-7}	1.3×10^{-6}	1.17	490	19.5
24	39.7	525	2.1×10^{-7}	5.4×10^{-7}	1.17	560	4.5
27	32.7	686	1.7×10^{-7}	2.2×10^{-7}	1	300	19.5
28	21.8	686	1.7×10^{-7}	2.2×10^{-7}	1	300	19.5
29	16.3	652	1.9×10^{-7}	2×10^{-7}	1	300	17.5
30	9.6	760	9.4×10^{-8}	1.9×10^{-7}	1.24	225	5
31	7.6	760	9.4×10^{-8}	1.9×10^{-7}	1.24	225	5
32	5.7	760	9.4×10^{-8}	1.9×10^{-7}	1.24	225	5
33	3.8	760	9.4×10^{-8}	1.9×10^{-7}	1.24	225	5
34	2.6	760	9.4×10^{-8}	1.9×10^{-7}	1.24	225	5
35	1.4	976	1.1×10^{-7}	1.8×10^{-7}	1.24	180	5
36	0.9	760	9.4×10^{-8}	1.9×10^{-7}	1.24	225	5
37	0.48	976	1.1×10^{-7}	1.8×10^{-7}	1.24	180	5

5.2.2 RF power Dependence

Figure 5.5 shows the RF power dependences of various highly charged Xe ions. After the ion source was tuned for producing these ions with a reasonably high injected RF power, the intensity of the currents were measured with respect to the RF power. The main parameters for producing each beam of ions are listed in Table 5.3

Table 5.3: Main parameters for Xe ions shown in Fig. 5.5

ion	RF Power [W]	vacuum of extraction side [Torr]	vacuum of injection side [Torr]	bias voltage [-V]	electrode position [mm]	B_{inj} [T]	B_{min} [T]	B_{ext} [T]
Xe^{20+}	716	4.4×10^{-7}	1.6×10^{-6}	350	1	1.91	0.4	1.09
Xe^{30+}	591	1.2×10^{-7}	2.1×10^{-7}	330	8	2.09	0.4	1.37
Xe^{32+}	515	9.2×10^{-8}	2.0×10^{-7}	560	21	1.85	0.4	1.18

As shown in Fig. 5.5, to produce higher charge state ions (e.g., 32+), we needed a higher RF power than that for producing lower charge state (e.g., 20+). It is clearly seen that the beam intensities of Xe ions are not saturated at the maximum RF power (about 800 W) injected in our experiments. We may obtain higher beam intensities at higher RF powers. However, we must keep a reflected RF power under 200 W, due to a limitation of the circulator (maximum absorption RF power of 200 W) mounted in the klystron power amplifier. When we tuned the ion source at a RF power higher than 800 W for producing Xe ions, the reflected RF power sometimes exceeded 200 W. Therefore, we could not safely increase the injected RF power over 800 W.

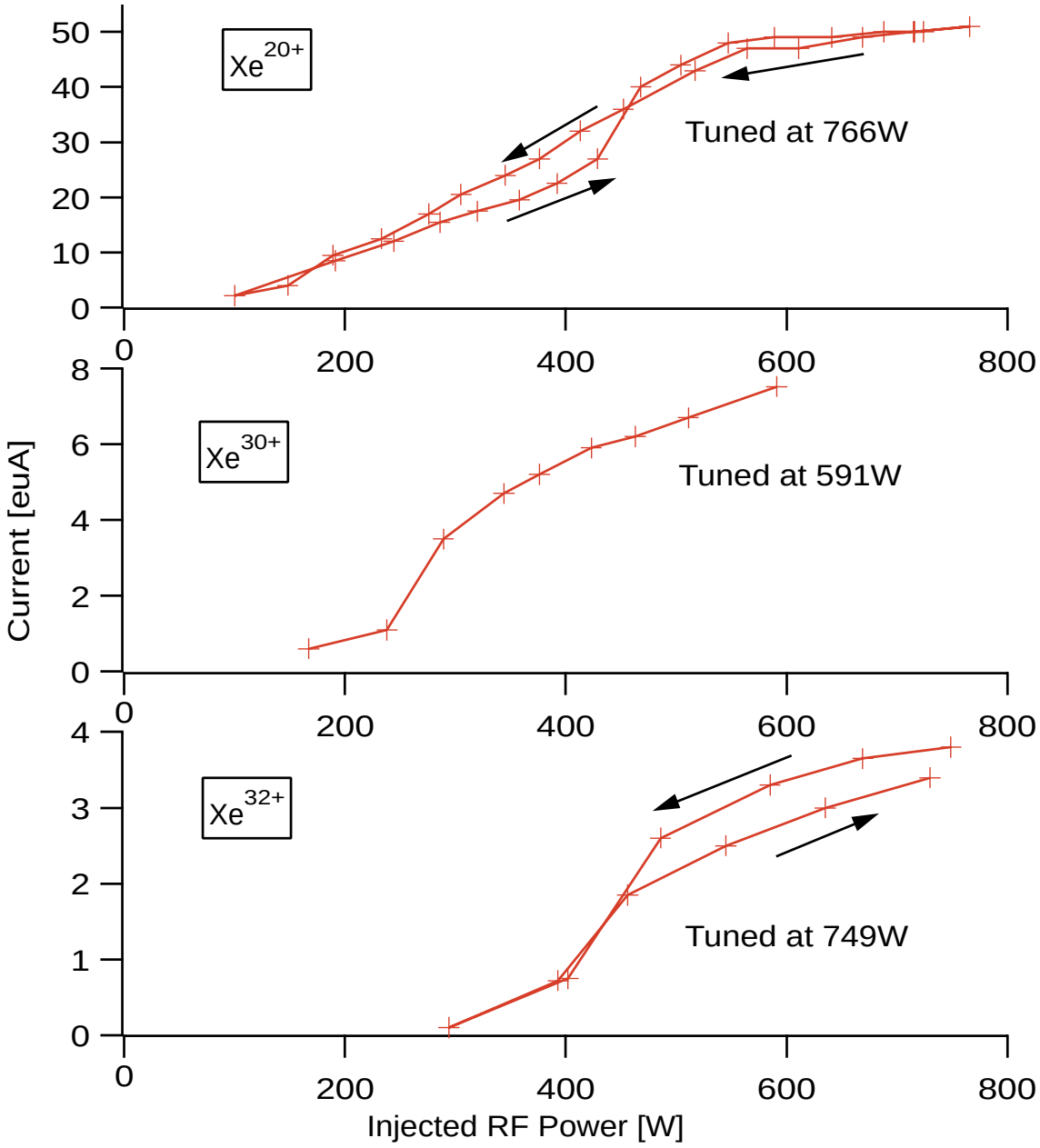

Figure 5.5: The injected RF power dependences of various highly charged Xe ions

5.2.3 Mirror Magnetic Field Dependence

As described in section 2.2, the strength of the mirror field critically influence the density of the plasma. Recently, it have been reported that the beam intensity of highly charged heavy ions increases with B_{inj} and almost saturates above the value of $3B_{ECR}$ to $4B_{ECR}$ [33, 34]. However, the influence of B_{ext} is still unclear. To investigate the influence of B_{ext} on the beam intensities and the charge state distributions, we measured the intensities and the distributions for three kinds of magnetic field configurations shown in Fig. 5.6. In this experiment, B_{inj} and B_{min} were fixed at approximately 1.85 T and 0.4 T, respectively. The gas pressure and the RF power were tuned to maximize the beam intensity of highly charged Xe ions for each configuration.

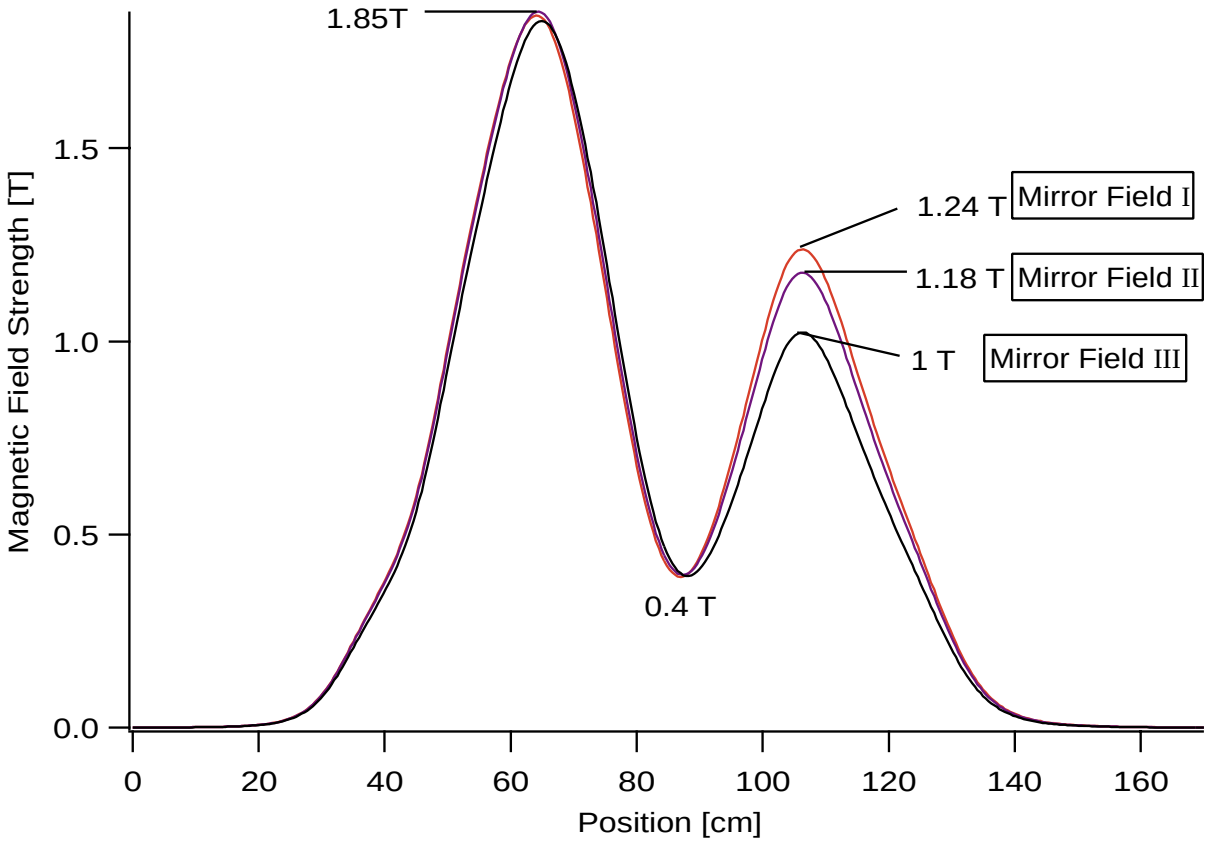

Figure 5.6: The mirror magnetic field profiles.

The spectra of Xe ions with Mirror Field I (extraction side 1.24 T) and Mirror Field III (extraction side 1 T) are shown in Fig. 5.7. The

operational parameters (gas mixing ratio, gas pressure and RF power, bias voltage) were optimized to produce Xe^{30+} ions, some of which are listed in Fig. 5.7.

Although we obtained the same beam intensity of Xe^{30+} under both conditions, the charge state distributions are significantly different. Comparing the two spectra, the high B_{ext} (Mirror Field I) gives higher intensities for the higher charge states of the Xe ions but lower intensities for the lower charge states of the Xe ions. On the other hand, the low B_{ext} (Mirror Field III) gives higher intensities for the lower charge states of Xe ions. Furthermore, the mean charge state is shifted from 26+ to 28+ with increasing B_{ext} as shown in Fig. 5.8. This means that the ion confinement time may increase with the B_{ext}.

Figure 5.9 shows the best results for Xe ions for each magnetic configuration.

It is clearly seen that Mirror Field III is suitable for producing lower charge states of Xe ions. From these experimental results, we find that the magnetic field strength of the extraction side is important for maximizing the beam intensity of Xe ions, i.e., for producing lower-charge-state Xe ions (e.g., 25+), it is better to decrease B_{ext}. On the other hand, for producing higher-charge-state Xe ions (e.g., 32+), B_{ext} must be increased.

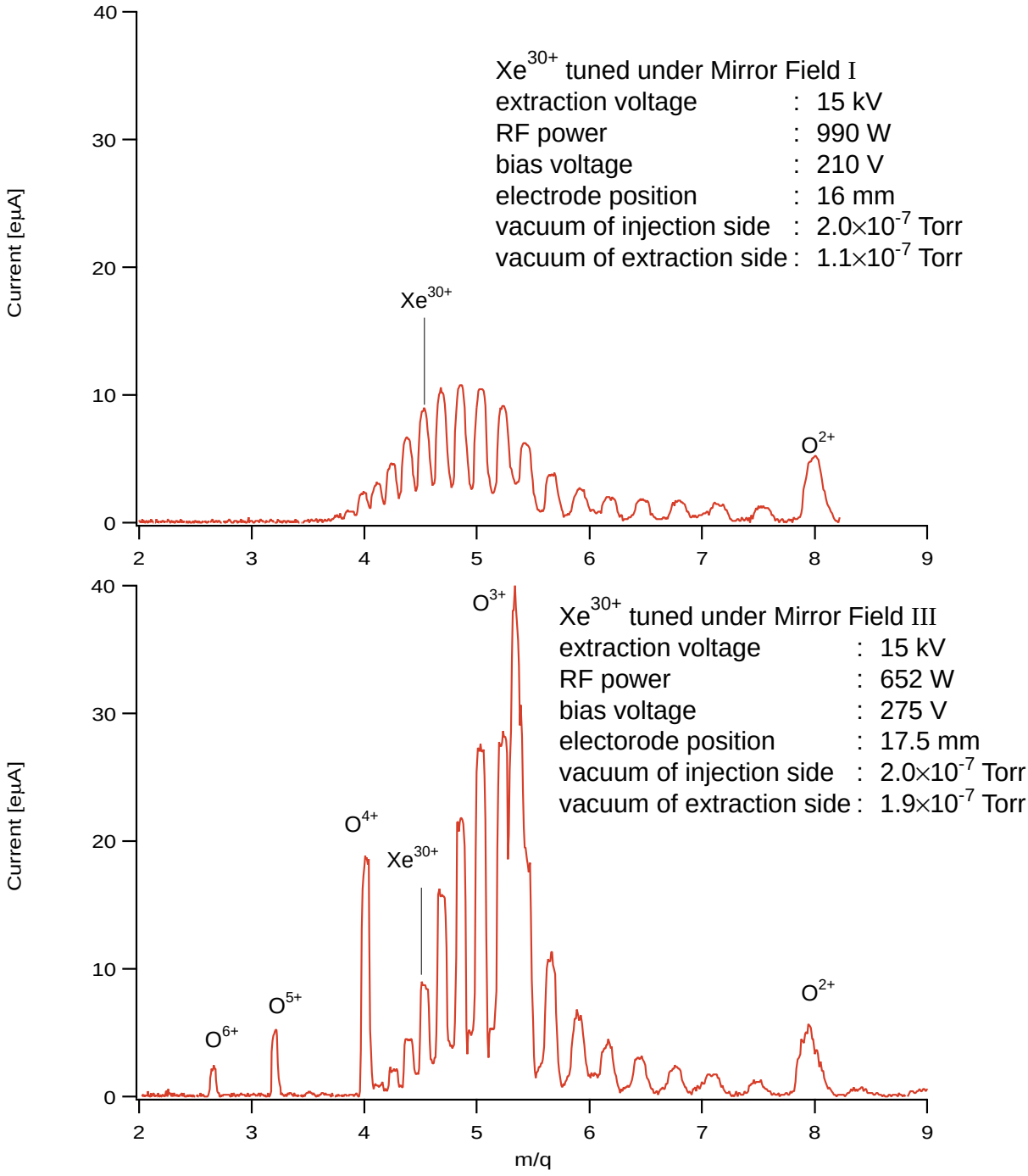

Figure 5.7: The spectra of Xe ions optimized for Xe^{30+}.

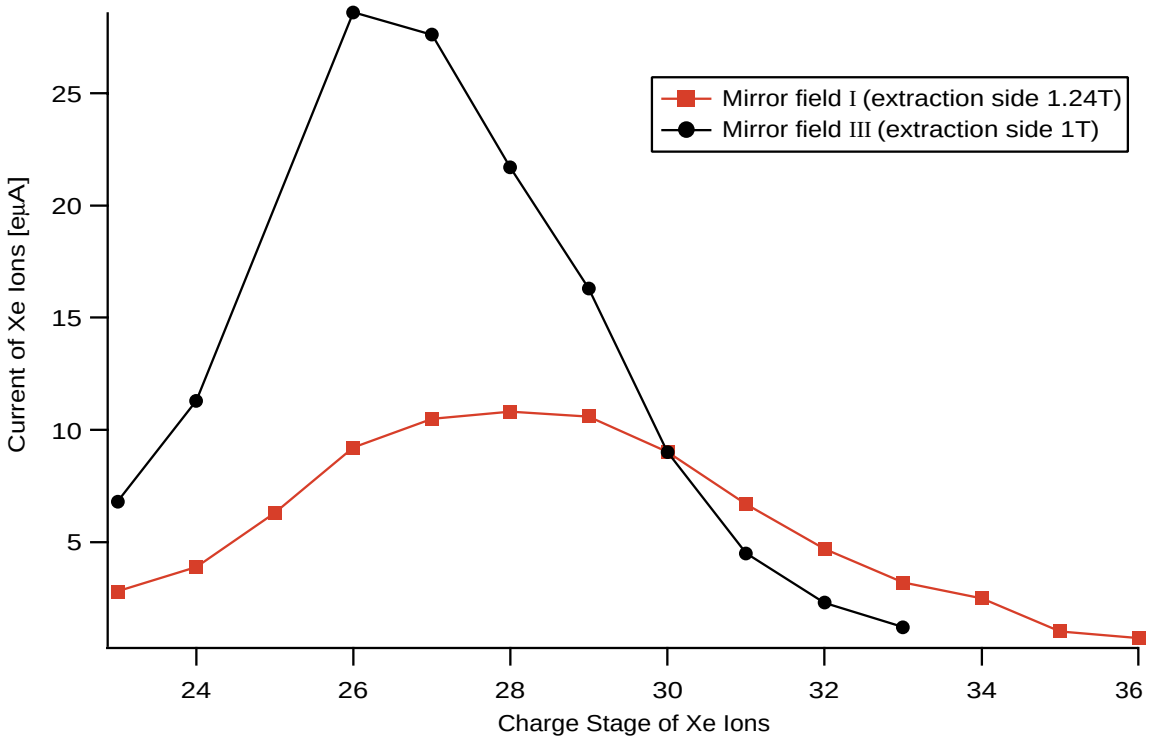

Figure 5.8: The charge state distributions of Xe ions optimized for Xe^{30+}.

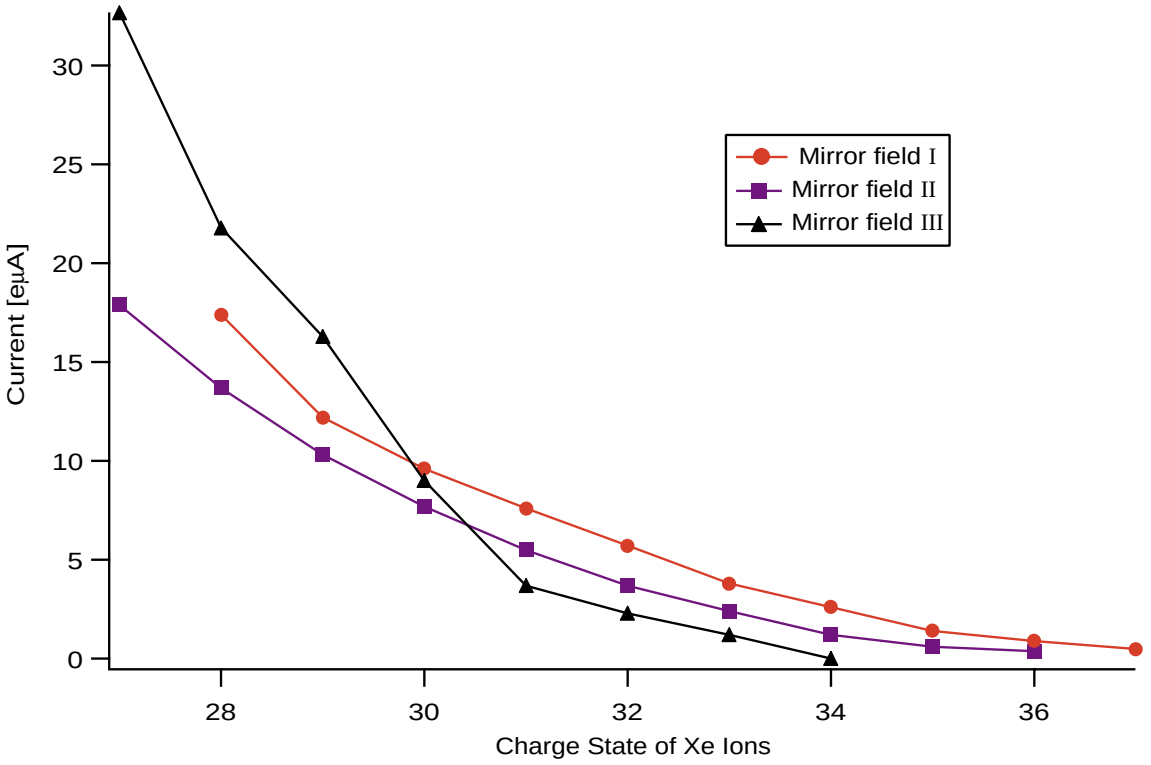

Figure 5.9: The best results for Xe ions in Mirror Field I, II and III

5.2.4 Biased Electrode Effects

We observed that a floating potential electrode helps to increase the beam intensities produced from the RIKEN 18 GHz ECRIS as described in chapter 3. In the case of SHIVA, a negatively biased electrode is very helpful in extracting intense ion beams, as observed in some other ECRISs (see chapter 3). In this section, I describe the effects of the negatively biased electrode on the beam intensities.

The beam intensities are strongly dependent on the position of the electrode, as shown in Fig. 5.10. The parameters for this measurements are listed in Table 5.4. It seems that the beam intensity oscillates regularly, and the distance between two peaks is about 10 mm. This corresponds to almost half the wavelength of the 14.5 GHz microwaves. The plasma chamber may behave as a multimode cavity, and the electrode crosses the standing waves when the electrode moves axially. Therefore, the matching conditions between the plasma and the microwaves may vary with axial motion of the biased electrode.

Table 5.4: The parameters of the measurement in Fig. 5.10

RF Power [W]	vacuum of extraction side [Torr]	vacuum of injection side [Torr]	bias voltage [-V]	electrode position [mm]	axial magnetic field
721	1.1×10^{-7}	2.1×10^{-7}	230	15	Mirror Field I shown in Fig. 5.6

Figure 5.11 shows the dependence of various Xe ions on the bias voltage of the electrode. After the source was optimized to produce each Xe ion, the beam intensities were measured as a function of the bias voltage. The optimized parameters for producing each ion are listed in Table 5.5. The magnetic configuration was Mirror Field II, shown in Fig. 5.6.

The beam intensities increase with the bias voltage and then saturate above a certain bias voltage. We need a higher negative bias voltage for maximizing the beam intensities of lower charge state Xe ions. As shown in Fig. 5.9, Mirror Field II is suited to higher charge states since its ion

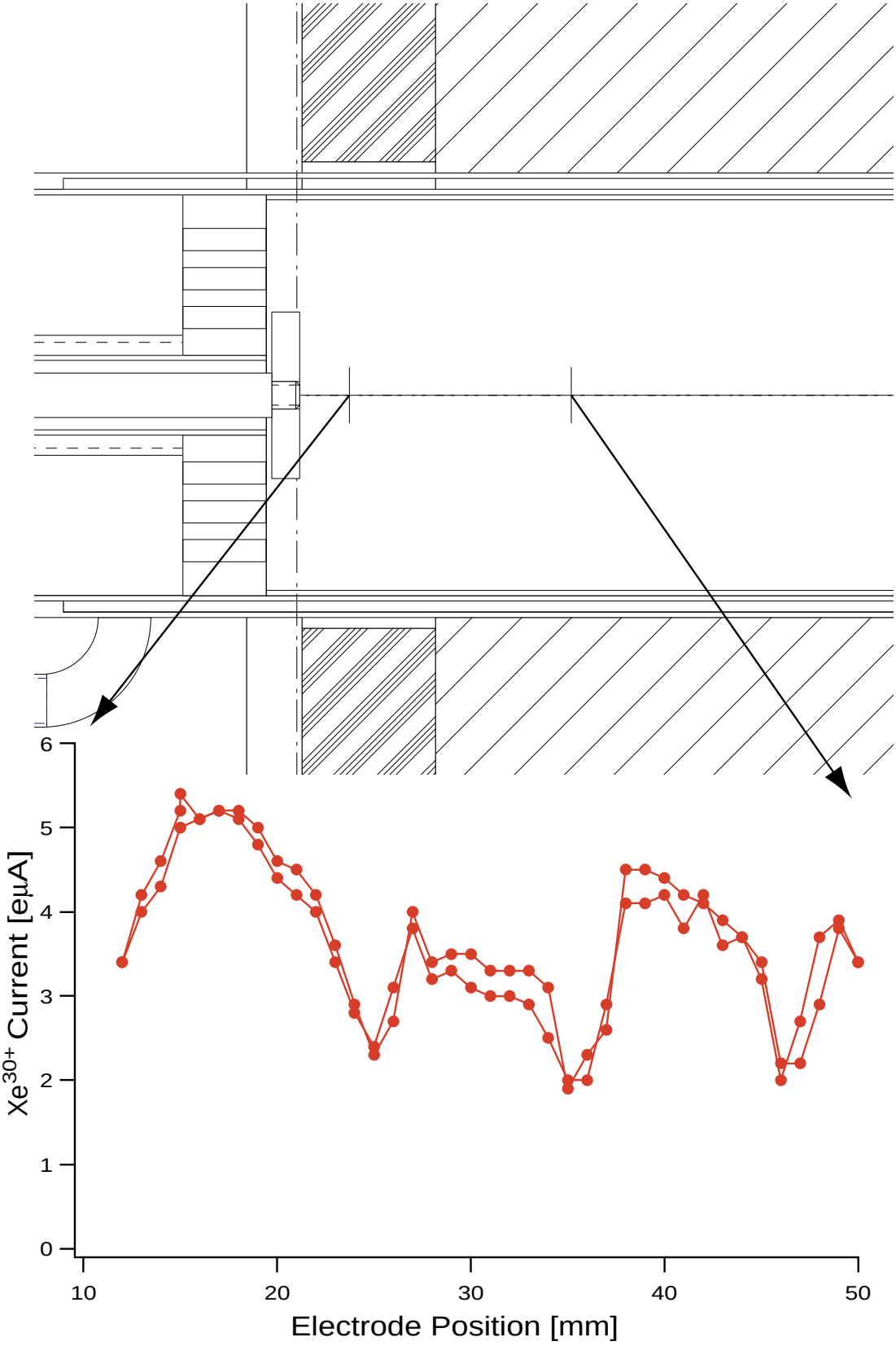

Figure 5.10: Beam intensity of Xe^{30+} as a function of the electrode position. The bias voltage is 230 V.

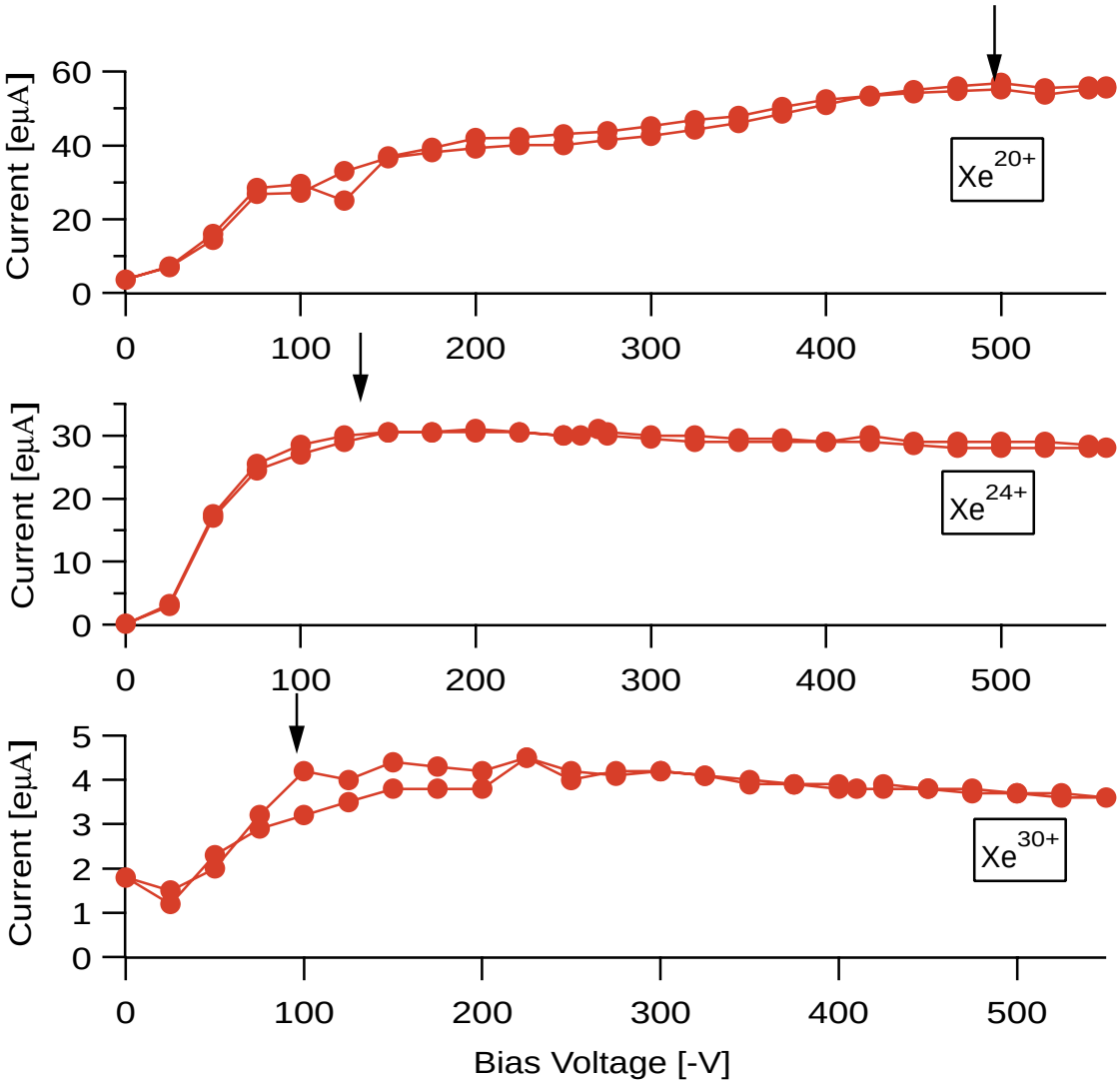

Figure 5.11: Beam intensities of Xe ions of various charge state as a function of the bias voltage.

Table 5.5: The parameters of the measurements of Fig. 5.11

ion	RF Power [W]	vacuum of extraction side [Torr]	vacuum of injection side [Torr]	bias voltage [-V]	electrode position [mm]
Xe^{20+}	668	2.6×10^{-7}	1.3×10^{-7}	540	18
Xe^{34+}	580	1.8×10^{-7}	4×10^{-7}	275	13
Xe^{30+}	774	1.4×10^{-7}	1.8×10^{-7}	420	5

confinement time is probably too long for lower charge states. Therefore we belive that lower-charge-state ions require more help of the biased electrode than higher-charge-state ions for an effective extraction in Mirror Field II. This result supports the experimental results described in chapter 3. A biased electrode may help to effectively extract ions from an ECRIS.

5.2.5 Comparison with Other ECRISs and Discussion

Figure 5.12 compares the beam intensities of highly charged Xe ions between SHIVA and other high performance ECRISs using 14.5 GHz microwaves.

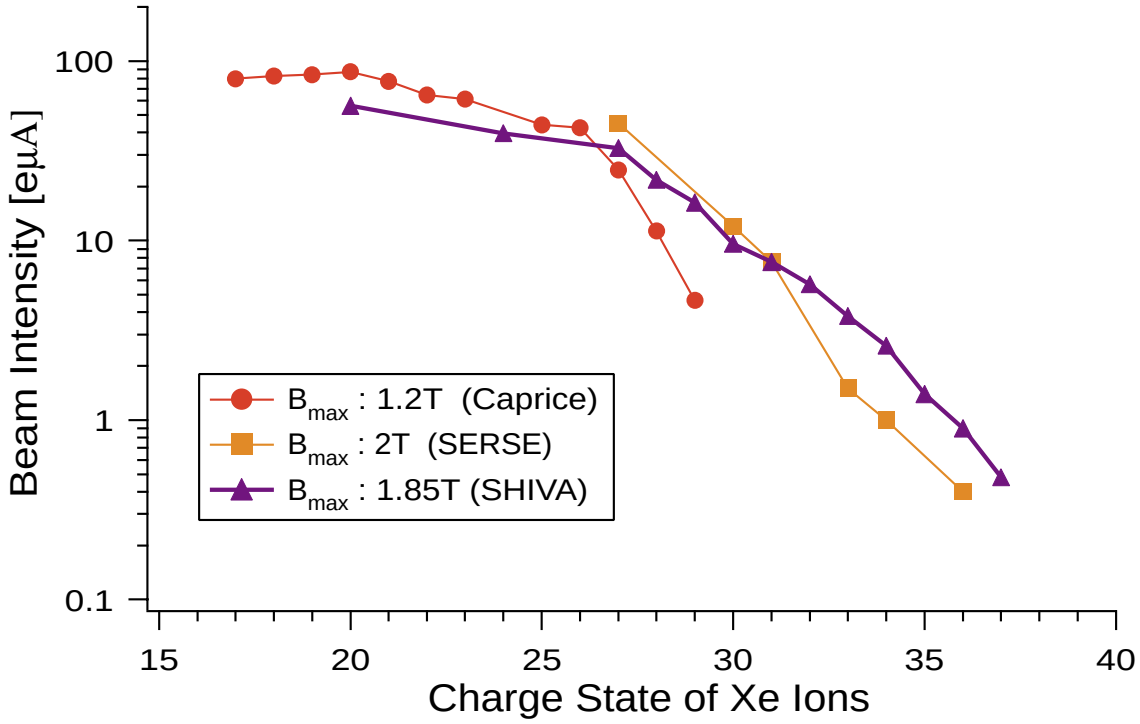

Figure 5.12: Comparison of intensities of Xe ions between various ECRISs using 14.5 GHz microwaves

SERSE is a superconducting ECRIS of the Laboratorio Nazionale Sud (L.N.S.), Catania [31, 35, 34] (Fig. 5.13). The ion source has a large plasma chamber, superconducting coils refrigerated with liquid He and used for both the solenoid coils and the hexapole magnet. Caprice is a compact ECRIS using room-temperature coils, which was developed in

CEA, Grenoble [36](Fig. 5.14). It has a small plasma chamber. The dimensions and other parameters of SHIVA, SERSE and Caprice are listed in Table 5.6.

Table 5.6: Comparison of dimensions and other parameters between various 14.5 GHz ECRISs

	SHIVA	SERSE	Caprice
B_{max} of axial magnetic field	1.85 T	2 T	1.2 T
radial magnetic field	1 T	1.1 T	1.08 T
extraction voltage	15 kV	20 kV	20 kV
inner diameter of plasma chamber	72 mm	130 mm	66 mm
length of plasma chamber	375 mm	420 mm	160 mm
axial length of resonance zone	∼100 mm	∼100 mm	∼90 mm
diameter of resonance zone	∼40 mm	∼73 mm	∼37 mm
volume enclosed by resonance surface (a cylindrical shape is assumed)	∼126 cm^3	∼419 cm^3	∼108 cm^3
biased electrode	yes	yes	yes
aluminium cylinder or chamber	yes	no	yes
typical injected RF power	∼800 W	∼1200 W	∼1200 W

As shown in Fig. 5.12, SHIVA and SERSE perform better for higher charge states than Caprice. On the other hand, Caprice has the best performance for medium charge states. Remarkably, SHIVA with the lowest injected RF power has the best performance for higher charge states.

SHIVA and SERSE are especially suited to generate highly charged ions in comparison to Caprice. Both SHIVA and SERSE are longer plasma chambers and higher magnetic mirror fields than Caprice.

As described in Ref. [8, 9], the ion confinement time τ_i is written as

$$\tau_i \propto \frac{B_{\max}}{B_{\min}} \left[\frac{\text{plasma length}}{\text{avg. ion velocity}} \right] \tag{5.1}$$

This equation shows that a longer plasma chamber and a higher mirror field cause the better ion confinement time. Therefore, the charge state

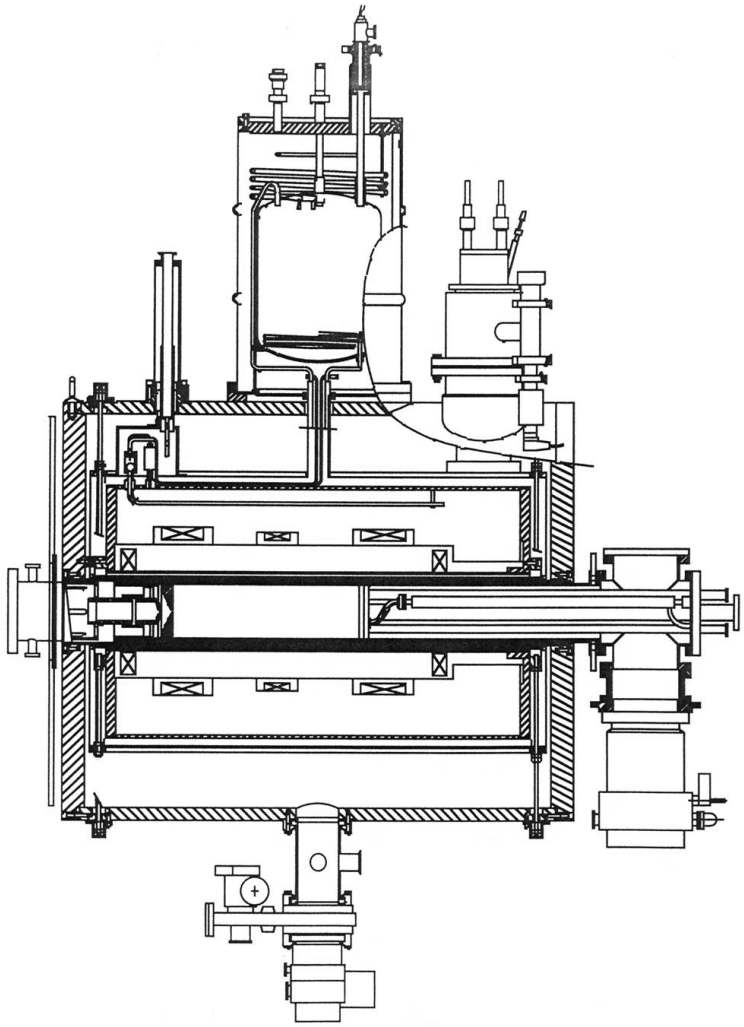

Figure 5.13: A cross-sectional view of SERSE

distributions of SHIVA and SERSE are shifted to higher charge states than that of Caprice. But, too long an ion confinement time due to the strong plasma confinement of SHIVA may cause lower performance for medium charge states.

One of the differences between SHIVA and SERSE is the material which covers the inner wall of the plasma chamber. The inner wall of the plasma chamber of SHIVA is covered by an aluminium cylinder. The material of the inner wall of SERSE is stainless steel. In the case of SERSE, it was reported [35] that an aluminium cylinder degraded beam intensities. However, the aluminium cylinder in SHIVA greatly improves the beam intensities, as shown in Fig. 5.15. The LBL group reported that the plasma

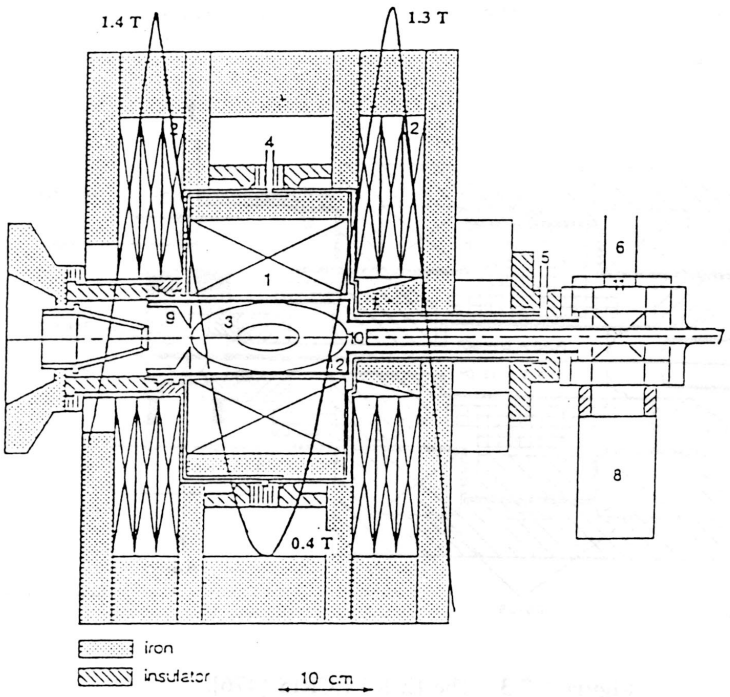

Figure 5.14: A cross-sectional view of Caprice

potential decreases dramatically when the plasma chamber is coated by aluminum oxide and that it is independent of the microwave power [37]. A low plasma potential helps to increases the confinement time of highly charged heavy ions in plasma. Furthermore, the secondary electrons from an aluminium cylinder increases the electron density and shortens the ionization time.

The difference in the ion confinement times is reflected in the difference between the charge state distributions of SHIVA and SERSE. Figure 5.16 shows a comparison of charge state distributions of Xe ions between SHIVA and SERSE, which are optimized for Xe^{30+}. The mean charge state of SHIVA is higher than that of SERSE. The mean charge state distribution of SHIVA and SERSE are 28+ and 27+, respectively. The longer plasma chamber and the SHIVA's aluminum oxide on inner wall of the chamber cause to increase the beam intensities of highly charged ions in SHIVA over those of SERSE.

One more remarkable point in Table 5.6 is that the required RF power for SHIVA is lower than those for both SERSE and Caprice. In general,

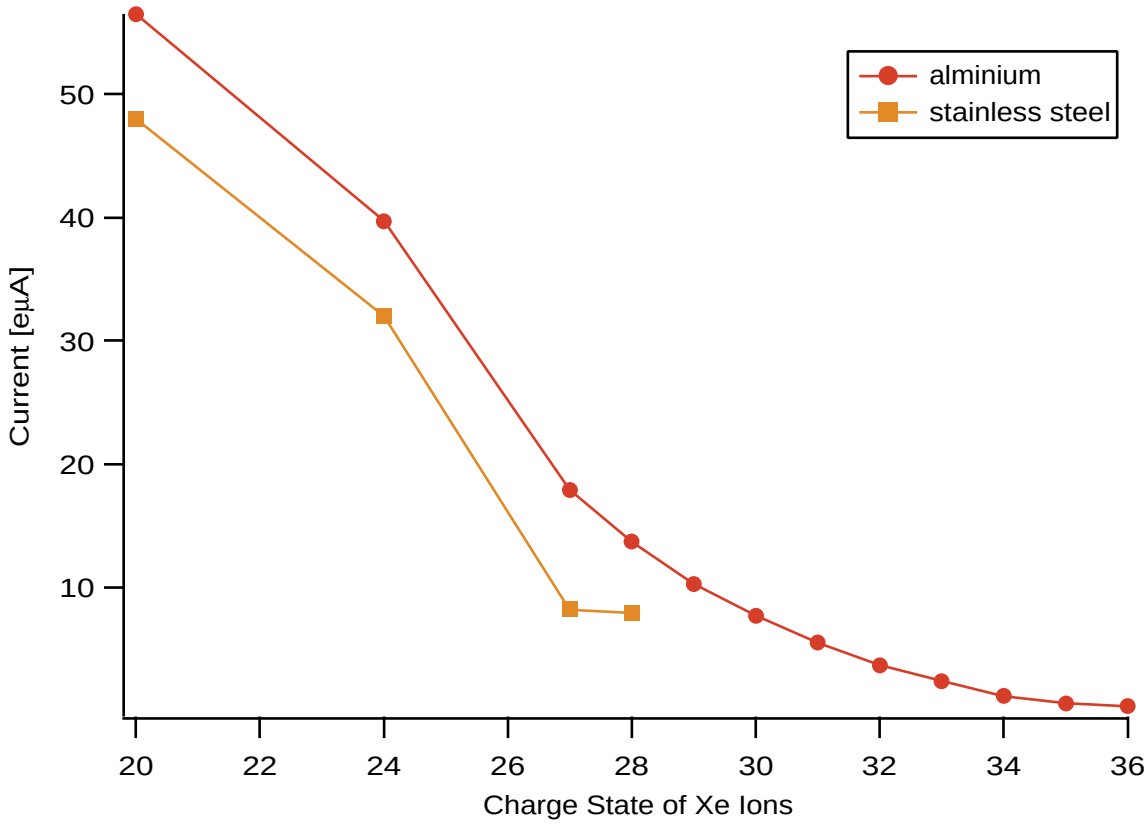

Figure 5.15: Comparison of Xe currents between with and without the aluminum cylinder in Mirror Field II.

it is thought that a smaller plasma volume require a smaller consumption of RF power. Actually, SERSE, with a larger plasma chamber, needs a higher RF power than SHIVA. However, it is strange that Caprice, with a smaller chamber, requires a higher RF power than SHIVA. The reason why Caprice requires almost the same RF power as SERSE may be a poor plasma confinement due to a lower magnetic field strength. Caprice may require a higher RF power to obtain a high density and high temperature plasma. From these experimental results, we concluded that a better plasma confinement and a smaller plasma volume will leads to a lower RF power consumption.

To summarize, the long plasma chamber, the high axial magnetic field and the aluminium cylinder on the inner wall of the plasma chamber lead to longer ion confinement times in SHIVA. Consequently SHIVA can produce intense beams of highly charged heavy ions. We conclude that these char-

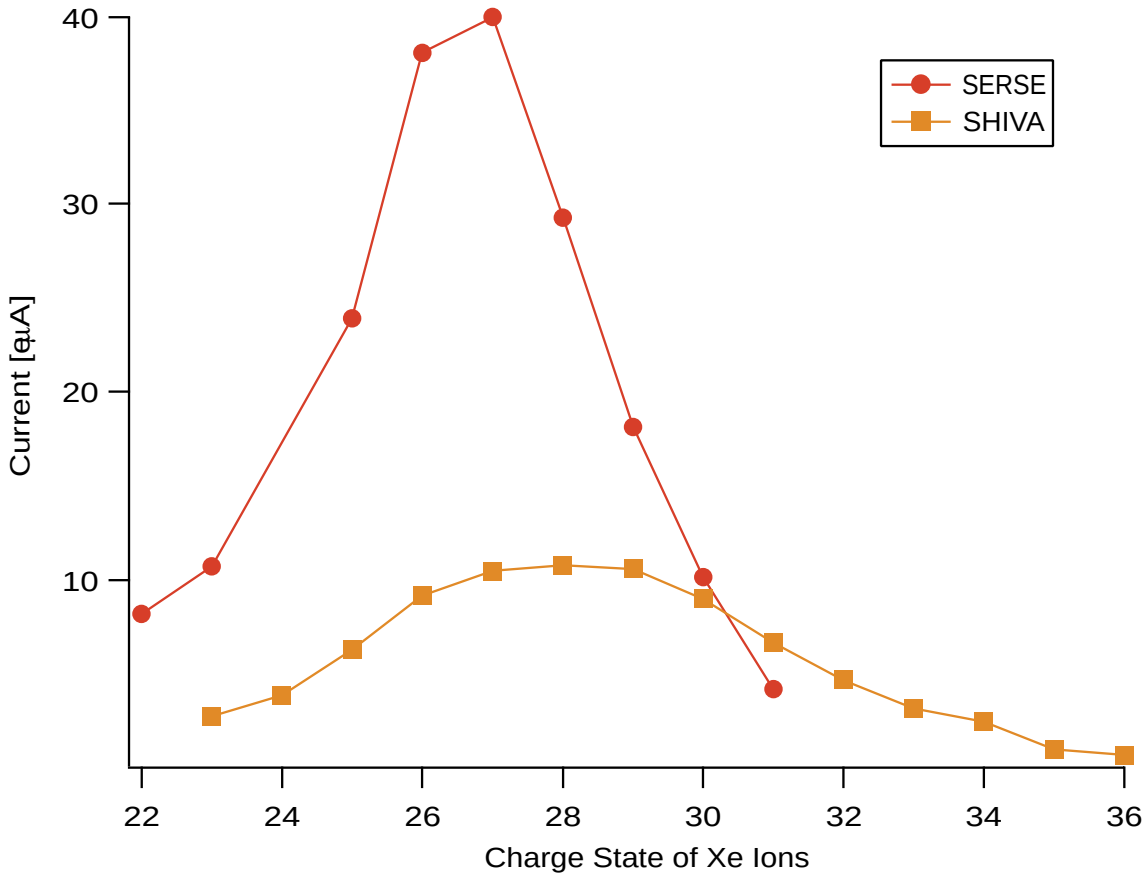

Figure 5.16: Charge state distributions of SHIVA and SERSE [34], tuned for Xe^{30+}

acteristics (long plasma chamber, high axial magnetic field and aluminium cylinder) are essential to produce intense highly charged ion beams, and that the biased electrode is helpful in optimizing the ion source for effective ion extraction. Furthermore, a small plasma chamber volume and high axial magnetic field lead to a low RF power consumption for ECRIS.

Chapter 6

Summary

We have designed and constructed a new ECR ion source using liquid-He-free superconducting solenoid coils to meet the requirements of cluster fission projects. And, we have found the optimum parameters for producing intense beams of highly charged heavy ions.

Before designing the new ECRIS, we researched the influence of a biased electrode on an ECR plasma and beam intensities using pulsed microwaves. We found the biased electrode changes plasma potential dip and adjust the ion confinement time. Consequently, the biased electrode amplifies the extracted currents from the ECRIS and helps optimize the ECRIS to produce an intense beam of highly charged heavy ions.

In the design of the new ECRIS to produce highly charged ions, we chose hybrid magnetic configuration which consist of a permanent hexapole magnet and superconducting solenoid coils cooled with small refrigerators. This magnetic configuration makes it possible to achieve a higher magnetic field with a superconducting magnet while avoiding the difficulties related to the use of liquid helium. To implement this magnetic configuration efficiently, we determined the optimum configuration for the solenoid coils, the axial position of the yoke, in addition to the optimum operational parameters, such as the current in the coils. Also we determined the optimum shape of the hexapole magnet.

We named the new type ECRIS SHIVA (**S**uperconducting without liquid **H**e ECR **I**on source for **V**arious **A**tomic cluster experiments). We found the optimum parameters (e.g., magnetic field configuration, RF power and voltage for the biased electrode) for producing intense beams

of highly charged ions. As a result, SHIVA excels in the production of highly charged ions. In comparison with other high performance ECRISs using 14.5 GHz microwaves, we found that the long plasma chamber, the high magnetic field and the aluminium cylinder of SHIVA achieves longer ion confinement time and more intense beam of highly charged ion. Furthermore, a small plasma chamber volume and a high axial magnetic field results lower RF power consumption for an ECRIS.

SHIVA makes it possible to observe fission phenomena of metal clusters around the phase transition for the first time in the world, and has a best performance of all of 14.5 GHz ECRISs in the world in producing highly charged heavy ions. We success to mark a step in the progress of ECRIS.

Acknowledgment

A large number of colleagues contributed to various aspects of the design and experimental studies as this work developed. I struggled with lots of problems for design, installation and experiments. I owed a great deal to all of them.

I express my profound gratitude for the guidance, warm encourage and generous help received from Prof. S. M. Lee and Prof. I. Arai. In particular, I am deeply grateful to Dr. T. Nagawawa for his kind support, warm encouragement, helpful advice, valuable discussion for the whole of this research activities. This study originated his idea and progressed with his guidance. Also I appreciate for helpful comments of Prof T. Hattori, Prof Y. Tagishi and Prof. Y. Miake.

The design of superconducting magnetic system was developed with Dr. T. Kawaguchi. And Mr. C. K. Chung gave me helpful advices for the mechanical design of the source. I could not complete this work without their supports. I gratefully acknowledge their helps.

I am much indebted to research collaborators Mr. M. Imanaka and Mr. M. Tsukada. I installed the source and performed experiments with them.

I am very grateful Prof. M. Kase, Prof. A. Goto and Prof. Y. Yano for their generous help and economical supports through Junior Research Associate institution during my stay at RIKEN. Also I appreciate Dr. M. Kidera and Mr. Y. Higurashi for all kinds of helps.

Finally, I acknowledge suggestive discussions and support of assembling the source with Dr. T. Miyazaki, Dr. H. Suzuki, Mr. H. Sasaki, Mr. S. G. Lee, Mr. S. Shimakura, Mr. J. Hirose and Mr. K. Hino, and also thanks to all professors, students and the technical staffs of the Tandem Accelerator Center in University of Tsukuba for their support.

Bibliography

[1] K. Sattler, J. Mühlboch, O. Echt, P. Pfau, and E.Recknagel.
Evidence for coulomb explosion of doubly charged microcluster.
Phys. Rev. Lett., 47(3):160, July 1981.

[2] F. Chandezon, C. Guet, B. A. Huber, D. Jalabert, M. Maurel, E. Monnandand, C. Ristori, and J. C. Rocco.
Critical Sizes against Coulomb Dissociation of Highly Charged Sodium Clusters Obtained by Ion Impact.
Phys. Rev. Lett., 74(19):3784, 1995.

[3] C. Guet, X. Biquard, P. Blaise, Blundell, M. Gross, Huber, D. Jalabert, M. Maurel, L. Plagne, and Rocco.
Excitation and fragmentation of highly charged metal clusters in collisions with ions.
Z. Phys. D, 40:317, July 1996.

[4] Hellmunt Herberland ant Martin Karrais, Martin Mall, and Yonca Thuner.
Thin films from energetic cluster impact: A feasibility study.
J. Vac. Sci. Thechnol. A, 10(5):3266, May 1992.

[5] T.P. Martin, T. Bergmann, H.Göhlick, and T. Lange.
Electronic shells and shells of atoms in metallic clusters.
Z. Phys. D, 19:25, 1991.

[6] B. C. Allen.
The Surface Tension of Liquid Metals, chapter 4, page 161.
Marcel Dekker, Inc., New York, 1972.

[7] U.Näher, S.Frank, N.Malinowski, U.Zimmermann, and T.P.Martin.
Fission of highly charged alkali metal clusters.
Z. Phys. D, 31:191, 1994.

[8] R. Geller.
Electron Cyclotron Resonance Ion Sources and ECR Plasmas.
IOP, Bristol, 1996.

[9] T.D. Rognlien and T.A. Cutler.
Transition from pastukhov to collisional confinement in a magnetic and electrostatic well.

Nucl. Fusion, 20(8):1003, 1980.

[10] Francis F. Chen.
Introduction to Plasma Physics an Controlled Fusion.
Plenum Press, 1984.

[11] T. K. Fowler and Richard F. Post.
Progress toward Fusion Power.
Scientific American, 215(6):21, 1966.

[12] 川村孝弐.
ECR プラズマの電子速度分布の形成.
理化学研究所報告, 64(4):125, 1988.

[13] H. Grawe.
A STOCHASTIC MODEL OF ELECTRON CYCLOTRON HEATING.
Plasma Phys., 11:151, 1969.

[14] A. Girard and G. Melin.
ECR ion sources today Physics, performance and technology.
Nucl. Instr. and Meth. in Phys. Res. A, 382:252, 1996.

[15] R. Geller.
ECRIS: The Electron Cyclotron Resonance Ion Sources.
Annu. Rev. Nucl. Part. Sci., 40:15, 1990.

[16] G. Shirkov.
Highly Charged Ion production in ECR Source of Heavy Ions.
CERN/PS 94-33(HI), 1994.

[17] P. Sortais.
Pulsed ECR ion source using the afterglow mode.
Rev. Sci. Intrum., 63(4):2801, April 1992.

[18] G. Melin, F. Bourg, P. Briand, J. Debernardi, M. Delaunay, R. Geller, B. Jacquot, P. Ludwig, T.K. N'Guyen, L. Pin, M. Pontonnier, J.C. Rocco, and F. Zadworny.
Some particular aspects of the physics of the ECR sources for multicharged ions.
Rev. Sci. Intrum., 61(1):236, January 1990.

[19] B. H. Wolf.
Handbook of Ion Sources, chapter 2, page 121.
CRC Press, Boca Raton, 1995.

[20] T. Kurita, T. Nakgawa, M.Kidera, Y. Miyazawa, M. Hemmi, T. Chiba, N.Inabe, M.Kase, T.Kageyama, O.Kamigaito, A.Goto, and Y.Yano.
Effect of Electrode for Producing the Highly Charged Heavy Ions form RIKEN 18 GHz Electron Cyclotron Resonance Ion Source.

Jpn. J. Appl. Phys., 38:3707, 1999.

[21] G. Melin, C.Barue, F.Bourg, P. Briand, J. Debernardi, M. Delaunay, R. Geller, A. Girard, K. S. Golovanivsky, D. Hitz, B. Jacquot, P. Ludwig, J.M.Mathonnet, T. K. Naguyen, L. Pin, M. Pontonnier, J. C. Rocco, and F. Zadworny.
Recent Developments and Future Projects on ECR ion sources at Grenoble.
In *Proceeding of the 10 th International Workshop on ECR Ion Sources*. Ork Ridge National Laboratory, 1991.

[22] S. Gammino, J. Sijbring, and A. G. Drentje.
Experiment with a biased disk at the K.V.I ECRIS.
Rev. Sci. Intrum., 63(4):2872, April 1992.

[23] M. Leitner, D. Wutte, J. Brandstotter, F. Aumayr, and H.P. Winter.
Single-stage 5 GHz ECR-multicharged ion source with high magnetic mirror ratio and biased disk.
Rev. Sci. Intrum., 65(4):1091, April 1994.

[24] M. Leitner, D. Wutte, and HP. Winter.
A Single Stage "Gissen Type" 5GHz-ECR Ion Source with A High magnetic Mirror Ratio.
In *Proceeding of 11th International Workshop on ECR Ion Sources*, Groningen, 1993.

[25] Takahide Nakagawa, Sandor Biri, Masanori Kidera, Yoshitoshi Miyazawa, Masatake Hemmi, Toshiya Chiba, Naohito Inabe, Masayuki Kase, Tadashi Kageyama, Osamu Kamigaito, Akira Goto, and Yasushige Yano.
Upgrade of RIKEN 18 GHz Electron Cyclotron Resonance Ion Source Using an Electrode at Floating Potential.
Jpn. J. Appl. Phys., 37(5A):2699, May 1998.

[26] T. Nakagawa, J. Ärje, Y.Miyazawa, M. Hemmi, T.Chiba, N. Inabe, M. Kase, T. Kageyama, O. Kamigaito, A. Goto, and Y. Yano.
DEVELOPMENT OF RIKEN 18GHz ECRIS.
In *Proceeding of 5th European Particle Accelerator Conference*, page 1478, Bristol, 1996. IOP.

[27] N. Nambudripad.
CRYOGENIC ENGINEERING, chapter 17, page 438.
Academic Press Inc., 1986.

[28] DAIKIN CRYOTEC.
Manual of refrigerators.

[29] T. Nakagawa, Y.Miyazawa, M. Hemmi, T. Chiba, N. Inabe, M. Kase, T. Kageyama, O. Kamigaito, A. Goto, and Y.Yano.

Improvement of RIKEN 18 GHz Electron Cyclotron Resonance Ion Source using Aluminum Tube.
Jpn. J. Appl. Phys., 35(7):4077, 1996.

[30] Vector Fields.
http://www.vectorfields.com/.

[31] G. Ciavola and S. Gammino.
Superconducting ECR sources.
Nucl. Instr. and Meth. in Phys. Res. A, 382:267, 1996.

[32] Los Alamos Accelerator Code Group.
http://laacg1.lanl.gov/.

[33] S. Gammino, G. Ciavola, T. Antaya, and K. Harrison.
Volume scaling and magnetic field scaling on SC-ECRIS at MSU-NSCL.
Rev. Sci. Intrum., 67(1):155, January 1996.

[34] S. Gammino, G. Ciavola, L. Celona, M. Castro, F. Chines, and S. Marletta.
18 GHz upgrading of the superconducting electron cyclotron resonance ion source SERSE.
Rev. Sci. Intrum., 70(9):3577, September 1999.

[35] P. Ludwig, F. Bourg, P. Briand, A. Girard, G. Melin, D. Guillaume, P. Seyfert, A. La Grassa, G. Ciavola, S. Gammino, M. Castro. F. Chines, and S. Marletta.
Summary of the performances of the superconducting electron cyclotron resonance ion source at 14GHz.
Rev. Sci. Intrum., 69(12):4082, December 1998.

[36] D. Hitz, F. Bourg, M. Delaunay, P. Ludwig, G. Melin, M. Pontonnier, and T. K. NGuyen.
The new 1.2 T-14.5 GHz Caprice source of multicharged ions: Results with metallic elements.
Rev. Sci. Intrum., 67(3):883, March 1996.

[37] Z. Q. Xie and C.M. Lyneis.
Improvements on the LBL AECR source.
In Masayuki Sekiguchi and Takahide Nakagawa, editors, *Proceedings of the 12th International Workshop on ECR ion sources*. RIKEN, 1995.